**Title**
Materials Design of Li Superionic Conductors for All-Solid-State Batteries



**Author**
Sun, Yingzhi

**Publication Date**
2022

Peer reviewed|Thesis/dissertation

# Materials Design of Li Superionic Conductors for All-Solid-State Batteries

by

Yingzhi Sun

A dissertation submitted in partial satisfaction of the

requirements for the degree of

Doctor of Philosophy

in

Engineering – Materials Science and Engineering

in the

Graduate Division

of the

University of California, Berkeley

Committee in charge:

Professor Gerbrand Ceder, Chair
Professor Kristin Ceder-Persson
Professor Bryan McCloskey

Fall 2022

Materials Design of Li Superionic Conductors for All-Solid-State Batteries



by

Yingzhi Sun

Abstract

Materials Design of Li Superionic Conductors for All-Solid-State Batteries

by

Yingzhi Sun

Doctor of Philosophy in Engineering – Materials Science and Engineering

University of California, Berkeley

Professor Gerbrand Ceder, Chair

As the use of lithium-ion batteries in consumer electronics and electric vehicles has grown, safety issues such as those arising from leakage and flammability of the organic liquid electrolyte have garnered increased attention. By replacing the organic liquid electrolyte with an inorganic solid electrolyte, however, these concerns can be circumvented, thereby improving the safety of the battery system. In addition, solid-state batteries are also expected to possess higher energy density than their conventional counterparts. On the anode side, the high modulus of the solid electrolyte is expected to constrain the growth of Li dendrites, which might enable the use of a Li metal anode. Furthermore, because some solid electrolytes possess a wide electrochemical stability window, high-voltage cathodes (> 4.5 V, vs $Li^+/Li$) may be used to further improve the total energy density.

The superionic conductor is one of the key parts of solid-state batteries. Over the past 20 years, accelerated development of Li superionic conductors has occurred. The ionic conductivities of some of these superionic conductors approach or even surpass those of liquid electrolytes. However, most reported superionic conductors have obvious drawbacks. New superionic conductors that meet all the requirements of solid-state batteries are needed. There are two strategies for exploring new potential superionic conductors: (1) modification the chemical composition based on the crystal structure of known fast Li conductors to further improve the properties or (2) searching for Li conductors with new crystal structures based on the structural features that favor fast $Li^+$ migration. In this dissertation, new superionic conductors are designed and explored by implementing both of these strategies.

Specifically, a strategy is developed to increase the ionic conductivity of sulfide Li-ion conductors through composition modification. Inspired by the wide use of halogens in superionic conductors, we propose that the conductivity could be further improved by substituting halogens with suitable pseudo-halogens. The Li argyrodite system was used to demonstrate the feasibility of this strategy. $BH_4$-substituted Li argyrodite was successfully synthesized and shown to have a room-temperature ionic conductivity of 4.8 mS/cm which is 5 times higher than that of halogen-substituted Li argyrodites. We further discuss the mechanism underlying the enhanced ionic conductivity and find that the faster Li diffusion originates from the weak interaction between Li and $BH_4$. The results provide design strategies for new superionic conductors with pseudo-halogen substitution.

We also present a structural feature that benefits the Li-ion migration in oxide Li-ion conductors. Based on a statistical analysis of the materials in the inorganic materials database, we discovered that the corner-sharing connectivity of the oxide crystal structure framework is more likely to have a distorted lithium environment with higher site energy. Materials with a corner-sharing framework are also usually less compact, which reduces the repulsion from non-lithium cations. Both features lead to a decreased migration barrier and accelerate the Li diffusion. A high-throughput search was performed based on this structural feature, and 10 new oxide Li-ion conductors were predicted. One of them, $LiGa(SeO_3)_2$, was successfully synthesized and was shown to have a bulk conductivity of 0.11 mS/cm, in agreement with theory predictions. These findings provide fundamental insights into the physical attributes that govern fast lithium conduction and help project new directions towards the discovery of superionic conductors for all-solid-state batteries.

# Table of Contents

# List of Figures

# List of Tables

# Acknowledgements

I would first like to thank my advisor, Professor Gerbrand Ceder for his guidance and support during my graduate studies. Professor Ceder taught me how to develop and carry out scientific research with big vision, clear logic, and high standards. He is also a role model as a leader with integrity, charisma, and effective communication.

I would also like to thank my qualifying exam and dissertation committee, Professor Kristin Ceder-Persson, Prof Bryan McCloskey, Professor Mark Asta, and Professor Jie Yao, for all their invaluable help for my research.

I thank all of my collaborators (KyuJung Jun, Bin Ouyang, Zheren Wang, Yihan Xiao, Yan Wang, Lincoln J Miara, Yaosen Tian, Shou-Hang Bo, Yan Zeng, Ryounghee Kim, Yaqian Zhang, Shuo Sun, Zijian Cai, Valentina Lacivita, Yinsheng Guo, Haegyeom Kim). It would not have been possible to complete my research project without their contribution.

I want to thank my labmates in our solid-state subgroup. These names include Shou-Hang Bo, Jae Chul Kim, Yaosen Tian, Tan Shi, Tina Chen, Yaqian Zhang, Valentina Lacivita, Qingsong Tu, Luis Barroso-Luque, Yan Zeng, Yu Chen, Mouhamad Diallo, Xinxing Peng, Xiaochen Yang, Sunny Gupta, Yunyeong Choi, Ronald Kam, Zhuohan Li, Tara Mishra, Benjamin Lam, Grace Wei, and Jia-Wei Lin. I'm grateful for their value insight and helpful discussion.

I thank the sponsor of our solid-state battery project, Samsung Advanced Institute of Technology, for their interests and support of our research project.

I want to thank all the friends in the Ceder Group for all the wonderful memories! It was a great pleasure to work with and learn from so many bright minds!

Finally, I would like to thank my family for their love, support, and encouragement. I would not be here without their continued support.

# Chapter 1 Introduction

## 1.1 Foreword

Part of this chapter has been published in Tian, Y., Zeng, G., Rutt, A., Shi, T., Kim, H., Wang, J., Koettgen, J., Sun, Y., Ouyang, B., Persson, K., Ceder, G., et al., 2020. Promises and challenges of next-generation "beyond Li-ion" batteries for electric vehicles and grid decarbonization, Chemical Reviews, 121(3), pp.1623-1669., and is reproduced here with the permission of the co-authors.

*Part of this chapter is a work derived by Yingzhi Sun from IEA material and Yingzhi Sun is solely liable and responsible for this derived work. The derived work is not endorsed by the IEA in any manner.*

## 1.2 Motivation and Application

The ever-increasing population, technological development, and economic progress have triggered a rapidly growing energy demand. Currently, fossil fuels continue to supply approximately 80% of the world's energy.[1] The massive exploitation of fossil fuels and the consequent generation of greenhouse gases, such as $CO_2$, have resulted in climate change and various environmental issues. From a sustainability perspective, it is imperative to develop alternative renewable energy technologies. During the past 20 years, several renewable energy sources, including solar, wind, tidal, biomass and geothermal energy, have played increasingly important roles in the global energy supply.[2] However, these energy sources are all inherently intermittent and generally dispersed in nature. Good energy storage systems are needed to optimize the use of these energy sources.

A battery is one of the most common energy storage systems. Based on their rechargeability, batteries can be divided into primary batteries (e.g., alkaline batteries[3] and zinc-carbon batteries[4]) and secondary batteries (e.g., lead-acid batteries[5] and lithium-ion batteries (LIBs)[6]). Owing to their good cycling stability and high energy density, LIBs, first commercialized by Sony in 1991,[7] currently dominate the market and have become ubiquitous in modern electronics.

The emerging electric vehicle (EV) market has further accelerated the growth of the LIB market. After a decade of fast development, the global EVs stock hit the 10-million mark in 2020. Consumers spent USD 120 billion on EV purchases in 2020, which is 50% higher than in 2019. Governments across the world spent USD 14 billion on direct-purchase incentives and tax deductions for EVs in 2020 with a 25% year-over-year rise. To date, over 20 countries have announced the full phase-out of internal combustion engine (ICE) car sales over the next 10–30 years (Figure 1.1), and more than 120 countries have announced economy-wide net-zero emissions pledges to support the development of EVs.[8] However, global EV adoption is still in the very early stage, and further adoption of EVs requires improvement of their batteries.

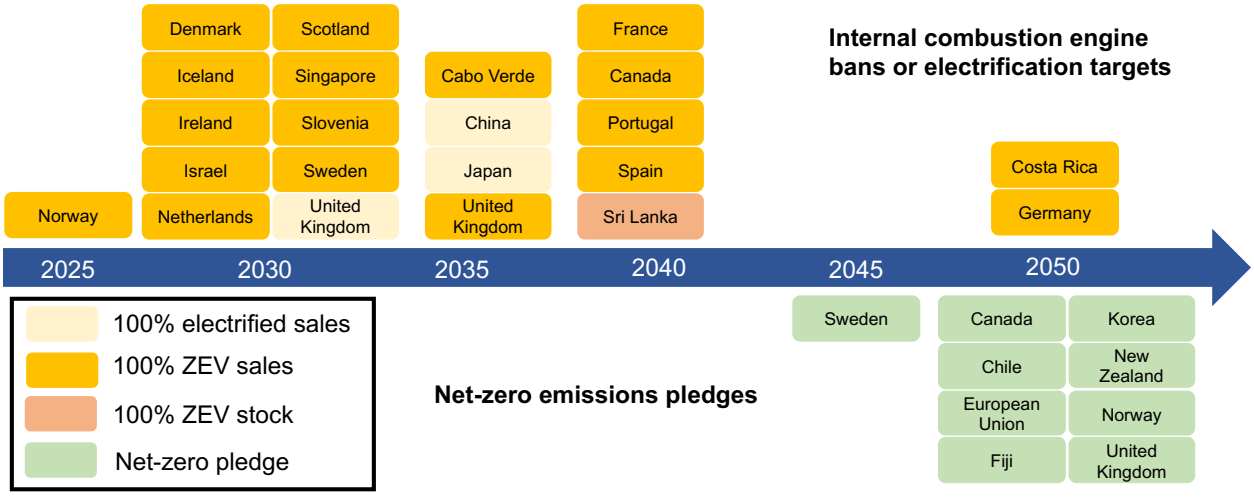


**Figure 1.1 Timeline of electrification targets/ICE bans in different countries.** IEA 2021; Global EV Outlook 2021, https://www.iea.org/reports/global-ev-outlook-2021, Creative Commons (CC) License: CC BY 4.0

Over the past decades of development, the cell-architecture and electrode-material options for LIBs have been established. Olivines (e.g., $LiFePO_4$), spinels (e.g., $LiMn_2O_4$), and layered oxides (e.g., $LiNi_{0.8}Co_{0.15}Al_{0.05}O_2$ and $Li(Ni, Mn, Co)O_2$) are typically used as cathodes, which are separated from a graphite anode by a polymer separator immersed in a carbonate-based organic liquid electrolyte. The specific energy of LIBs has increased from approximately 90 Wh $kg^{-1}$ in the 1990s to over 250 Wh $kg^{-1}$ today. In addition, as manufacturing has improved, the cost of LIB modules has been significantly reduced from over 1000 USD kW $h^{-1}$ to lower than 150 USD kW $h^{-1}$.[9] However, materials-level advancements in LIBs are also approaching fundamental limits. On the cathode side, layered oxide materials, particularly Ni-rich compounds, will likely dominate the market in the near future

because of their good performance, competitive cost, and well-established manufacturing process. In the meantime, however, the potential gains from further modifying the cathode are also becoming limited. On the anode side, graphite (both synthetic and natural) is still almost exclusively used. Although pure Si anodes have much higher capacity than graphite, the Si content in today's commercial cells is still very limited due to lifetime problems caused by the non-passivating solid-electrolyte interphase (SEI) on Si and dramatic volume change (over 300%) during lithiation/delithiation.[10] The demands for batteries with higher energy density and higher power density to satisfy the requirements of future EVs have triggered the investigation of systems beyond conventional LIBs.

Directly using Li metal as the anode provides a path to significantly increase the energy density of Li batteries. Although tremendous efforts have been dedicated to this approach[11], it remains difficult to make a Li metal anode work well in liquid electrolytes because of the dendrite problem and unstable SEI. In this context, all-solid-state batteries (ASSBs) are considered better suited for utilizing a Li metal anode owing to the high modulus and wide electrochemical stability window of solid electrolytes. Figure 1.2 compares the specific energies and energy densities at the cell level of the common cathodes used in a typical LIBs and a Li-metal ASSBs.[12] Because of the reduction in volume and mass associated with the use of a Li-metal anode, multiple selected Li-ion cathodes deliver volumetric energy densities larger than 750 Wh $L^{-1}$ at the cell level in the ASSB, with a maximum volumetric energy density of 1373.8 Wh $L^{-1}$ reached using the NCA cathode. Although these comparisons do not represent the optimal cell-level energy densities of various ASSB systems, they demonstrate the significant energy-density increase that can be achieved using established LIB cathodes in an ASSB configuration.

Besides the better compatibility with a Li-metal anode, ASSBs also offer the advantages of compatibility with high-voltage cathodes (>4.5 V vs $Li^+/Li$) and improved safety, as the flammable organic liquid electrolyte is replaced with a non-flammable solid electrolyte. Overall, ASSBs represent safer and more powerful next-generation electrochemical energy storage systems. More detailed information on the technologies of ASSBs will be introduced in Part 1.2.

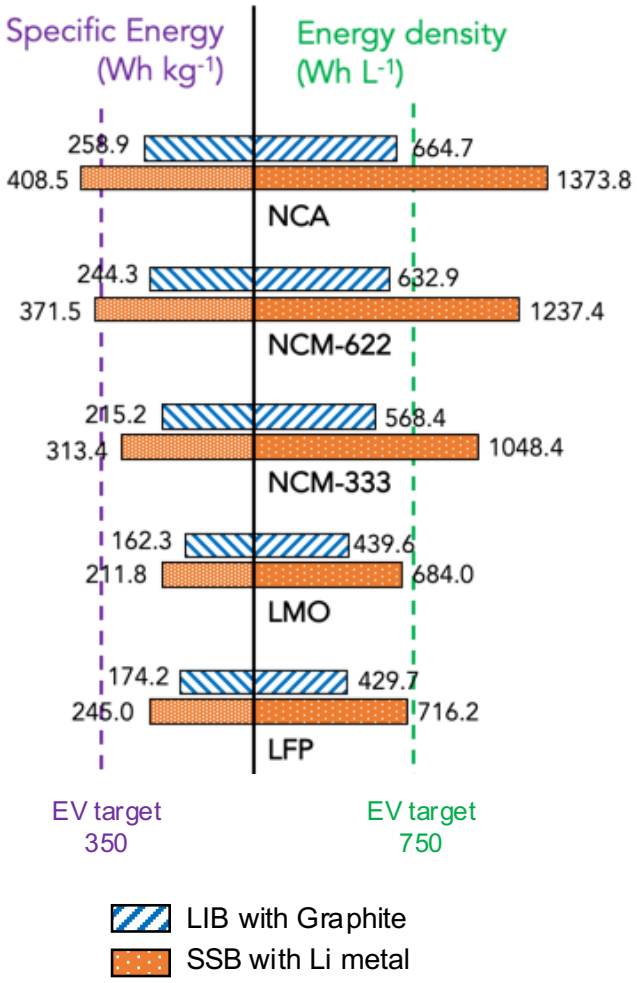


**Figure 1.2 Specific energy and energy density calculations of LIBs and SSBs.** The inputs employ data from the BatPaC model.[13] Assumptions for the lithium–metal ASSB cell: a Li-metal anode is used in all the ASSBs and a Li utilization of 0.80 was set to determine the anode thickness; the cathode composite contains the same cathode loading as in the LIBs (80–83 wt.%, depending on the cathode), 6 wt.% conductive carbon, and SE powder of the remaining weight ratio; the cell uses a $Li_2S$–$P_2S_5$ solid separator of 20-μm thickness with a porosity of 5 vol % in the SE pellet and a density of 1.87 g $cm^{-3}$. This figure is adapted and reproduced from ref. [12].

## 1.3 All-solid-state batteries

### 1.3.1 Overview of all-solid-state batteries

In solid-state batteries (SSBs), solid ionic conductors are used as the electrolyte to transport working ions between the anode and cathode. In addition, it is necessary to distinguish all-solid-state batteries (ASSBs) from quasi-solid-state batteries (QSSBs) even though both are sometimes referred to as SSBs. In QSSBs, a small amount of liquid electrolyte is used at the interface between the solid electrolyte and electrode materials. Although the existence of the liquid electrolyte might improve the ion transport through the interface, it also brings back the problems of the liquid electrolyte, such as leakage and flammability, to the SSBs. In ASSBs, the electrolyte is totally composed of solid ionic conductors without any liquid additive. Albeit more challenging, ASSBs are closer to the ideal next-generation battery system. During the past 20 years, intense research efforts have been focused on the solid electrolyte, accelerating the discovery of a wide variety of new fast solid ionic conductors.[14,15] Driven by the rapid research progress, ASSBs have been pushed close to commercialization. Several major automotive companies have targeted the mid-2020s to begin using ASSBs in EVs.[16–18]

The most common solid electrolytes can be divided into two categories: ceramics and polymers. Although polymer solid electrolytes are mechanically soft and can better accommodate the electrode volume change during lithiation/delithiation, the conductivity of polymer electrolytes is quite low at room temperature, and most of these electrolytes still have flammability risks.[19] In contrast, ceramic solid electrolytes are generally non-flammable and possess much higher ionic conductivities even at low temperature, making them more suitable for practical ASSBs. The cell structures of conventional LIBs and ASSBs with ceramic solid electrolytes are shown in Figure 1.3.[20] Conventional LIBs contain a porous cathode and porous anode, coated on thin aluminum and copper foils, respectively. A thin separator (~ 10-$\mu$m thick) is placed between the cathode and anode to prevent short-circuiting. The liquid electrolyte infiltrates the porous electrodes and separator to provide an ionic pathway. In a ASSBs with a conventional anode (i.e., graphite), the liquid electrolyte in the electrodes and the separator are completely replaced by a solid electrolyte. It is worth noting that the solid electrolyte used as the separator and the solid electrolytes in the electrodes are sometimes different for stability and manufacturing reasons. ASSBs with a Li-metal anode can be made by further replacing the graphite anode with Li metal. In this case, a more compact cell

structure can be obtained, resulting in both higher volumetric energy density and higher specific energy.

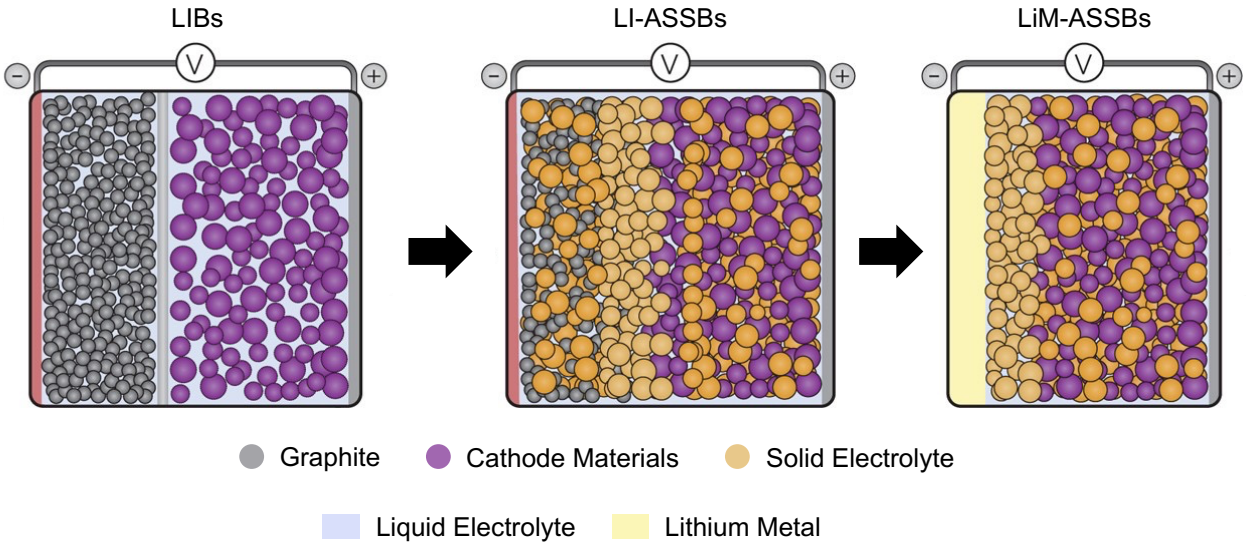


**Figure 1.3 Cell structures of LIBs and ASSBs.**
Schematic illustration of LIBs (left), ASSBs with graphite anode (LI-ASSBs, middle), and ASSBs with Li-metal anode (LiM-ASSBs, right). This figure is adapted and reproduced from ref. [20].

## 1.3.2 Potential benefits of all-solid-state batteries

The improved safety is one of the most significant advantages of ASSBs over conventional LIBs. With the widespread use of LIBs, the inherent safety issues have garnered increased attention, especially after several widely publicized safety incidents involving both EVs and consumer electronics.[21,22] A major concern for conventional LIBs is the flammability of the organic liquid electrolyte. The organic liquid electrolyte can participate in a rapid exothermal reaction after thermal runaway caused by mechanical or electrical abuse, further resulting in fire or explosion. In ASSBs, the flammable organic liquid electrolyte is replaced with a non-flammable inorganic solid electrolyte, which inherently mitigates these risks.

Besides the advantage on safety, ASSBs are also believed to provide a pathway toward higher energy density. Li metal, which has a high theoretical specific capacity of 3860 mAh $g^{-1}$, is expected to be used on the anode side of ASSBs. A Li-metal anode cannot be used in current LIBs due to the formation of dendrites and unstable SEI.[23] The formation of dendrites originates from the inhomogeneous electrodeposition of Li metal. The growth of Li-metal dendrites can destroy the SEI

and expose a fresh Li surface, which will further promote the inhomogeneous deposition of Li metal and form regenerative feedback. In this case, the uncontrolled growth of Li-metal dendrites can lead to short-circuiting, which may further result in fast exothermal reaction and battery fire. In addition, the exposed fresh Li continues to react with the liquid electrolyte, forming a new SEI, resulting in Li and electrolyte consumption. These two issues of Li metal can potentially be solved with the use of a solid electrolyte. The high modulus of the solid-electrolyte pellet might be able to prevent the propagation of Li dendrite. In addition, the wide stability window of some solid electrolytes can avoid the electrolyte consumption issue. Figure 1.4 shows the estimated volumetric and gravimetric energy density for ASSBs using a NMC622 cathode, $Li_3PS_4$ (LPS) SE, and Li-metal anode. With a high cathode loading (>80 wt % active material in the cathode composite) and a thin separator (<50 μm), ASSBs can have a significant energy density advantage over current LIBs, particularly in terms of volumetric energy density.[12]

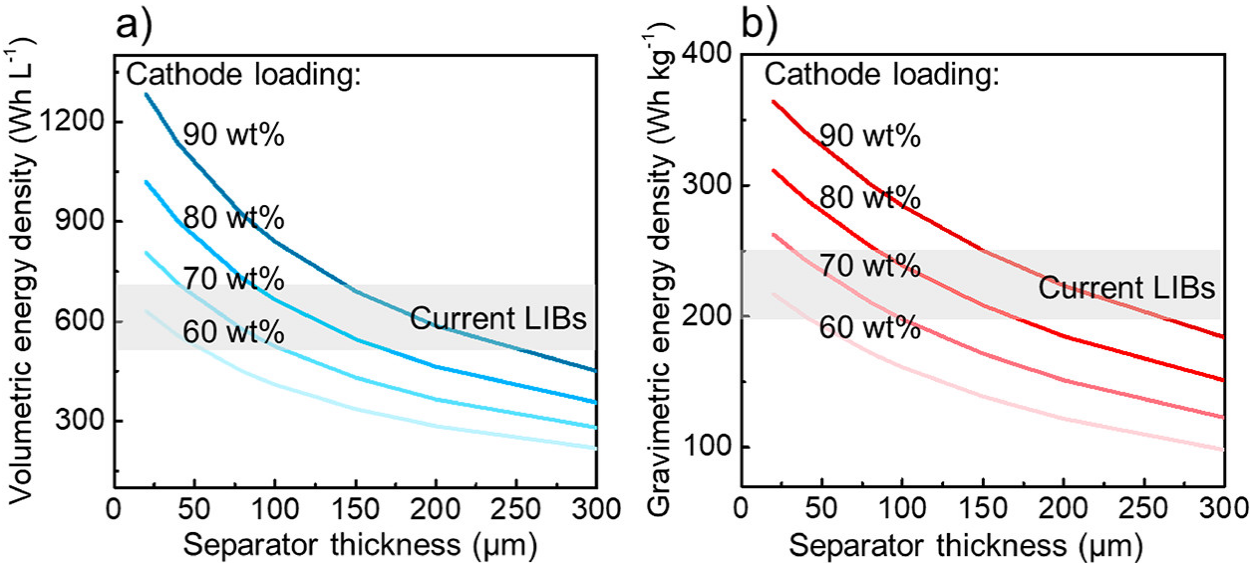


**Figure 1.4 Energy density comparison between ASSBs and LIBs**
Estimated cell-level (a) volumetric and (b) gravimetric energy density for ASSB using Li-metal anode with different cathode loadings and separator thicknesses compared with those of current LIBs. The model uses NMC622 as the cathode, 20% excess Li metal as the anode, and LPS as the SE. This figure is adapted and reproduced from ref. [12].

Additionally, a conventional liquid electrolyte with carbonate solvents would become oxidized at a voltage of slightly over 4V (vs. $Li^+/Li$), preventing the application of high-voltage cathode active materials.[24] In contrast, oxide and halide solid electrolytes typically have much higher electrochemical stability.

ASSBs with halide solid electrolytes can deliver high areal capacity (> 4 mAh $cm^{-2}$), high specific capacity (>190 mAh $g^{-1}$), and good cycling performance, even at a high cut-off potential of 4.8 V (vs. $Li^+/Li$).[25] Further improvement of the energy density for ASSBs can be achieved through the use of a bi-polar electrode stacking cell design. Figure 1.5 presents a schematic illustration of ASSBs with a bi-polar stacking cell design. Compared with the conventional cell design of LIBs, the bi-polar stacking allows the use of only one current collector per unit cell, which can reduce the overall current-collector thickness as well as the "dead volume" between unit cells.[26]

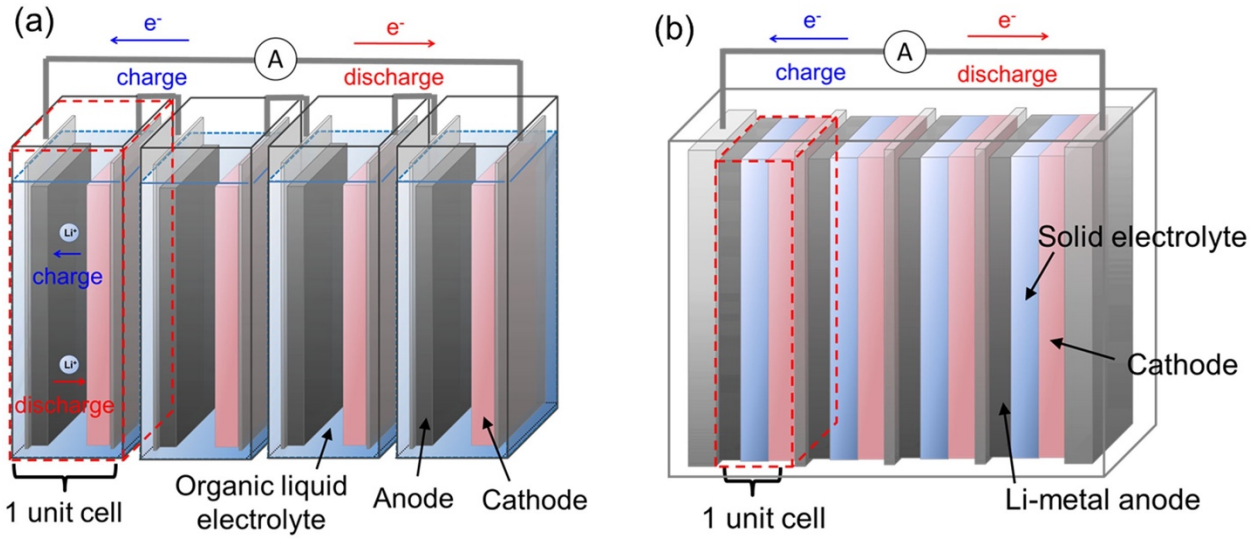


**Figure 1.5 Bi-polar electrode stacking cell design.**
Schematic of (a) conventional stacked LIBs using a liquid electrolyte and (b) bi-polar stacked ASSBs. This figure is adapted and reproduced from ref. [26]. Creative Commons (CC) License: CC BY 4.0

In addition, several solid electrolytes, including $Li_{10}GeP_2S_{12}$,[27] $Li_{9.54}Si_{1.74}P_{1.44}S_{11.7}Cl_{0.3}$,[28] and $Li_{6.6}Si_{0.6}Sb_{0.4}S_5I$,[29] have exhibited ionic conductivities higher than those of current liquid electrolytes at room temperature. Furthermore, it has been demonstrated that ASSBs using these solid electrolytes can be cycled under extremely high current rate (e.g., 18C).[28] In this context, ASSBs can potentially achieve higher power density than conventional LIBs, which is critical to fast charging and high peak power output.

## 1.3.3 Challenges in all-solid-state batteries

Despite the advantages mentioned in Part 1.2.2, ASSBs currently are not ready for commercialization. As shown in Figure 1.6, several scientific and engineering issues

must be resolved to realize high-energy-density ASSBs with long cycle life.[12] On the cathode side, many solid electrolytes, especially sulfide solid electrolytes, decompose or react with cathode active materials when charged to high voltage or upon co-sintering at high temperatures.[30,31] Additionally, the volume changes of cathode active materials during lithiation/delithiation could induce contact loss between the cathode and solid electrolyte, further resulting in capacity loss.[32,33]

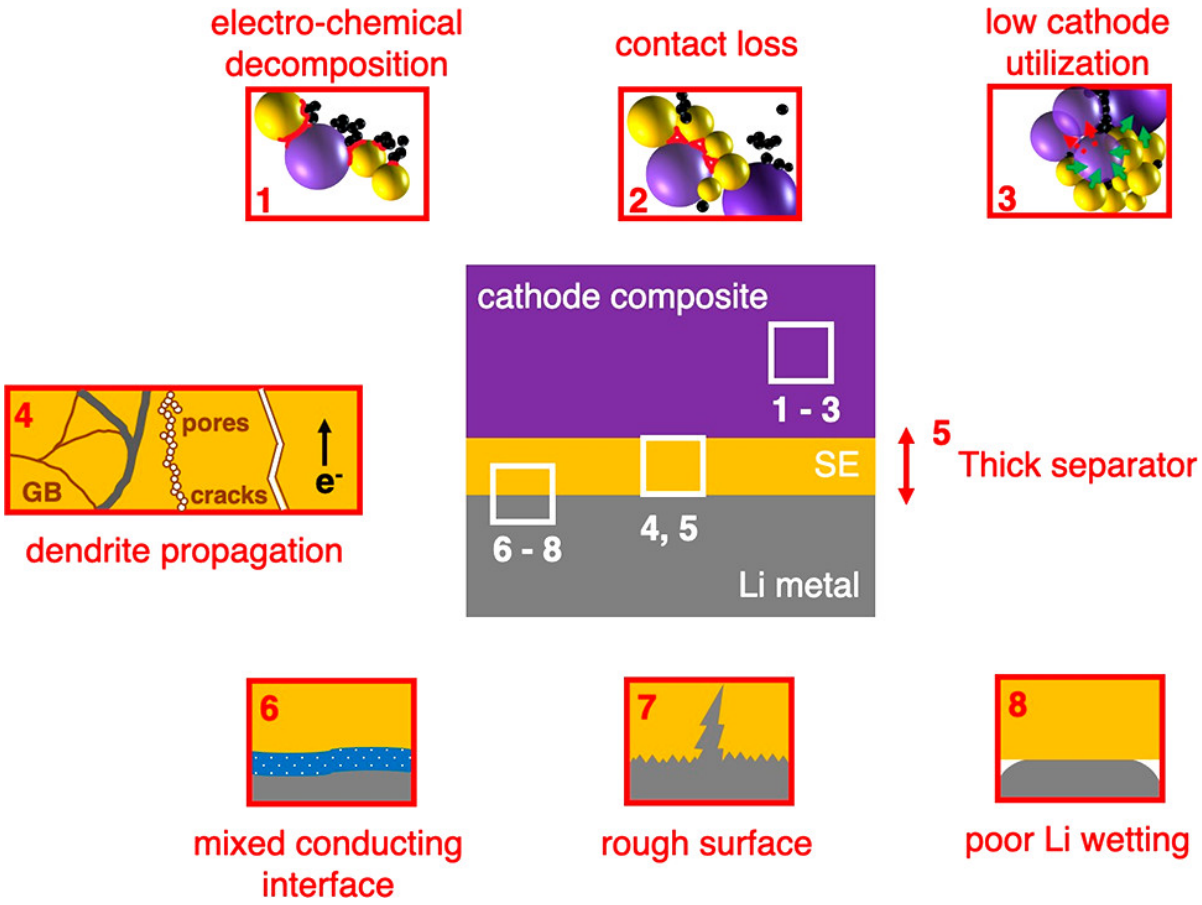


**Figure 1.6 Schematic illustration of the major issues in ASSBs.**

To maximize the volumetric energy density, the polymer separators in state-of-the-art LIBs are typically thinner than 10 $\mu$m. To achieve a competitive energy density compared with LIBs, the thickness of the solid electrolyte separator is expected to be less than 50 $\mu$m. Although several thin-film fabrication methods have been developed at the lab scale,[34–37] high-cost and low throughput prevent their application in large-scale production. This figure is adapted and reproduced from ref. [12].

On the anode side, the application of a Li-metal anode is essential to achieve high energy-density ASSBs. However, the extremely low reduction potential of Li metal makes the stability of solid-electrolyte contact challenging. It is important to design

a stable or self-passivating interface between the Li metal and solid electrolyte.[38] In addition, the rough surface of the solid electrolyte can induce inhomogeneous of Li deposition and further lead to the formation of Li dendrites. Although the high modulus of the solid electrolyte might constrain the growth of Li dendrites in the bulk, Li-metal dendrites could still penetrate the solid electrolyte through grain boundaries and particle boundaries.[39] In addition, some solid electrolytes have a lithiophobic surface which introduces a high interfacial resistance, limiting the rate performance and power density of ASSBs.[40]

## 1.4 Superionic conductors and solid electrolytes

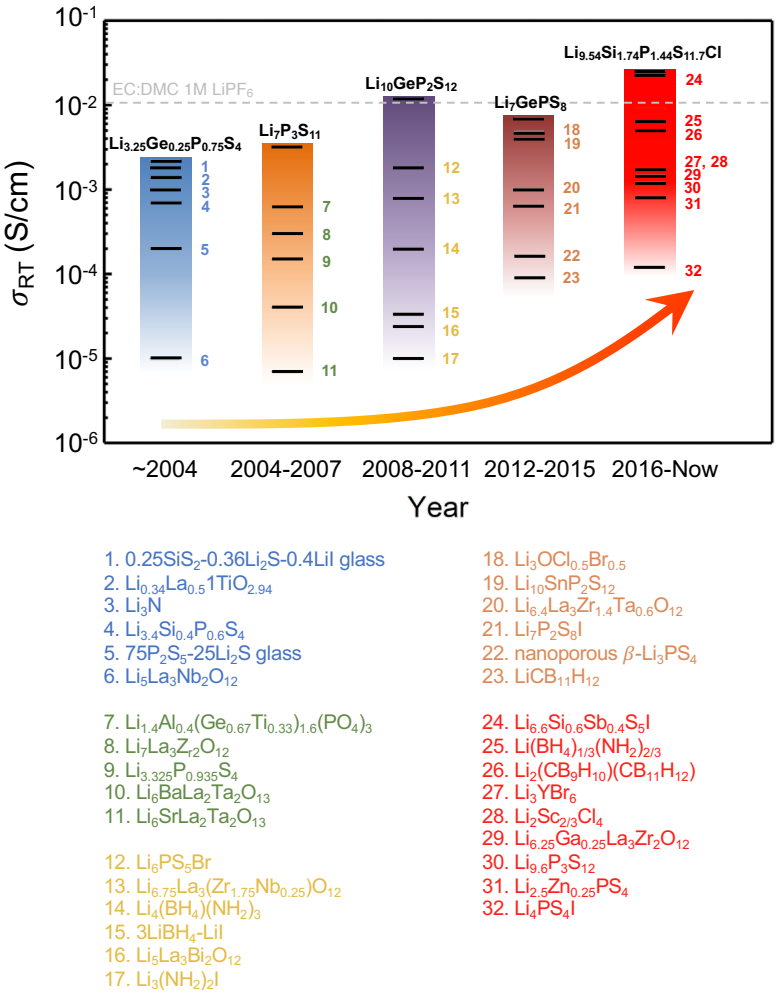


**Figure 1.7 Progress in the discovery of Li-ion superionic conductors.**
The room temperature ionic conductivities of representative Li-ion superionic conductors over time are plotted to demonstrate the improvement in ionic conductivity. This figure is adapted and reproduced from ref. [12].

From the perspective of materials design, one of the key factors in developing high-performance ASSBs is to explore fast ionic conductors (i.e., superionic conductors) with high ionic conductivity, low electronic conductivity, a wide stability window, and good processibility. During the past two decades, there has been an accelerated development of Li-ion superionic conductors. Figure 1.7 shows the recent progress made in Li-ion superionic conductors.[27,28,41–71] The ionic conductivity of many of these conductors, such as argyrodite-type materials, LISICON materials, and garnet-type materials, approaches or even surpasses that of currently used liquid electrolytes (~ $10^{-2}$ S/cm). The Li-ion migration mechanism in superionic conductors will be discussed in part 1.3.1. Two major types of superionic conductors (sulfide and oxide superionic conductors) will then be introduced in the following parts.

## 1.4.1 Ion transport in superionic conductors

Although a complete understanding of superionic conductivity is not yet available, it has been discovered that certain structural and chemical factors may result in high ionic conductivity. To understand how these factors affect the ionic conductivity, the ion-migration mechanism must first be explained. As shown in Figure 1.8, at the atomic scale, mobile cations (e.g., $Li^+$) need to pass through energy barriers to hop between the sites with local minimum energy (i.e., the grand-state stable site and intermediate metastable site). The energy used to overcome this barrier is labeled $E_m$. To enable the long-range diffusion of ions, the hopping with low activation energy must form a percolating network.

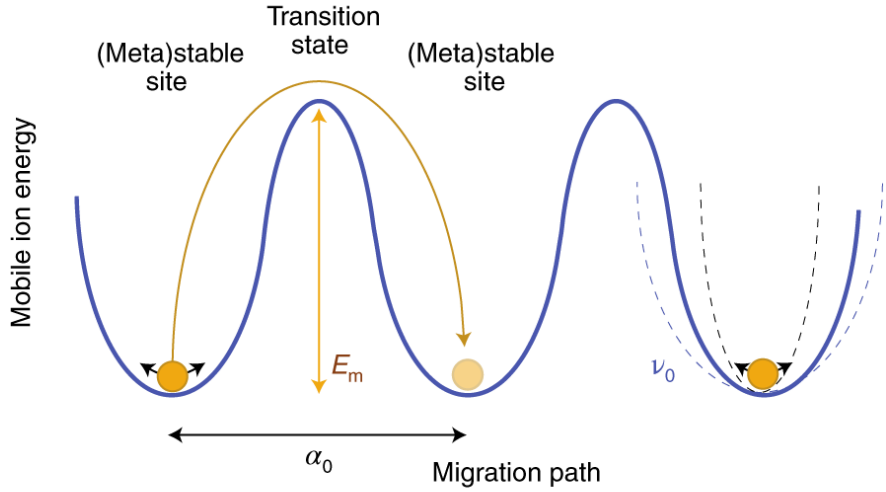


**Figure 1.8 Schematic illustration of energy landscape during ion migration.** This figure is adapted and reproduced from ref. [72].

The ionic conductivity ($\sigma$) in a solid is equal to the product of the charge (q), concentration (n), and mobility (u) of the charge carriers (equation 1.1):

$$\sigma = n\, q\, u\,. \tag{1.1}$$

Additionally, ion diffusion is a thermally activated process that can be described by a modified Arrhenius relationship (equation 1.2):

$$\sigma = \sigma_0 T^{-1} e^{-\frac{E_a}{k_B T}}, \tag{1.2}$$

where $\sigma_0$ is the pre-factor, T is the temperature, $E_a$ is the activation energy for ion diffusion, and $k_B$ is the Boltzmann constant. The activation energy $E_a$ consists of the defect formation energy ($E_f$) and the energy barrier for ion migration ($E_m$). $E_f$ corresponds to the energy used to form point defects, such as vacancies and interstitial ions, which are usually perceived as the mobile charge carriers in a crystalline solid. In addition, $E_m$ corresponds to the highest migration energy barrier along the conduction pathway. The pre-factor $\sigma_0$ is related to other details of the hopping process, such as the entropy of migration ($\Delta S_m$), the jump distance ($\alpha_0$), and the attempt frequency ($\nu_0$). For the simplest direct hopping, the pre-factor can be expressed as follows (equation 1.3):

$$\sigma_0 = z\nu_0\alpha_0^2 \frac{nq^2}{k_B} e^{-\frac{\Delta S_m}{k_B}}, \tag{1.3}$$

where z ($\leq 1$) is a geometric factor that depends on the directionality of the conduction mechanism. According to equation 1.2, the activation energy is the dominating factor controlling the ionic conductivity. The energy change along the ion-diffusion pathway is described by the energy landscape (Figure 1.8). In general, a flat energy landscape, where the displacement of the working ion only causes a small change in the structure energy, is beneficial to attain a low activation energy. One way to flatten the energy landscape is to minimize the coordination changes along the diffusion path. The coordination environment is highly correlated with the anion framework. As shown in Figure 1.9, in a body-centered cubic (BCC)-like anion framework, Li can directly hop between adjacent tetrahedral sites. In contrast, Li must hop along a tetrahedral–octahedral–tetrahedral path in other closed-packed anion frameworks, leading to a much larger energy barrier. Many sulfide-type superionic conductors with low activation energy, such as $Li_7P_3S_{11}$ and $Li_{10}GeP_2S_{12}$, indeed have a BCC anion framework.[73] However, the BCC anion framework

criterion does not work well for oxide-type superionic conductors. Because the oxide anion has a much smaller size and weaker screening power than the sulfide anion, besides the bare anion framework, the interactions between cations should also be considered when evaluating the migration energy in oxide-type superionic conductors. The structural features that benefit cation diffusion in oxide-type superionic conductors will be further discussed in Chapter 3.

Besides the anion framework, the anion chemistry can also be tuned to modify the cation migration in superionic conductors. Replacing a monatomic anion with a polyanion might introduce more degrees of freedom (e.g., rotational, and vibrational degrees of freedom) and/or reduce the interaction between working cation and its neighboring anions, which could further decrease the energy barrier. This strategy has been successfully applied to increase the ionic conductivity of sodium antiperovskite $Na_3OX$ (X = Cl, Br, I, etc.) by 4 orders of magnitude by substituting the halide anion with the $BH_4^-$ group.[74] However, the mechanism of this strategy still remains unclear. This strategy will be further discussed in Chapter 2 using the Li argyrodite system.

Another strategy to accelerate ion migration is to engineer the cation sites. Equation 1.1 and equation 1.3 show that the charge-carrier concentration is another important factor in determining the ionic conductivity of materials. This defect concentration can usually be tuned by aliovalent doping. For example, Ca doping can be used to create Na vacancies in cubic $Na_3PS_4$ to obtain a room-temperature ionic conductivity of $\sim$1 mS $cm^{-1}$ [75], and Zr doping has been reported to increase the ionic conductivity of $LiTaSiO_5$ by introducing interstitial Li ions.[76] However, the migration energy barrier could be decreased by pushing up the energy of stable cation sites. The site energy of mobile cations can be raised by introducing additional mobile ions into the pristine structure and forcing them to occupy high-energy sites. This phenomenon has been observed in garnet-type ionic conductors. $Li_7La_3Zr_2O_{12}$ exhibits an ionic conductivity of 0.3 mS $cm^{-1}$, whereas materials with the same garnet-type structure but lower Li concentrations, $Li_5La_3Nb_2O_{12}$ and $Li_3La_3Te_2O_{12}$, exhibit much lower ionic conductivities. As the Li concentration increases from x = 3 to x = 7 in garnet-type materials $Li_xLa_3M_2O_{12}$ (M = Te, Nb, Zr), more Li ions are pushed to the high-energy octahedral sites to minimize the interaction between adjacent Li ions, which further flattens the energy landscape and reduces the activation energy.[77]

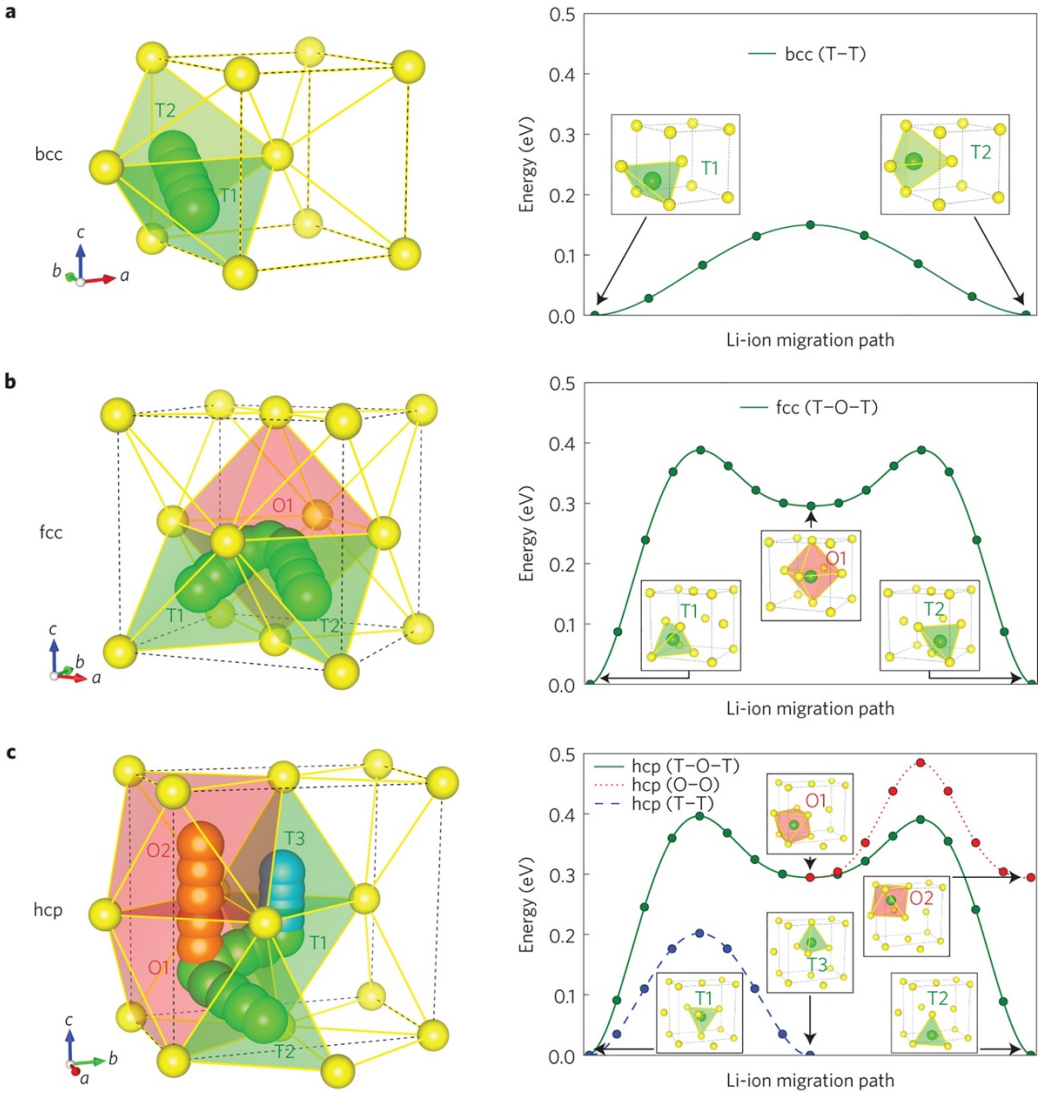


**Figure 1.9 Energy landscape in close-packed anion frameworks.**
The migration path (left panels) and related energy landscape (right panels) in (a) BCC, (b) FCC, and (c) HCP sulfur lattice. The sulfide anions are colored yellow, and the Li ions are colored green, blue and red for different paths. $LiS_4$ tetrahedra and $LiS_6$ octahedra are colored green and red, respectively. This figure is adapted and reproduced from ref. [73].

## 1.4.2 Sulfide-type solid electrolytes

Sulfide-type superionic conductors offer a huge advantage in terms of ionic conductivity because of the large ionic size and high polarizability of sulfide anions. Besides the high bulk conductivity, sulfide-type solid electrolytes also possess fairly low boundary resistance. A good total ionic conductivity can be easily achieved

through cold pressing, which makes sulfide-type solid electrolytes easy to process. As shown in Figure 1.7, sulfide glasses were first investigated as lithium-ion conductors. Most sulfide glasses systems consist of $Li_2S$ and sulfide-based network formers, such as $SiS_2$, $GeS_2$, or $P_2S_5$.[78–80] Lithium halides have also been used as additives to increase the lithium concentration and conductivity of the glasses. During the development of sulfide glasses electrolytes, it was discovered that crystal phases with higher conductivity could be formed in the glass phase. This type of composite is usually called a glass-ceramic. Most works on glass-ceramic sulfide electrolytes have been performed using the $xLi_2S–(100–x)P_2S_5$ system. In this system, depending on the value of x, various phases can be formed during the crystallization. For $x < 70$, low-conductivity phases, such as $Li_3PS_4$ and $Li_4P_2S_6$, are precipitated and decrease the conductivity of the glass-ceramic.[81] For $x \geq 70$, the high-conductivity phases $Li_7P_3S_{11}$ and $Li_{3.25}P_{0.95}S_4$ are created and significantly increase the conductivity from $10^{-5}$ S/cm to $10^{-3}$ S/cm.[44]

Although good conductivities have been obtained in glass and glass-ceramic systems, the study of the migration mechanism remains very limited for amorphous-phase system. Most of the design principles for glasses and glass-ceramics are empirical, which prevents the discovery of new glass/glass-ceramic conductors. In contrast, more crystalline sulfides with well-defined conduction pathways have been shown to have superior conductivities. The room-temperature conductivity of thio-LISICON $Li_{10}GeP_2S_{12}$ can reach up to $1.2 \times 10^{-2}$ S/cm.[27] and can be further increased to $2.5 \times 10^{-2}$ S/cm by Si and Cl doping, even surpassing the ionic conductivity of conventional liquid electrolytes.[28] Another widely explored crystalline sulfide electrolyte is the Li argyrodites with a prototype composition of $Li_7PS_6$. Part of the sulfur in the Li argyrodite structure is loosely bonded and easy to substitute with halogens. Additionally, halogen substitution has a great effect on the Li diffusion in the argyrodite structure with the ionic conductivity of halogen-substituted argyrodite-type materials varying from $10^{-6}$ to $10^{-2}$ S/cm.[82–85] Based on this property, the Li-argyrodites system will be used to investigate the effect of pseudo-halogen substitution in Chapter 2.

### 1.4.3 Oxide-type solid electrolytes

Compared with sulfide solid electrolytes, oxide solid electrolytes generally exhibit a wider electrochemical stability window and improved chemical stability with cathode active materials.[86–88] However, the ionic conductivities of oxide solid electrolytes are generally lower than those of sulfide solid electrolytes. In addition, high-temperature sintering is always required to densify the oxide solid electrolytes

and reduce the boundary resistance. Garnet-type, NASICON-type and perovskite-type conductors are three types of oxide solid electrolytes that have been widely investigated. Within the family of garnet-type conductors, cubic $Li_7La_3Zr_2O_{12}$ (LLZO) is considered the most promising candidate owing to its high room-temperature conductivity (> $10^{-4}$ S/cm) and high stability against Li metal. Compared with cubic LLZO, tetragonal LLZO is more thermodynamically stable. However, the ionic conductivity of tetragonal LLZO is two orders lower than that of the cubic phase.[89] To stabilize the highly conductive cubic phase, most efforts have been focused on aliovalent doping. The stabilization of the cubic phase originates from the increased Li sublattice disorder caused by the Li vacancies created by aliovalent substitution.[90] NASICON-type materials have a formula of $AM_2(PO_4)_3$, where the A site is occupied with alkali cations, such as $Li^+$ and $Na^+$, and the M site is occupied by high-valence cations. $LiTi_2(PO_4)_3$ is one of the most widely investigated NASICON-type Li-ion conductors. By substituting $Ti^{4+}$ with $Al^{3+}$, the conductivity of $Li_{1.2}Al_{0.2}Ti_2(PO_4)_3$ (LATP) can reach $5 \times 10^{-3}$ S/cm. However, LATP is not stable against a Li-metal anode because of the presence of $Ti^{4+}$.[91] The general formula for perovskite-type materials is $ABO_3$. The most well-known perovskite-type Li-ion conductor is $Li_{3x}La_{2/3-x}TiO_3$ (LLTO) with the A site partially occupied by Li/La. The vacancy concentration and cation disordering at the A site have a great effect on the ionic conductivity of LLTO.[92] Although LLTO exhibits a high bulk conductivity up to $10^{-3}$ S/cm, it is difficult to reduce the grain-boundary resistance. The total conductivity of LLTO is only $10^{-4}$ - $10^{-5}$ S/cm, which is 1–2 orders of magnitudes lower than the bulk conductivity.[93]

## 1.5 Dissertation overview

This dissertation explores new superionic conductors, prepared through composition modification and structural design, that can be used as solid electrolytes in ASSBs. Chapter 2 focuses on exploring new sulfide solid electrolytes prepared through composition modification. A combined theoretical and experimental approach was used to explore the possibility of enhancing the ionic conductivity through pseudohalogen substitution in the Li-argyrodite structure. Chapter 3 discusses the crystal-structure features that benefit the Li-ion migration in oxide superionic conductors. We reveal that corner-sharing connectivity of the oxide crystal framework increases the ionic conductivity. A new selenate-type fast Li-ion conductor was predicted and experimentally demonstrated. Chapter 4 summarizes the main findings of the dissertation and provides an outlook for superionic conductors and solid-state batteries.

# Chapter 2 Pseudohalogen-substituted Li argyrodite superionic conductor

## 2.1 Foreword

The work presented in this chapter was published in Sun, Y., Ouyang, B., Wang, Y., Zhang, Y., Sun, S., Cai, Z., Lacivita, V., Guo, Y. and Ceder, G., 2022. Enhanced ionic conductivity and lack of paddle-wheel effect in pseudohalogen-substituted Li argyrodites. *Matter*. DOI: 10.1016/j.matt.2022.08.029, and is reproduced here with the permission of co-authors.

## 2.2 Abstract

Superionic conductors are key to the development of safe and high-energy-density all-solid-state batteries. Using a combined theoretical and experimental approach, we explore the feasibility of increasing the ionic conductivity through pseudohalogen substitution in the Li argyrodite structure. Under the guidance of calculated thermodynamic stability, $BH_4$-substituted Li argyrodite, $Li_{5.91}PS_{4.91}(BH_4)_{1.09}$, was successfully synthesized via a mechanochemical method. As-synthesized $BH_4$-substituted Li argyrodite displays an ionic conductivity of 4.8 mS/cm at 25 $^oC$. Ab initio molecular dynamics simulation trajectory analysis was used to investigate how $BH_4$ facilitates Li-ion diffusion and indicates only a weak correlation with the B-H bond motion. We find that the enhanced conductivity mainly originates from the weak interaction between Li and $BH_4$ and find no evidence of a paddle-wheel effect from the polyanion. This work provides insight on how cluster ions enhance Li diffusion and systematically describes how to explore superionic conductors with pseudohalogen substitution.

## 2.3 Introduction

The application of solid-state electrolytes provides opportunities for batteries that are safer and more powerful than current state-of-the-art Li-ion batteries.[94,95] Driven by the demands for solid-state electrolytes, there has been a rapidly growing interest in the discovery of solid-state alkali ionic conductors with ionic conductivities equal to or higher than those of liquid electrolytes.[60,96–101]

Although most recent work for improving ionic conductivity has focused on substituting cation sites,[101–104] less work has been done on modifying the anion chemistry though their framework is known to be important for ionic conductivity.[100] In this paper we focus on cluster-ion substitution as it provides an option for engineering the anion framework. Compared with single-ion substitution, cluster-ion substitution provides more degrees of freedom including bond stretching and bond bending, which may assist alkali-metal to preserve their coordination as much as possible as they migrate through the transition state, a factor which is important in the migration of many cations.[100,105] To date, it remains unclear whether and how these additional degrees of freedom lead to higher conductivity, even though high conductivities have been reported in several recent studies.[106–111] Specifically, several-orders-of-magnitude enhancement in the ionic conductivity has been reported in both theoretical and experimental work applying cluster-ion substitution in antiperovskite-type materials.[109–111] The cluster ions used in those reports can be classified as pseudohalogen anions, as the formal charge of such cluster ions equals that of a halogen, and the strong covalent interactions within such a cluster ion cause it to behave as a unit. Considering the frequent appearance of halogens in fast-ionic conductors, it is important to understand how pseudohalogen substitution influences ionic conductivity.

The argyrodite structure is a good framework to study the pseudohalogen effect as it already has reasonable conductivity with the presence of regular halogens.[97,112–115] As the halogen site in argyrodite has only mobile $Li^+$ in its first coordination shell, it is loosely bonded with the rest of the framework creating the expectation that it may be easier to substitute.[83,96] The most widely studied argyrodites are derived from halogen substitution in the $Li_7PS_6$ argyrodite prototype, which yields various forms of $Li_6PS_5Cl$, $Li_6PS_5Br$, and $Li_6PS_5I$. Halogen substitution has been reported to have a beneficial effect on the diffusion of Li ions with the ionic conductivity of halogen-substituted argyrodite-type materials varying from $10^{-3}$ mS/cm to 10 mS/cm.[83,84,97,116–119]

In this work, we explore the feasibility of enhancing the ionic conductivity through pseudohalogen substitution in the Li argyrodite system using a combined theoretical and experimental approach including first-principles stability analysis, solid-state synthesis, structure characterization, and ab initio molecular dynamic (AIMD) analysis. A computational screening of potential Li argyrodite pseudohalides to determine the synthetically accessible argyrodite pseudohalides points at $BH_4$-substituted Li argyrodites as the most stable pseudohalides. An argyrodite-type material with the composition $Li_{5.91}PS_{4.91}(BH_4)_{1.09}$ was successfully synthesized using a mechanochemical method and shown to have a high ionic conductivity of

4.8 mS/cm at room temperature, considerable higher than that of conventional halogen-substituted Li argyrodites.

When explaining the effect of polyanions/cluster anions on Li-ion diffusion, most recent work has centered on whether there is a synergistic effect between the polyanions and Li diffusion (the so-called "Paddle-Wheel" effect).[108,111,120–122] Our theoretical analysis shows that the motion of Li ions has only a weak relationship with any motion of the $BH_4$ anion. Hence, rather than appealing to a "paddle-wheel" effect we argue that the enhanced conductivity mainly originates from the Li–pseudohalogen interaction which is weaker than the Li-halogen (Cl, etc.). As a result, Li ions are trapped for a shorter time near the pseudohalide groups and diffuse faster. This finding also indicates that the origin of higher conductivity in the argyrodite structure with pseudohalogen substitution is the flattening of the energy landscape with the introduction of light and highly covalent cluster ions, rather than any "dynamical coupling" between Li diffusion and polyanion rotation, as has been speculated in the literature. Our study provides a mechanistic understanding of how pseudohalogen substitution can help increase Li-ion conductivity, shedding light on design strategies for optimizing ionic conductivity by engineering the anion framework of conductors.

## 2.4 Results

### 2.4.1 Crystal structure and phase stability

The general (pseudo)halogen-substituted argyrodite is reported to have a crystal structure with cubic symmetry as shown in Figure 2.1A. Three crystallographic positions in the argyrodite structure, 4a, 4c, and 16e, are associated with sulfur ions. The 4b site is occupied by P which binds 4 S ions to it into a $PS_4$ group. In contrast, the 4a and 4c sites are occupied by S atoms which are relatively far away from all other non-Li atoms (> 4 Å) and are not considered to be part of a covalent bond complex. As a result, sulfur in the 4a and 4c sites is usually easier to substitute.[116]

To understand the compositional range over which different Li argyrodite pseudohalides can exist, five pseudohalide ions were considered for substitution on 4a and/or 4c. Four types of substitution are considered, distinguished by their site occupancy (shown in Figure 2.1B). The first three types of substitution form $Li_6PS_5X$ (X = halogen or pseudohalogen), which corresponds to the occupancy of a (pseudo)halogen on either the 4a or 4c site, or half occupancy on both the 4a and 4c

sites. In the fourth type, both the 4a and 4c sites are fully substituted by the (pseudo)halogen, leading to the composition $Li_5PS_4X_2$ (X = halogen or pseudohalogen).

A

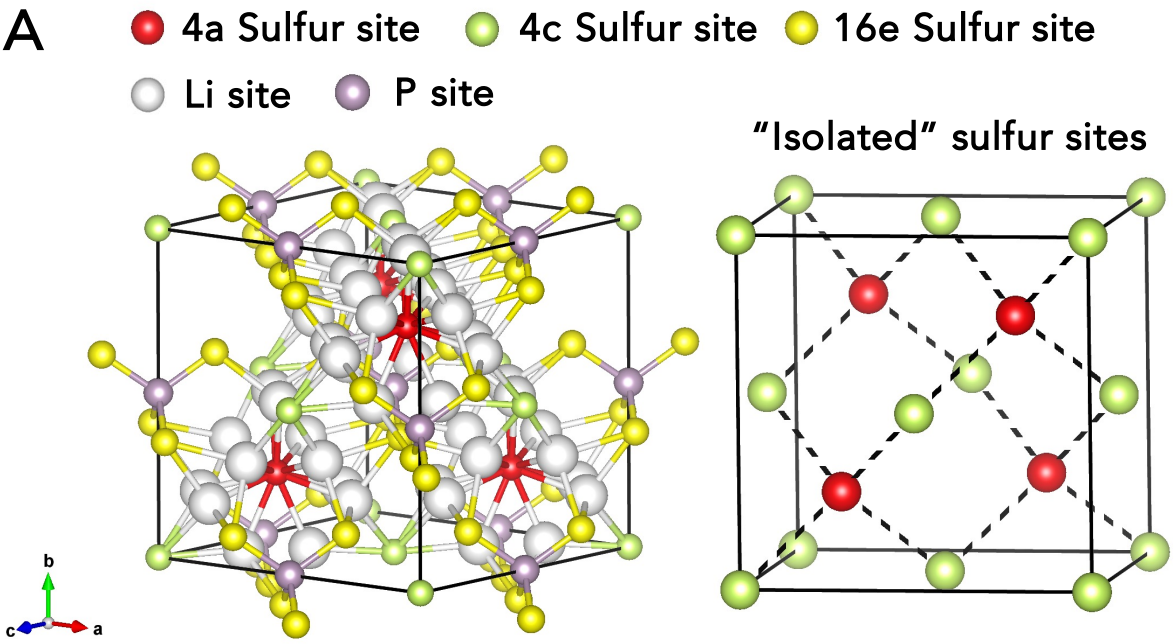


B

| Configuration | $Li_6PS_5X$ (4a) | $Li_6PS_5X$ (4c) | $Li_5PS_4X$ (Mixed) | $Li_6PS_5X_2$ (4a & 4c) |
|---|---|---|---|---|
| 4a Site | 1.0 | 0.0 | 0.5 | 1.0 |
| 4c Site | 0.0 | 1.0 | 0.5 | 1.0 |

**Figure 2.1 Crystal structure of lithium argyrodite.**
(A) General structure of argyrodite with different sulfur sites distinguished by colors (4a with red, 4c with green, and 16e with yellow). (B) Sulfur site occupancy for four types of substitution.

To evaluate the energy of these compounds, we enumerated the 10 possible Li arrangements across the 48h sites (denoted as the Li site) and picked the one with lowest DFT energy. We did not consider possible occupancy of Li in other sites, such as 48h', 16e, and 24g because we find that the change in energy of our structures when moving a Li from 48h to 48h' is small (see Supplemental Table 2.1),

and will therefore not significantly influence relative phase stability, but including it in all calculations would require unnecessarily large supercells. For each Li-Vac configuration on the 48h sites, the S-(pseudo)halogen ordering with lowest electrostatic energy was selected for DFT calculations. The orientation of the pseudohalogen was initialized by rotating the pseudohalogen until the average interatomic distance between the cluster ions and the neighboring cations is maximized. The phase stability was evaluated by comparing the energy of the substituted argyrodites to that of all the possible combinations of competing phases (the convex hull construction).[123]

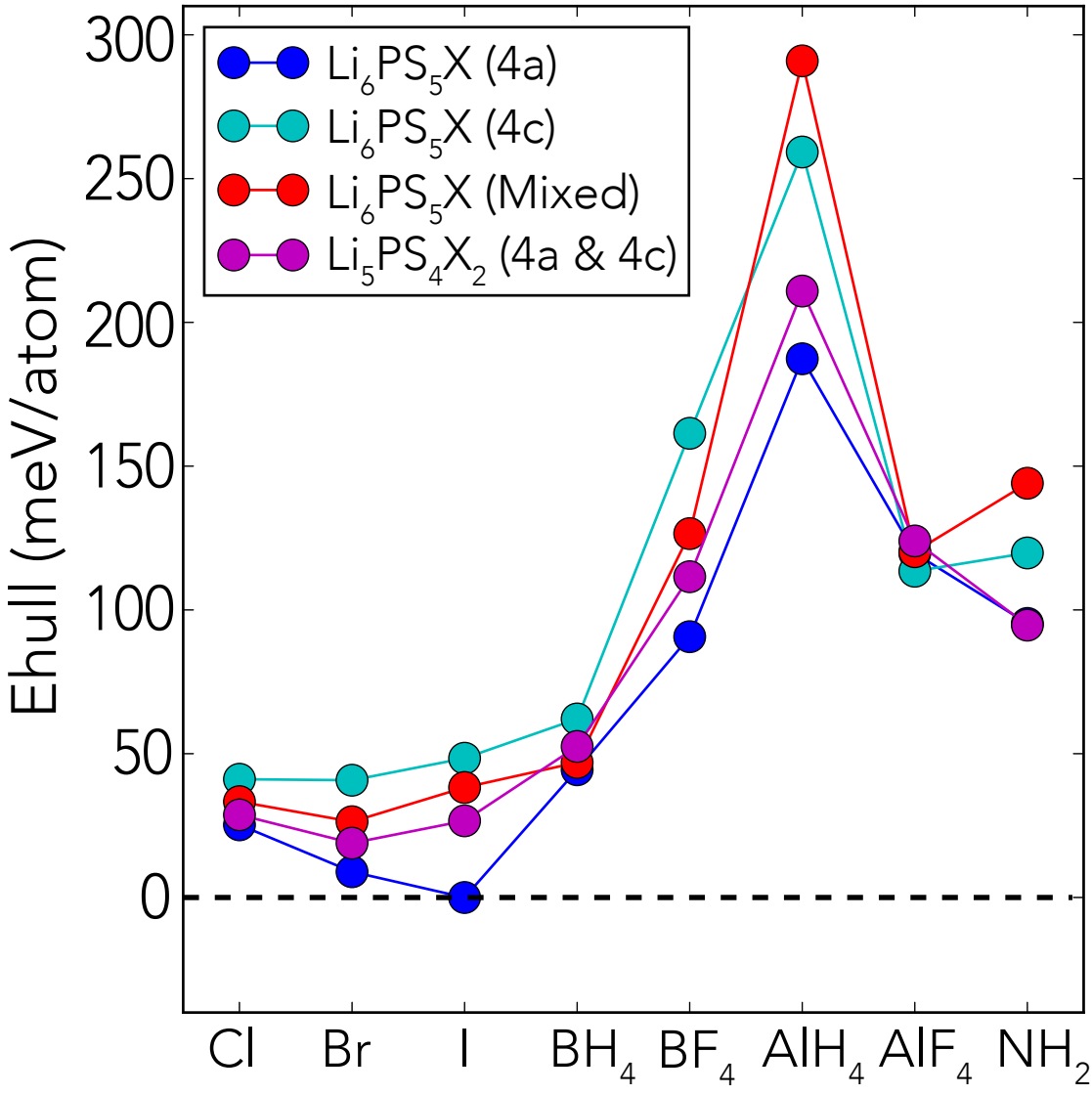


**Figure 2.2 Phase stabilities of Li argyrodites with different (pseudo-)halogen substitutions**

Figure 2.2 shows that most argyrodites have non-zero energy above the convex hull ($E_{hull}$), indicating that at 0 K, they are not a thermodynamic ground state. However, the halide versions of the argyrodites, such as $Li_6PS_5Cl$ and $Li_6PS_5Br$, have been synthesized[96], indicating that they can be stabilized by entropy, as is the case for other fast ion conductors,[124,125] or that metastable synthesis pathways to their formation exist[126]. It should be mentioned that we only use the $E_{hull}$ values to indicate the relative stability of argyrodites with different (pseudo)halogen substitutions. An argyrodite with a low $E_{hull}$ value does not necessarily guarantee synthetic accessibility. To give an example, $Li_5PS_4X_2$ (X=Cl, Br, I) has never been reported experimentally in literature. This is consistent with a broad analysis of metastable compounds which indicates that while low $E_{hull}$ is required for possible existence of metastable compounds, it is not a sufficient condition.[126]

The phases that compete for phase stability for each argyrodite are given in Table 2.1. Most of these are stoichiometric phases, implying that they will not generate much configurational entropy at non-zero temperature, and hence will create more favorable conditions for the formation of the argyrodite at higher temperature.

**Table 2.1 Competing phases for $BH_4$ substitution and halide substitution.**

| Materials | Competing Phases | Materials | Competing Phases |
|---|---|---|---|
| $Li_6PS_5BH_4$ | $LiSH + Li_2S + BP$ | $Li_6PS_5X$ (X=Cl, Br, I) | $Li_3PS_4 + Li_2S + LiX$ |
| $Li_5PS_4(BH_4)_2$ | $LiBH_4 + LiSH + BP$ | $Li_5PS_4X_2$ (X=Cl, Br, I) | $Li_3PS_4 + Li_2S + LiX$ |

## 2.4.2 Synthesis and Characterization

Our ab initio results indicate that $BH_4$-substituted argyrodites have the lowest $E_{hull}$ among the pseudohalogen substituted compounds, making them likely candidates for synthesis. In addition, Sakuda et al. recently reported that an argyrodite phase appeared in the $(100-x)(0.75Li_2S{\cdot}0.25P_2S_5){\cdot}xLiBH_4$ mixture with $x \geq 43$.[127] So, we set $BH_4$-substituted argyrodites as our target materials. $\beta$-$Li_3PS_4$, which is a metastable phase at room temperature, was used as precursor to increase the thermodynamic driving force for the formation reaction of the pseudohalide argyrodite. In addition, the $Li_3PS_4$ precursor has the $PS_4$ groups preformed, which may make it easier to form the argyrodite. Because $LiBH_4$ decomposes at high

temperature,[128] a heating process is not suitable for this reaction. Instead, a mechanochemical method using high-energy ball milling (SpexSamplePrep 8000M Mixer/Mill, 1425 RPM) was used. To prevent the sample temperature from becoming too high, the ball milling was interrupted for 15 min after every 30-min milling. In addition, we find that excess $LiBH_4$ is necessary to the synthesis of $BH_4$-substituted argyrodite since $LiBH_4$ is easily oxidized and consumed during the synthesis. When the precursors were mixed in the stoichiometric ratio of $Li_6PS_5BH_4$ ($\beta$-$Li_3PS_4$ : $LiBH_4$ : $Li_2S$ = 1: 1 : 1), no argyrodite phase was formed in the product (Supplemental Figure 2.1).

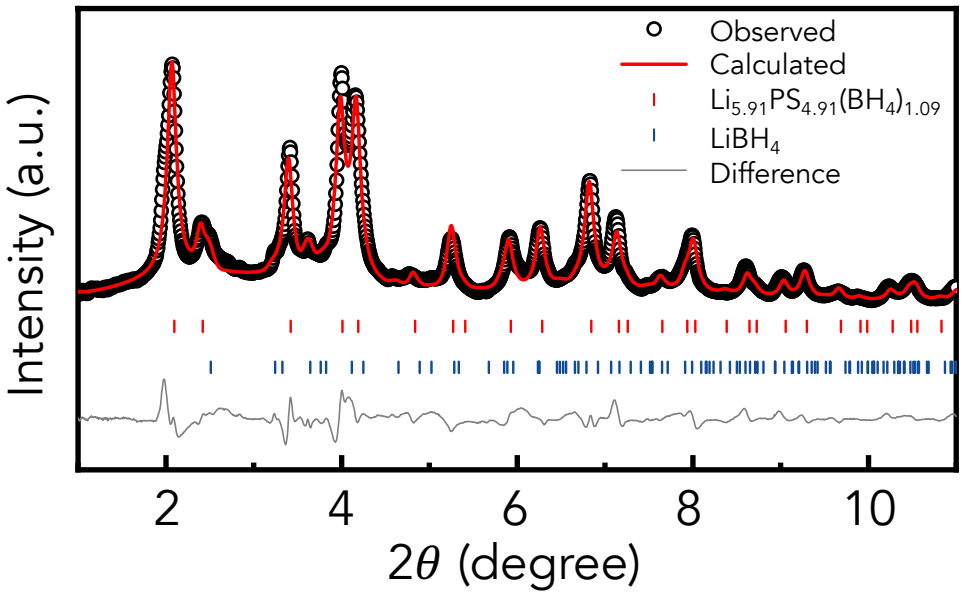


**Figure 2.3 Synchrotron XRD pattern of as-synthesized $BH_4$-argyrodite.**

Synchrotron X-ray diffraction (XRD) (shown in Figure 2.3) was conducted to confirm that an argyrodite phase was formed with a small amount (~2.8 wt %) of remaining $LiBH_4$. The synchrotron XRD pattern was refined using the Rietveld method with the TOPAS V6 software package to determine the lattice parameters, atomic positions, and occupancies. The best fits were obtained when the $BH_4^-$ and $S^{2-}$ ions are assumed to be disordered over the 4a site and 4c site. As shown in Table 2.2, the refined B occupancies of the 4a and 4c sites are 0.584 and 0.506, respectively, indicating that the chemical formula of the as-synthesized $BH_4$-substituted argyrodite is $Li_{5.91}PS_{4.91}(BH_4)_{1.09}$.

**Table 2.2 Atomic site information for BH4-substituted Li argyrodite based on Rietveld refinement of synchrotron XRD data**

| Atom | Wyckoff position | x | y | z | $B_{iso}$ / Å$^2$ | Site occupancy |
|---|---|---|---|---|---|---|
| Li1 | 48h | 0.3053(2) | 0.3053(2) | 0.0024(8) | 4 | 0.334(4) |
| Li2 | 24g | 0.75 | 0.0386(4) | 0.25 | 4 | 0.315(9) |
| B1 | 4a | 0 | 0 | 0 | 4.2(4) | 0.584(8) |
| S1 | 4a | 0 | 0 | 0 | 4.2(4) | 0.416(8) |
| B2 | 4c | 0.25 | 0.25 | 0.25 | 4.2(4) | 0.506(7) |
| S2 | 4c | 0.25 | 0.25 | 0.25 | 4.2(4) | 0.494(7) |
| P1 | 4b | 0.5 | 0.5 | 0.5 | 3.6(6) | 1 |
| S3 | 16e | 0.6200(7) | 0.6200(7) | 0.6200(7) | 3.6(6) | 1 |
| H1 | 16e | 0.0761(1) | 0.0761(1) | -0.0761(1) | 1 | 0.584(8) |
| H2 | 16e | 0.1739(1) | 0.1739(1) | 0.1739(1) | 1 | 0.506(7) |

Space group: F-43m, Lattice parameter: a = 10.0112(7) A, R-factor: Rwp = 7.63%

Transmission electron microscopy (TEM) electron diffraction (ED) patterns of the as-synthesized materials are presented in Figure 2.4A. The diffraction spots match with the calculated diffraction rings of the argyrodite structure, confirming the formation of the argyrodite phase. STEM energy dispersive spectroscopy (EDS) mapping images are presented in Figure 2.4B and indicate a homogeneous distribution of B throughout the particles, further corroborating the bulk substitution of $BH_4$.

To confirm the successful incorporation of the $BH_4^-$ unit, we also measured the Raman response of the argyrodite electrolytes and their precursors. The $BH_4^-$ internal stretching modes have characteristic frequencies residing in the 2200cm$^{-1}$ to 2400cm$^{-1}$ region, allowing for easy and unambiguous identification. As shown in Figure 2.5, we observed the $BH_4^-$ stretching modes in the $Li_{5.91}PS_{4.91}(BH_4)_{1.09}$ sample and in the $LiBH_4$ positive control compound, whereas in the $\beta$-$Li_3PS_4$ and $Li_6PS_5Cl$ negative control compounds, the $BH_4^-$ stretching region is spectrally silent. The presence of the $BH_4^-$ stretching modes provides further evidence that the $BH_4^-$ is successfully incorporated into the argyrodite electrolyte.

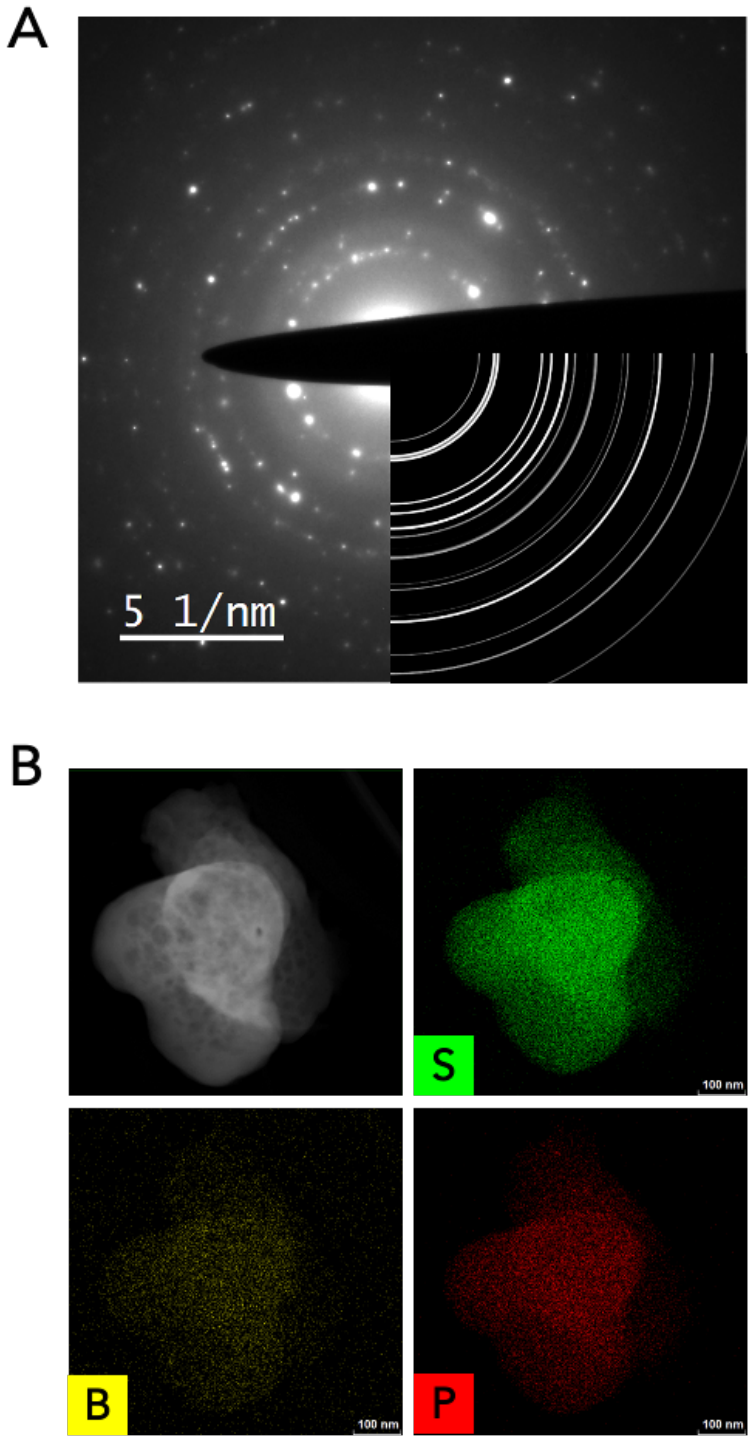


**Figure 2.4 Electron microscopy characterization of $BH_4$-argyrodite.**
(A) Electron diffraction pattern of as-synthesized $BH_4$-argyrodite. Calculated diffraction rings of the argyrodite structure are shown in the bottom right corner. (B) STEM/EDS mapping of the element distribution in a representative particle cluster of the $BH_4$-argyrodite (scale bar: 100 nm).

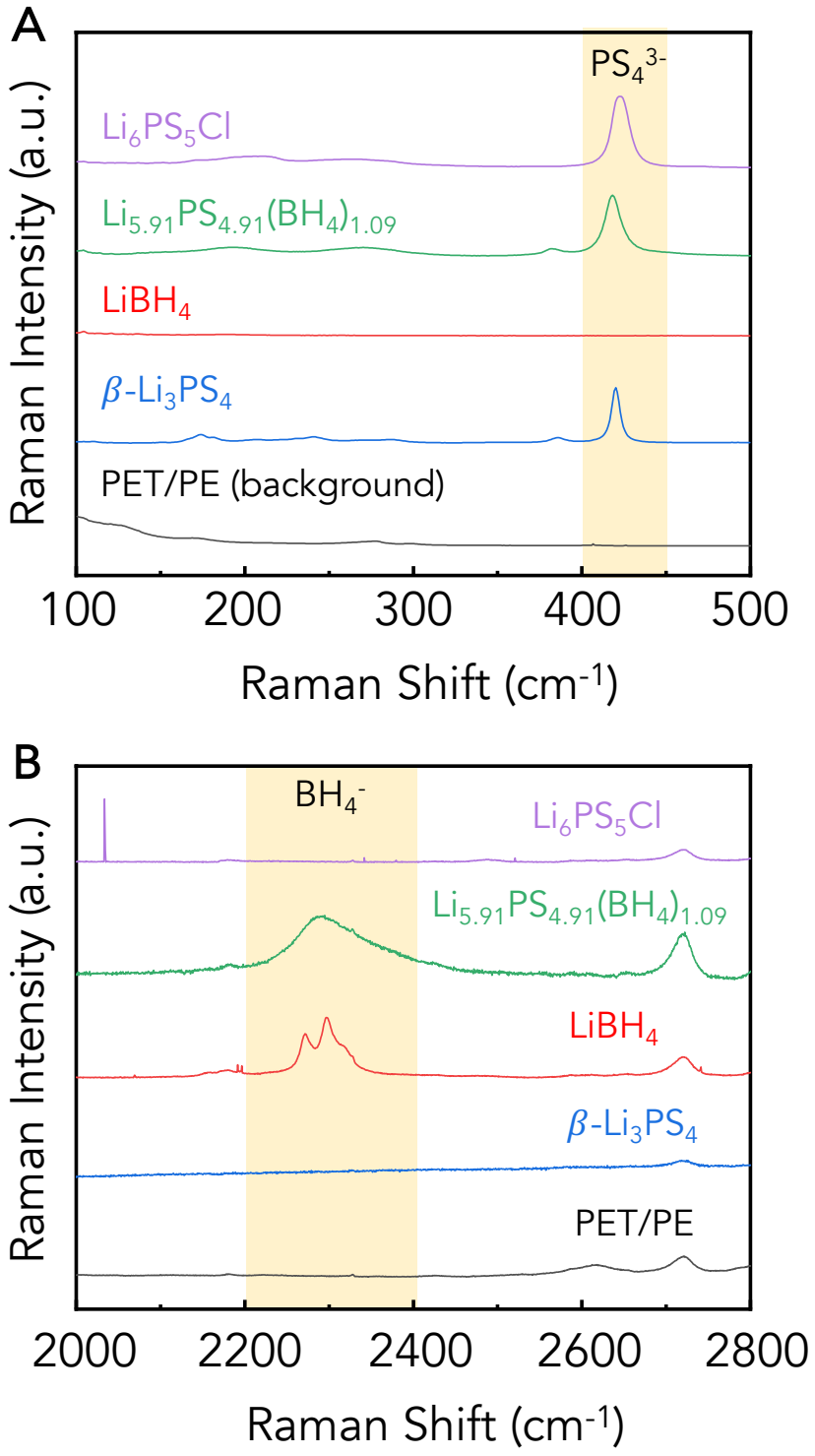


**Figure 2.5 Raman spectroscopy of $BH_4$-argyrodite.**
Raman spectra of $Li_6PS_5Cl$, $Li_{5.91}PS_{4.91}(BH_4)_{1.09}$, $LiBH_4$, $\beta$-$Li_3PS_4$, and PET/PE in the (A) 100 $cm^{-1}$ to 500 $cm^{-1}$ region and (B) 2000 $cm^{-1}$ to 2800 $cm^{-1}$ region.

### 2.4.3 Electrochemical Performance

Electrochemical impedance spectroscopy (EIS) measurements were performed to determine the ionic conductivity of the cold-pressed $Li_{5.91}PS_{4.91}(BH_4)_{1.09}$ with the results shown in Figure 2.6. The impedance data was fit with an equivalent circuit consisting of one parallel constant phase element (CPE)/resistor in series with a CPE. In the $Li_{5.91}PS_{4.91}(BH_4)_{1.09}$ sample, the response of the CPE/resistor has shifted to frequencies that are too high to measure with the impedance analyzer, and only the tail of the blocking electrode was used for the fit. The EIS results indicate a room-temperature (RT) ionic conductivity of 4.8 mS/cm. This value is several orders of magnitude higher than that of the precursor β-$Li_3PS_4$ and $LiBH_4$ (Supplemental Figure 2.2), ensuring that we did not measure the conductivity of the remaining β-$Li_3PS_4$ and $LiBH_4$ precursors.

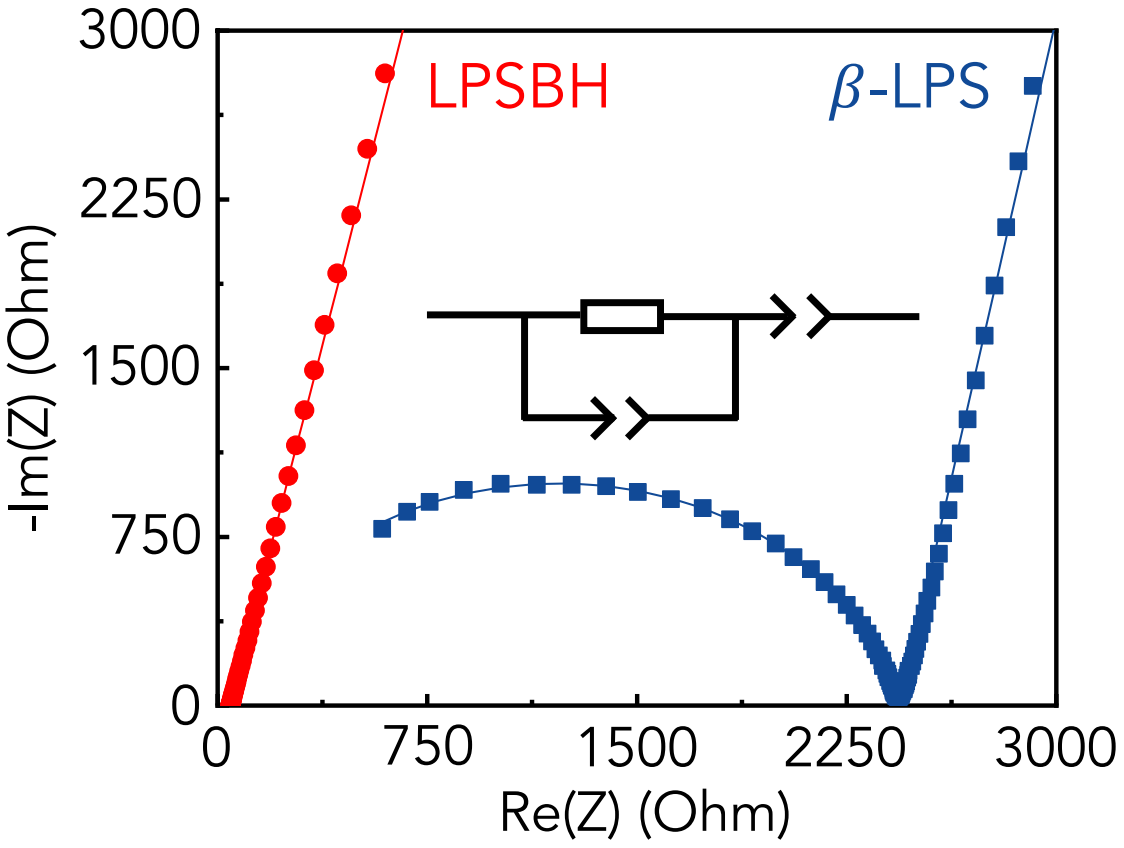


**Figure 2.6 Electrochemical impedance spectroscopy (EIS) of $BH_4$-argyrodite.** EIS plots of $Li_{5.91}PS_{4.91}(BH_4)_{1.09}$ (LPSBH, red points) and $\beta$-$Li_3PS_4$ ($\beta$-LPS, blue points) at room temperature.

The EIS of $Li_{5.91}PS_{4.91}(BH_4)_{1.09}$ at different temperatures are plotted in Figure 2.7. The Arrhenius plots of the $BH_4$-substituted Li argyrodite ($Li_{5.91}PS_{4.91}(BH_4)_{1.09}$) and conventional halogen-containing Li argyrodite ($Li_6PS_5Cl$ and $Li_6PS_5Br$) are compared in Figure 2.8. The RT ionic conductivity of the $BH_4$-substituted Li argyrodite is ~5 times higher than that of $Li_6PS_5Cl$ (0.95 mS/cm) and $Li_6PS_5Br$ (0.87 mS/cm) and has a lower activation energy of 0.27 eV. The Li concentration of $BH_4$-substituted Li argyrodite is only slightly (1.5 %) lower than that of halogen-substituted argyrodites ($Li_6PS_5Cl$ and $Li_6PS_5Br$), which cannot be responsible for the ~5-fold increase of ionic conductivity.[129] This result strengthens our argument that pseudohalogen substitution indeed improves the ionic conductivity of argyrodite-like compounds.

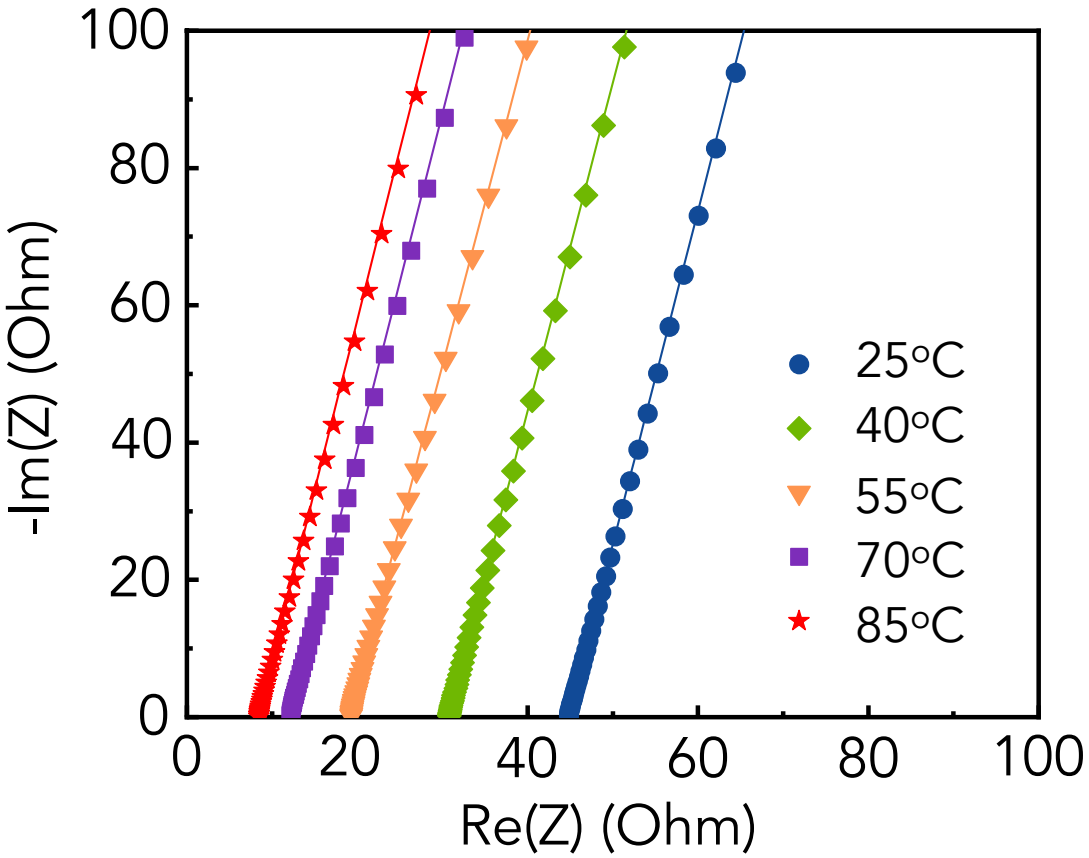


**Figure 2.7 EIS of $BH_4$-argyrodite at different temperatures.**
EIS plots of $Li_{5.91}PS_{4.91}(BH_4)_{1.09}$ at 25°C (blue circle), 40°C (green rhombus), 55°C (orange triangle), 70°C (purple square), and 85°C (red star).

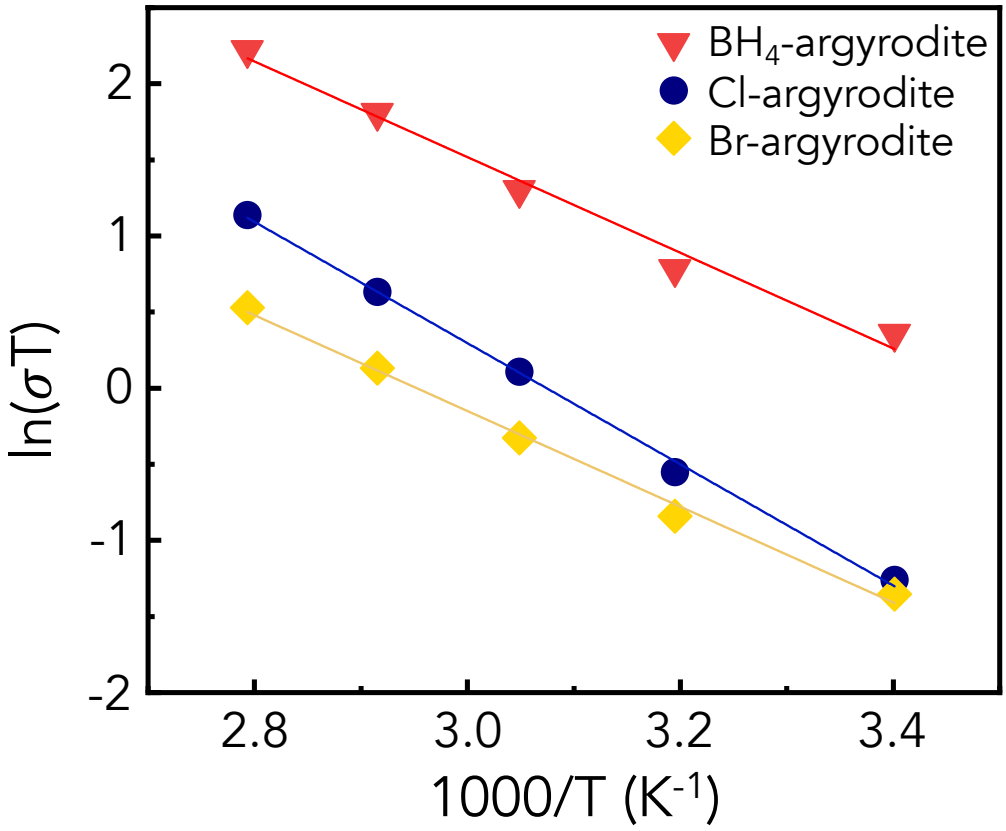


**Figure 2.8 Arrhenius plot of Li argyrodites.**
Arrhenius plot of $Li_{5.91}PS_{4.91}(BH_4)_{1.09}$ (red triangle), $Li_6PS_5Cl$ (blue sphere), and $Li_6PS_5Br$ (yellow rhombus).

To further evaluate the electrochemical performance of the $BH_4$-substituted Li argyrodite, a prototype all-solid-state cell was assembled with as-synthesized $Li_{5.91}PS_{4.91}(BH_4)_{1.09}$, an indium-metal anode, and a $LiNi_{0.5}Co_{0.2}Mn_{0.3}O_2$ cathode. On the cathode side, $LiNi_{0.5}Co_{0.2}Mn_{0.3}O_2$ was coated with lithium borate $Li_3B_{11}O_{18}$, which has been reported to protect the cathode from reaction with a sulfide electrolyte.[130] The cell was cycled between 1.4 and 3.7 V (2.0 and 4.3 V vs. $Li/Li^+$) at a current density of 0.05 $mA/cm^2$ under room temperature. The cell was held at 3.7 V for 3 hours after charging. The first-cycle capacity loss of ~60 mAh/g is likely attributable to the decomposition of the solid electrolyte. As is common in sulfides,[131] the excess charge capacity disappeared after the first cycle, indicating that a passivation layer may have formed at the interface between the electrolyte and carbon framework. A reversible capacity of ~130 mAh/g was obtained during the first two cycles (shown in Figure 2.9). However, the capacity of this all-solid-state

cell faded to 101 mAh/g after 10 cycles (as shown in Figure 2.9 and Supplemental Figure 2.3) which may be attributed to the fact that a $BH_4$ group can be easily oxidized at high voltage.

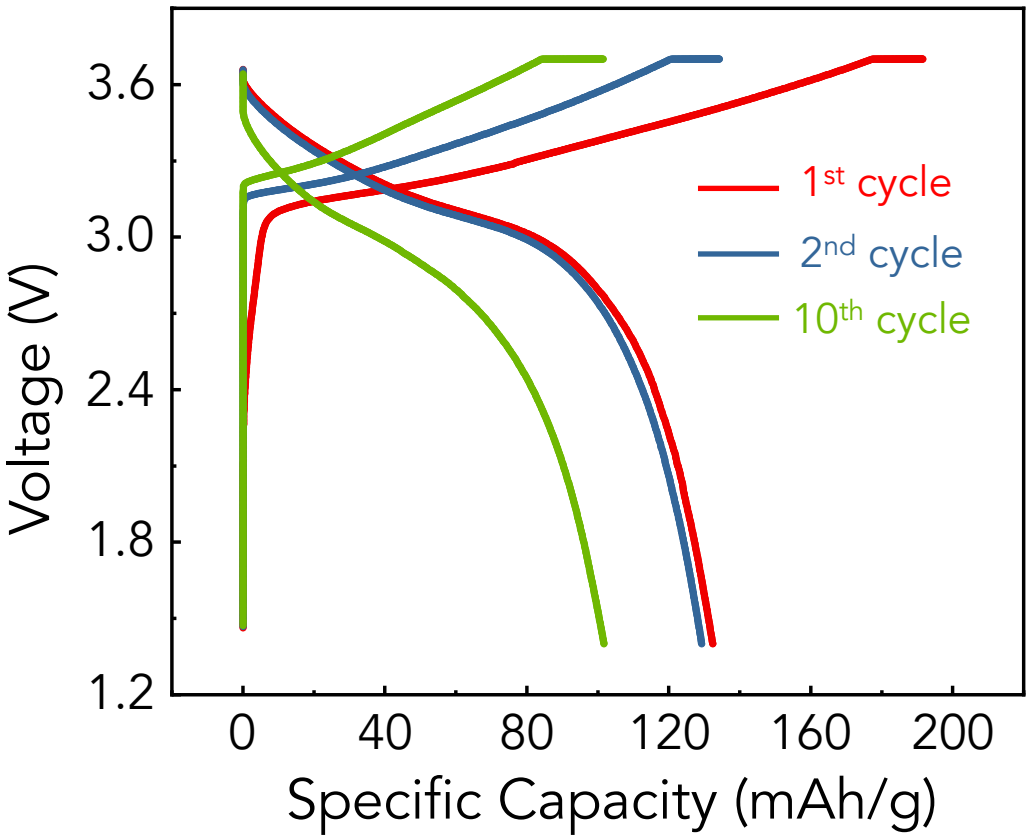


**Figure 2.9 Electrochemical performance of prototype ASSBs.**
(+) $LiNi_{0.5}Co_{0.2}Mn_{0.3}O_2$ | $Li_{5.91}PS_{4.91}(BH_4)_{1.09}$ | In (-) all-solid-state battery charged and discharged between 1.4 and 3.7 V at a current density of 0.05 mA/cm$^2$. The cell was held at 3.7 V for 3 hours after charging. See also Supplemental Figure 2.3.

## 2.5 Discussion

Ab-Initio Molecular Dynamics (AIMD) can be an effective approach to understand how different local structures contribute to the overall conductivity, as it can probe the correlation between local Li hopping and polyanion dynamics. The AIMD trajectory in a period of 10 ps at 600 K was selected to visualize the correlation between Li diffusion and polyanion groups. The atomic trajectories of selected Li with one of its first neighboring $BH_4$ groups and $PS_4$ groups are illustrated in Figure 2.10. Besides the Li migration observed in the trajectories, there is very significant

$BH_4$ motion, such that the $BH_4$ trajectory almost fills the spherical space around it as shown in Figure 2.10A. In contrast, because there is relatively less movement in the $PS_4$ group, its trajectory remains a tetrahedron shape, as observed in Figure 2.10B for the $PS_4$ group.

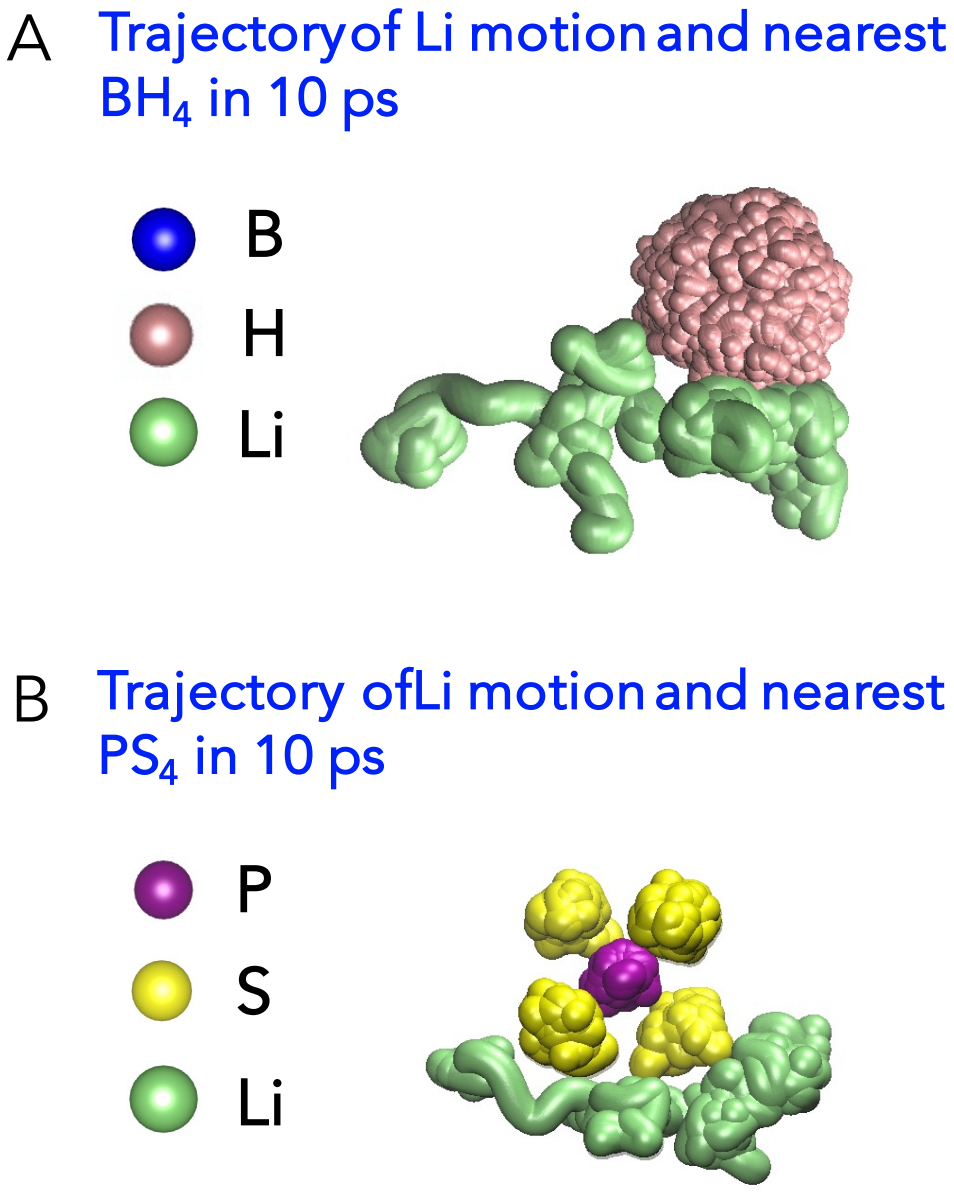


**Figure 2.10 Trajectories of atoms in $BH_4$-argyrodite.**
(A) Trajectories of one selected Li atom with its neighboring $BH_4$ (B is buried within the spherical trajectory of H) polyanion. (B) Trajectories of one selected Li atom with its neighboring $PS_4$ polyanion.

The structural dynamics of $BH_4^-$ and $PS_4^{3-}$ groups predicted by AIMD are consistent with Raman spectroscopy observations. Figure 2.5B shows that the $BH_4^-$ characteristic stretching modes in the $BH_4$ argyrodite sample are significantly broadened, in contrast to the sharp and well-resolved modes in the $LiBH_4$ lattice. This marked increase in the linewidth indicates significant damping and frequent scattering in the vibrational trajectories of the $BH_4^-$ group in $BH_4$-argyrodite, which supports the AIMD result. On the other hand, as shown in Figure 2.5A, the $PS_4^{3-}$ group characteristic mode at ~ 420cm$^{-1}$ largely maintains its narrow linewidth across the $\beta$-$Li_3PS_4$, Cl-argyrodite and $BH_4$-argyrodite. This behavior is consistent with the AIMD simulations showing well-defined small-amplitude vibrational motion of the $PS_4^{3-}$ group. These observations indicate that $BH_4$ is very flexible and free to move locally in contrast with $PS_4$. That suggests the possibility that $BH_4$ may easily relax away when Li moves, thereby facilitating its hopping.

Given that $BH_4$ and $PS_4$ behave quite differently in terms of vibrational motion, one may expect that the $BH_4$ motion will facilitate the diffusion of nearby Li. To investigate this possibility, we performed AIMD at 600 K for 10 ps and measured how long $Li^+$ stays close to a specific $BH_4^-$ or $PS_4^{3-}$ group once it has entered its environment. We define such an "interaction event" as occurring when $Li^+$ comes within a distance that is set as the maximum of the first neighbor bond length observed in the density functional theory (DFT) relaxed structure, which is 2.2 Å for Li–H and 2.8 Å for Li-S. We have also tested our analysis with the Li-H cutoff distance being 2.8 Å while fixing the Li-S cutoff to be 2.8 Å. As indicated in Supplemental Figure 2.4, the conclusion that Li is less anchored by H still remains. Figure 2.11A shows the "escape curve" for both environments. More specifically, what is shown is the fraction of $Li^+$ in an interaction event (y-axis) that has left again after a certain time (x-axis). It is clear that $Li^+$ leaves the $BH_4$ environment very quickly (black curve in Figure 2.11A) as compared to the $PS_4$ environment, where the $Li^+$ residence time is much longer (blue curves). A similar comparison is made between the Li–$BH_4$ residence time in $Li_6PS_5BH_4$ and the Li–Cl residence time in $Li_6PS_5Cl$ in Figure 2.11B. For $Li_6PS_5Cl$, the interact event radius was set as the maximum bond length of Li–Cl (2.8 Å).

As can be inferred from Figure 2.11A, $Li^+$ is much more strongly anchored near the $PS_4^{3-}$ group than near the $BH_4^-$ group. Almost all "interaction events" around $BH_4$ last less than 0.1 ps, whereas more than 40% of the events associated with the $PS_4$ group last longer than 0.1 ps. Moreover, ~10% of the $Li^+$ entering the $PS_4$ environment persist for longer than 1 ps, which is one-order-of-magnitude longer than the longest period of events around $BH_4$. It is also worth mentioning that such

event duration of ~0.1–1 ps is roughly the same time scale of Li hoping, as observed in the Li hopping analysis in Supplemental Figure 2.5.

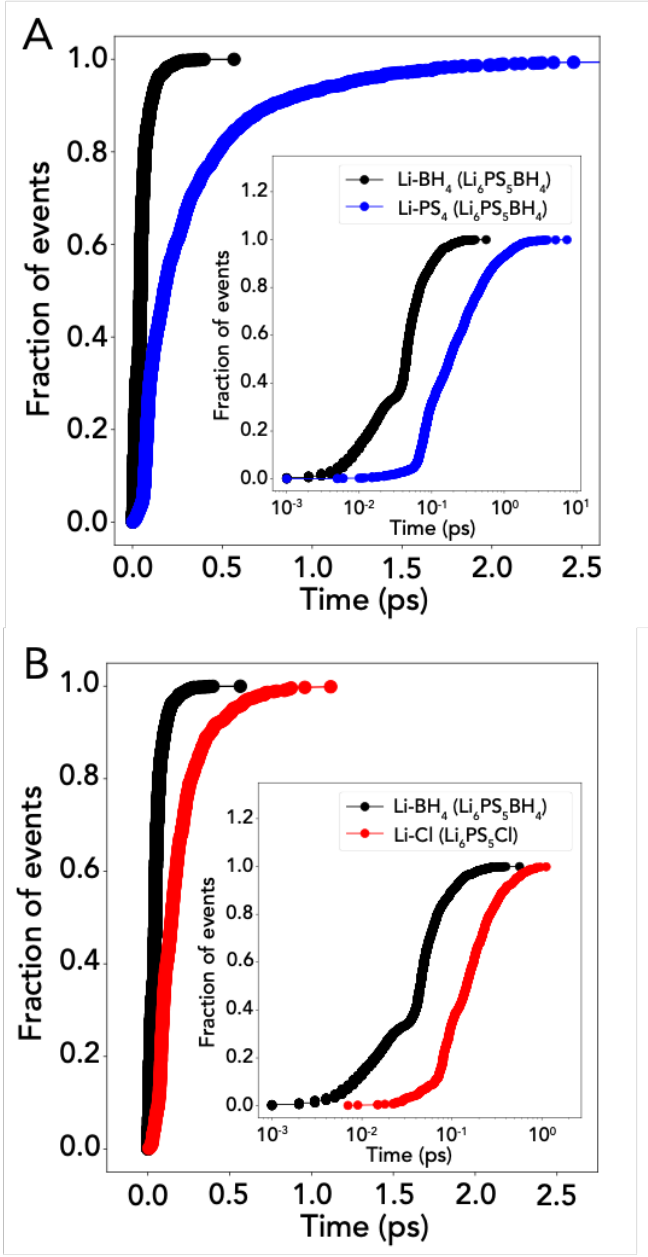


**Figure 2.11 Escape curves of Li in argyrodite structure.**
(A) Fraction of events occurring around $BH_4$ and $PS_4$ in $Li_6PS_5BH_4$ during a simulation time of 10 ps in 600 K (semilogarithmic plot in the set). See also Supplemental Figure 2.4. (B) Fraction of events occurring around $BH_4$ in $Li_6PS_5BH_4$ and Cl in $Li_6PS_5Cl$ during a simulation time of 10 ps in 600 K (semilogarithmic plot in the set). An event is defined as a Li atom entering a sphere of radius $r_{Li\text{-}H}$ = 2.2 Å, $r_{Li\text{-}Cl}$ = 2.8 Å or $r_{Li\text{-}S}$ = 2.8 Å.

Since the $PS_4$ group has a larger negative charge than $BH_4$ one may suspect that electrostatics plays a dominant role in the anchoring of Li near $PS_4$. But this is inconsistent with the data in Figure 2.11B which shows that even though Li–Cl "interaction events" in $Li_6PS_5Cl$ have short residence times (more than 90% of the lithium escapes from the Cl- environment occur in less than 0.25 ps), they are still substantially longer than the Li–$BH_4$ residence times, consistent with the increased ionic conductivity of $BH_4$-substituted argyrodite relative to that of $Li_6PS_5Cl$. It is also worth clarifying that the size of the $BH_4^-$ cluster ion is similar to that of $Cl^-$ because the Li–B bond lengths in $Li_6PS_5BH_4$ are similar to the Li–Cl bond lengths in $Li_6PS_5Cl$ (both range between 2.5 and 2.7 Å). Therefore, the enhancement of conductivity does not originate from the size difference between $BH_4^-$ and $Cl^-$.

Our ab-initio analysis clearly indicates that $BH_4^-$ anchors the Li ions much less than $PS_4^{3-}$ or $Cl^-$ in argyrodites. This weakened anchoring effect and consequently higher conductivity can have two possible origins: (1) a potential dynamic coupling between Li diffusion and $BH_4^-$ rigid rotation that facilitates Li conduction by lowering the activation barrier (also called the "Paddle-wheel" mechanism) and (2) a weaker interaction between Li–$BH_4$ that flattens the Li site energy landscape near $BH_4^-$, which facilitates the Li motion. Mechanism (1) has been frequently mentioned in recent papers as being responsible for fast Li conduction[110,111,120,122], whereas the role of mechanism (2) in contributing to the high conductivity has not been specifically evaluated. To determine whether both or one of these mechanisms contribute to the conductivity, we performed multiple analysis. In Figure 2.13 and Figure 2.14, we quantify the dynamic correlation of Li diffusion and multiple motion degrees of freedoms in $BH_4$ unit, whereas in Figure 2.15 we quantify the local electronic interaction among Li–$BH_4$, Li–$PS_4$, and Li–Cl.

In principle, the $BH_4$ cluster ion has 15 degrees of freedom, as each of the atoms can displace in three dimensions. To facilitate the analysis of a possible dynamic correlation, two key modes of motion of $BH_4$ are considered: the stretching mode and the bending mode. The translational mode of $BH_4$ as a unit is not considered here since the motions that we investigate are relative to the B atom which is also the center of mass of $BH_4$. The translational motion of $BH_4$ is captured in the motion of the Li atom relative to the B atom. As shown in Figure 2.12, the first mode represents the stretching of the B–H bond, whereas the second mode reflects the bending of the B–H bond, which can lead to the rotation of H relative to B.
To quantify whether $BH_4$ rotates as a rigid body we investigate the correlation between the angular changes of the B-H bonds which should be pronounced if the $BH_4$ cluster rotates as a rigid body. However, our dynamic correlation analysis

among the motion of the four B-H bond angles shows very little correlation (Pearson correlation analysis at Supplemental Table 2.2 and Supplemental Figure 2.8). Such observation indicates that the $BH_4$ unit does not rotate as a rigid body.

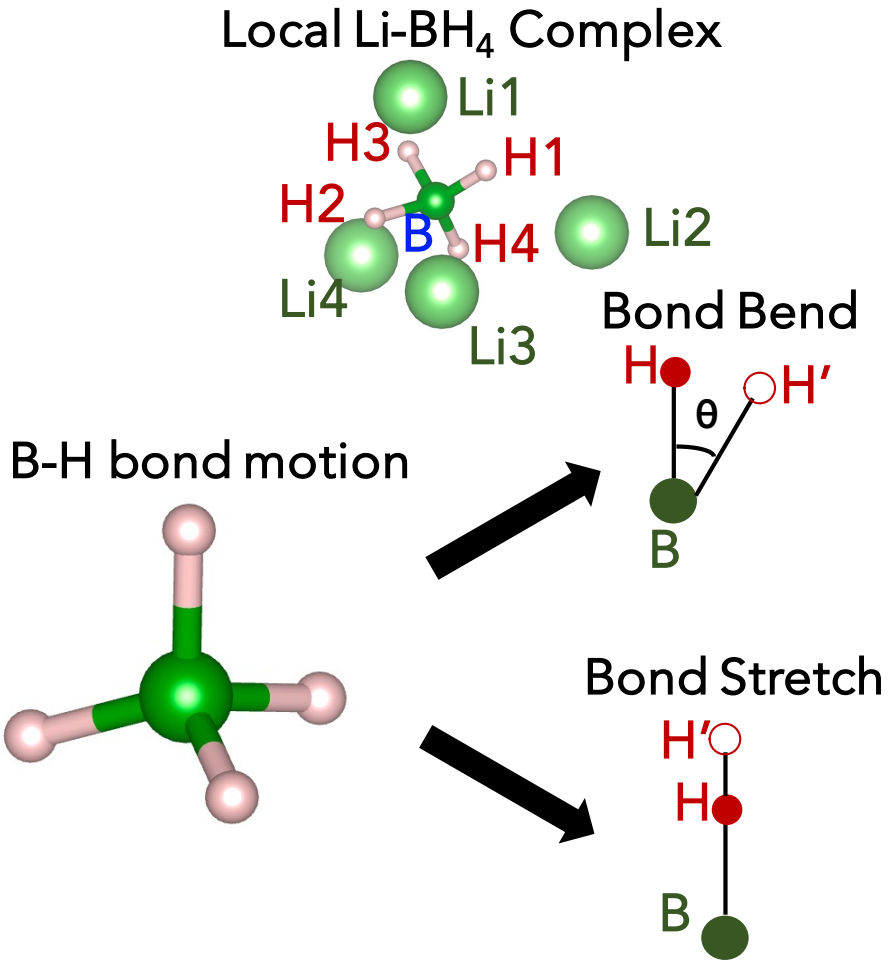


**Figure 2.12 Schematic illustration of Li diffusion and B-H bond motions.** Demonstration of the relationship between B-H bond motion and Li diffusion. The motion of B-H bond can be decomposed into stretching and bending modes of the B–H bond.

To quantify whether the Li motion is correlated with individual B-H bond motion, i.e., B-H bond stretching and B-H bond bending, the correlation between the B–H bond motion and Li position was calculated based on event analysis similar to the one used to generate Figure 2.11. We collect all the partial trajectories for which Li stays in a sphere within a cutoff distance of 3.0 Å from the B atom as events to investigate possible correlation between Li motion and B-H bond motion. If the Li motion is correlated to B–H bond motion, it should show up in the Pearson

correlation of trajectories. In atomic trajectories of 10 ps of AIMD simulation at 600 K, we tracked all the "events" for which Li is close enough to a $BH_4$ unit. For each of the "events", we obtain a time series of the Li–B and B-H displacement. We can then calculate and average the Pearson correlation coefficient of these two displacements with either stretching or bending. Both the histogram and estimated kernel density of the probability distribution of the average correlation of all the Li atoms are shown in Figure 2.13.

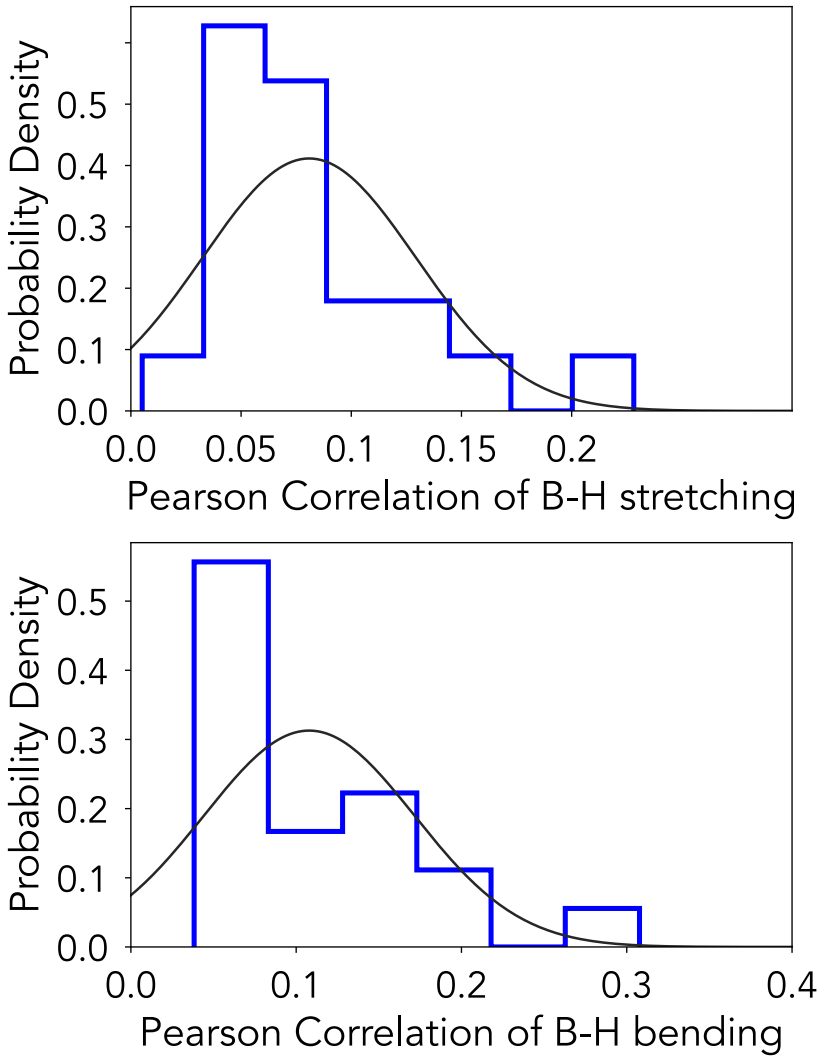


**Figure 2.13 Pearson Correlation between Li diffusion and B-H bond motions.** Probability distribution of the Pearson correlation between the stretching of the B-H bond and Li motion as well as the probability distribution of Pearson correlation between the bending of the B-H bond and Li motion.

For B-H bond stretching, we checked the correlation between changes in the B–H bond length and the Li–B distance. The Pearson coefficient[132] , in this case, is defined as (equation 2.1):

$$Corr = \frac{cov\left(l_{B-H}(t), l_{Li-B}(t)\right)}{\sigma\left(l_{B-H}(t)\right)\sigma\left(l_{Li-B}(t)\right)} \tag{2.1}$$

where $l_{B-H}(t)$ refers to the stretching length of the B–H bond, $l_{Li-B}(t)$ refers to the Li–B distance in the defined event, $cov(l_{B-H}(t), l_{Li-B}(t))$ refers to the covariance of Li-B distance and the stretching length of B-H bond while $\sigma(l_{B-H}(t))$ and $\sigma(l_{Li-B}(t))$ are the standard deviation of the Li-B distance and the stretching length of the B-H bond. For B-H bond bending, we evaluated the correlation between the B-H bending angle $\sigma(\theta_{B-H}(t))$ and the Li-B bending angle $\sigma(\theta_{Li-B}(t))$. We use Li–B bending angle as an indication of the motion of Li with respect to the corresponding B-H bond because the displacement of the Li atom itself does not give the relative position information of Li with respect to the B-H bond. The intercorrelation between these two bending angles can then be quantified using the Pearson correlation coefficient (equation 2.2):

$$Corr = \frac{cov\left(\theta_{B-H}(t), \theta_{Li-B}(t)\right)}{\sigma\left(\theta_{B-H}(t)\right)\sigma\left(\theta_{Li-B}(t)\right)} \tag{2.2}$$

In equation 2.2, $cov(\theta_{B-H}(t), \theta_{Li-B}(t))$ refers to the covariance of two bending angles while $\sigma(\theta_{B-H}(t))$ and $\sigma(\theta_{Li-B}(t))$ are the standard deviation of the bending angles.

It can be clearly inferred from Figure 2.13 that neither the B–H bond stretching, nor the bond bending are particularly correlated to the motion of Li atoms nearby. The maximum correlation coefficient observed is less than 0.2, and most of the coefficients are smaller than 0.1. Given that a correlation smaller than 0.5 is generally regarded as weak correlation in statistics,[133,134] the calculated value indicates that even though B-H bond bends and stretches very fast, the position of Li is not correlated to the movement of B-H bonds. Considering that rigid rotation of the $BH_4$ unit is absent, and the movement of in visual B-H bond shows little correlation with Li diffusion, there is no evidence to conclude that the enhanced conductivity in this material originates from a “paddle-wheel” mechanism.

To further corroborate the origin of weak correlation between $BH_4$ motion and Li diffusion, we calculated the frequencies of the stretching and bending degrees of

freedom for the B-H bond, as shown in Figure 2.14. For stretching degree of freedom, the frequency can be estimated as (equation 2.3):

$$f_{stretching} = \frac{1}{l_{max}} \times \frac{d(l_{B-H})}{dt} \tag{2.3}$$

Here, $l_{max}$ refers to the maximum amplitude of bond stretching as observed in the period of 10 ps. For bending degree of freedom, the frequency can be estimated as (equation 2.4):

$$f_{bending} = \frac{1}{360^0} \times \frac{d(\theta_{B-H})}{dt} \tag{2.4}$$

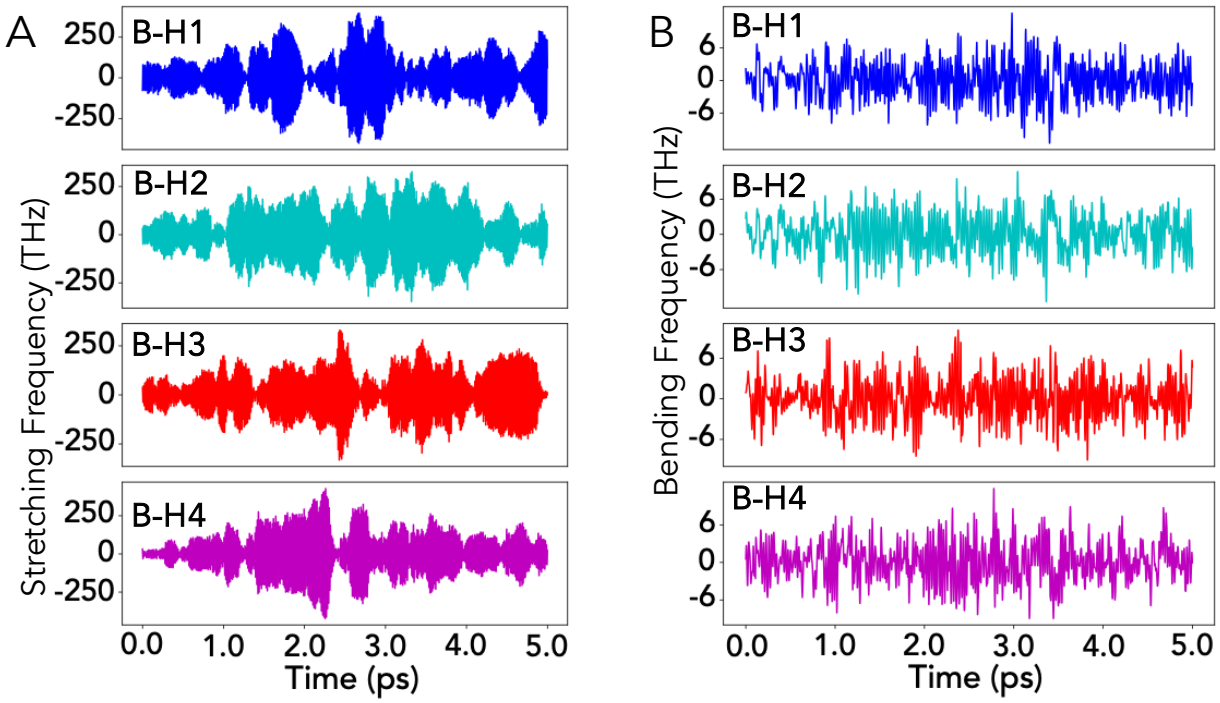


**Figure 2.14 Frequency evolution of the B-H bond stretching and bending.** Demonstration of the calculated frequency evolution of the B-H bond (A) stretching degree of freedom and (B) bending degree of freedom as a function of time for selected $BH_4$ unit as shown in Figure 2.12. See also Supplemental Figure 2.6.

The evolution of frequencies of stretching and bending degrees of freedom are demonstrated in Figure 2.14A and Figure 2.14B. Since the frequency at each time frame is calculated from the first derivative of the velocities, the overall analysis will not significantly be modified by longer trajectories. We have also confirmed this by plotting the frequency evolution over the shorter time of 1 ps (Supplemental Figure

2.6). As indicated in Figure 2.14A, the stretching frequency has a magnitude ranging from a few tens of THz to 200 THz, while the bending frequency in Figure 2.14B has a magnitude of several THz, which is consistent with observations on $BH_4$ groups in $Mg(BH)_4$.[135] Given that the Li hopping frequency is calculated to be well below 1 THz (Supplemental Figure 2.5), it turns out that both B–H bond stretching, and bond bending occur at a higher-frequency time frame than the Li hops, so that B-H bond motion and Li motion can be decoupled.

Finally, To verify whether the weaker anchoring effect of $BH_4^-$ on $Li^+$ is related to weak electronic interaction between $Li^+$ and $BH_4^-$, we calculated the integrated crystal orbital Hamilton population (-ICOHP) to quantify the chemical bonding strength of Li–$BH_4$, Li–$PS_4$, and Li–Cl (Figure 2.15).[136,137] As shown in Figure 2.15, the -ICOHP value of the Li–$BH_4$ bond is much smaller than that of the Li–$PS_4$ bond or Li–Cl bond, which reveals significantly weaker electronic interaction. Therefore, we confirmed that the enhanced ionic conductivity has little to do with dynamic correlation among Li diffusion and B-H bond motion (e.g., the "paddle-wheel" mechanism) but is mostly caused by weak electronic interaction between the $Li^+$ and $BH_4^-$ group. It should also be noted that the influence of weak electronic interaction between Li and the anion framework on Li ionic conduction has also been discussed in the context of the inductive effect that central ions in $MS_4$ tetrahedra have on the Li conduction in LGPS-like structures.[138]

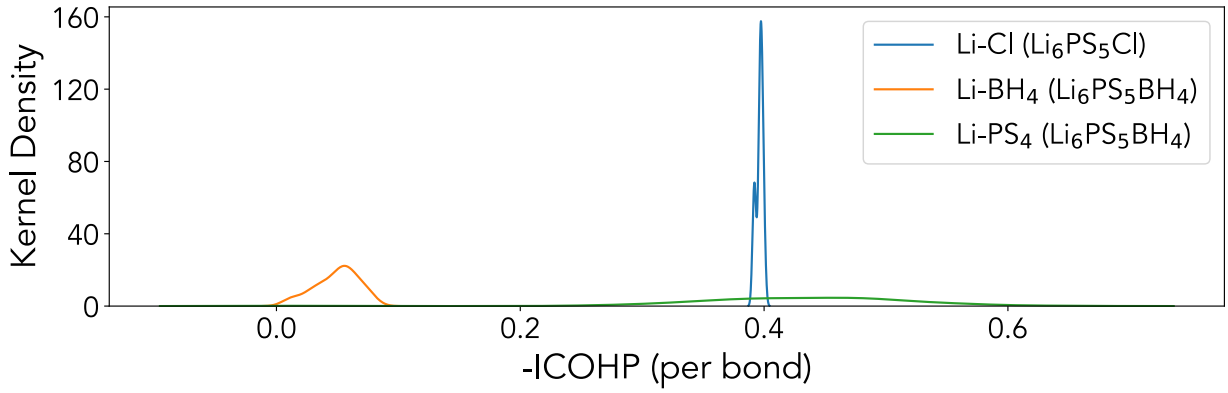


**Figure 2.15 Kernel density distribution of calculation -ICOHP value of Li–Cl, Li–$BH_4$, and Li–$PS_4$ bonding in $Li_6PS_5Cl$ and $Li_6PS_5BH_4$**

## 2.6 Conclusion

In this work, we investigated the Li argyrodite system to explore the possibility of enhancing ionic conductivity through pseudohalogen substitution. Ab-initio

computational screening to predict the synthetic accessibility of Li argyrodites with different pseudohalogen substitution suggested that among many possible polyanions, $BH_4$ could most likely substitute for the S on 4a and 4c sites in the argyrodite structure. This $BH_4$-substituted Li argyrodites ($Li_{5.91}PS_{4.91}(BH_4)_{1.09}$) was successfully synthesized via a mechanochemical method and shows an ionic conductivity of 4.8 mS/cm, ~5-times higher than that of common halogen-substituted Li argyrodites ($Li_6PS_5Cl$ and $Li_6PS_5Br$), confirming the positive contribution of a cluster ion to the Li-ion conductivity. AIMD analysis demonstrates that the enhancement of the Li-ion conductivity originates from the weaker anchoring effect the pseudohalide anion has on $Li^+$. We found no evidence for any correlation between B-H bond motion and Li motion, indicating that no "paddle-wheel" effect is needed to explain the enhanced conductivity.

## 2.7 Methodology

### 2.7.1 Synthesis

β-$Li_3PS_4$ was synthesized using lithium sulfide ($Li_2S$, Sigma-Aldrich, 99.98% trace metals basis) and phosphor sulfide ($P_2S_5$, Sigma-Aldrich, 99%) mixed in a 2:1 molar ratio (excess $P_2S_5$ was used) in acetonitrile (Sigma-Aldrich, anhydrous, 99.8%). The suspension was stirred for 24 h and filtered to obtain the precipitate. The precipitate was washed with acetonitrile (ACN) 3 times and dried at 80 °C for 12 h to obtain $Li_3PS_4$·2ACN. The as-obtained $Li_3PS_4$·2ACN was then heated under vacuum at 150 °C for 24 h to obtain β-$Li_3PS_4$. The as-synthesized β-$Li_3PS_4$ and $LiBH_4$ (Aldrich, >95%) were mixed in a 1:2 molar ratio and hand ground in an agate mortar for 15 min. Then, 0.8 g of the powder mixture and 80 g of zirconium oxide balls (5 mm in diameter) were placed into a zirconium oxide ball-mill jar and ball milled (SpexSamplePrep 8000M) for 2 h. To prevent the sample temperature from becoming too high, ball milling was paused for 15-min after every 30-min milling. The mixture was further annealed at 150 °C for 48 h to obtain $BH_4$-substitutued argyrodite. Because of the sensitivity to $O_2$ and moisture for the system, all the experimental procedures were performed in an argon atmosphere with <0.1 ppm of $O_2$ and $H_2O$.

$Li_6PS_5X$ (X = Cl, Br) samples were synthesized via a previously reported method.[96] Lithium sulfide ($Li_2S$, Sigma-Aldrich, 99.98% trace metals basis), phosphor sulfide ($P_2S_5$, Sigma-Aldrich, 99%), LiCl (Sigma-Aldrich, >99.98% trace metals basis), and LiBr (Sigma-Aldrich, >99%) were mixed in the appropriate stoichiometric ratio. The

mixtures were hand ground in an agate mortar for 15 min and then pressed into pellets of 6.0 mm in diameter under a pressure of 2.0 metric tons for 4 min. The pellets were then filled into quartz ampules (12-mm inner diameter and ~15 cm in length), which were sealed under vacuum. The ampules were carbon-coated and preheated to avoid traces of water. The reaction was performed at 550 °C for 144 h to obtain $Li_6PS_5X$ (X = Cl, Br).

Cl-substituted argyrodite and Br-substituted argyrodite were also prepared by the same synthesis approach as was used for the $BH_4$-substituted argyrodite. β-$Li_3PS_4$ and LiX (X = Cl, Br) were mixed in a 1:2 molar ratio and hand ground in an agate mortar for 15 min. Then, 0.8 g of the powder mixture and 80 g of zirconium oxide balls (5 mm in diameter) were placed into a zirconium oxide ball-mill jar and ball milled (SpexSamplePrep 8000M) for 2 h. Ball milling was paused for 15-min after every 30-min milling. The mixture was further annealed at 150 °C for 48 h to obtain Cl-substituted argyrodite and Br-substituted argyrodite. The EIS of these halide-substituted argyrodites are shown in Supplemental Figure 2.7.

## 2.7.2 Electrochemistry

The Li-ion conductivity was evaluated using EIS with tantalum metal as blocking electrodes at temperatures ranging from 20 °C to 85 °C. The solid-electrolyte powder was uniaxially compressed under a pressure of 520 MPa to make a ~1-mm-thick pellet with a diameter of 7.7 mm and then sandwiched by two tantalum foils. EIS measurements were performed using an EC-Lab Electrochemistry SP300 system (Biologic). The measurements were conducted at the initial open-circuit voltage in the frequency range of 7 MHz to 10 mHz with the application of a 10-mV signal amplitude. The measurements were performed using a Biologic controlled environment sample holder assembled and sealed in an Ar-filled glove box.

Solid-state cells were also fabricated in an Ar-filled glovebox. The cathode composite was prepared by first hand-mixing 65 mg of LBO-coated $LiNi_{0.5}Co_{0.2}Mn_{0.3}O_2$ powder (from Samsung Research Japan[130]) and 30 mg of $Li_{5.91}PS_{4.91}(BH_4)_{1.09}$ for 20 min and then mixing them for another 20 min after adding 5 mg of carbon nano-fibers (CNFs, from Samsung Research Japan). The cell was assembled using a custom-made pressure cell consisting of a polyether ketone (PEEK) cylinder with an inner diameter of 8 mm and two 8-mm-diameter stainless-steel rods as current collectors. One end of the cylinder was first closed with a current collector. Then, 40 mg $Li_{5.91}PS_{4.91}(BH_4)_{1.09}$ as the electrolyte was added and

compressed under a pressure of 100 MPa. Then, 5 mg of the cathode composite was spread evenly on top of the electrolyte membrane and compacted under pressure of 200 MPa. Finally, an 8-mm-diameter piece of In metal was attached on the other side of the electrolyte membrane as the anode and compacted under 200-MPa pressure again. The entire cell was sealed in an Ar-filled jar and cycled under 5-MPa stack pressure provided by a spring. Cell cycling was performed using a Bio-Logic VMP300 system.

### 2.7.3 Characterization

For structure determination, synchrotron XRD data were collected at beamline 11BM at the Advanced Photon Source at Argonne National Laboratory. Because of the air sensitivity of the sample, the $Li_{5.91}PS_{4.91}(BH_4)_{1.09}$ powder was sealed into 0.0395-inch-diameter polyimide tubing in an argon glove box. Rietveld refinement was performed using the TOPAS V6 software package (Bruker). Chebyshev polynomials are used for the background fitting. Fundamental parameters approach is used for the peak shape modeling. The constrains for the structural factor refinement are as follows:

Occ(X) represents the site occupancy of atom X at related Wyckoff position.
4a sites are fully occupied by B1 and S1:
Occ(B1) + Occ(S1) = 1
4c sites are fully occupied by B2 and S2:
Occ(B2) + Occ(S2) = 1
H1 is bonded to B1 and H2 is bonded to B2:
Occ(B1) = Occ(H1), Occ(B2) = Occ(H2)
Based on the charge balance, we could get:
12Occ(Li1) + 6Occ(Li2) + Occ(B1) + Occ(B2) = 7.

TEM ED and EDS measurements were performed on a FEI TitanX 60-300 microscope equipped with the Bruker windowless EDS detector at an accelerating voltage of 300 KV in the Molecular Foundry at LBNL. The simulated electron diffraction ring pattern for argyrodite structure (ICDD 04-018-1429) was generated with the Single Crystal 4 diffraction simulation software. Raman spectroscopy measurements were carried out using a home-built confocal micro-spectroscopy setup. Briefly, a Coherent Verdi-V2 single frequency laser was used as the excitation source at a wavelength of 532nm. The excitation laser was focused onto the sample surface using a 60X NA0.7 Nikon ELWD objective. The same objective collected

the backscattered light. The collected signals were sent through 532nm notch filters to remove the Rayleigh line and then focused onto the entrance slit of a spectrometer. An IsoPlane 320 spectrometer equipped with an 1800 g/mm grating was used to disperse the signal onto a PIXIS 400 thermoelectrically cooled CCD. All samples were pellets pressed in an argon-filled glovebox and sealed using PET/PE encapsulations.

## 2.7.4 Computational methods

**DFT Structural Optimization and Total Energy Calculations:**

Because of the partial occupancy of Li sites in the argyrodite structure, structural enumerations in a supercell with only 48h Li sites were performed, and first-principle calculations were performed on the top 10 structures with lowest electrostatic energy using DFT as implemented in the plane-wave-basis-set Vienna ab initio simulation package (VASP). The structure with lowest DFT energy is then selected for further AIMD simulation. Projector augmented wave potentials with a kinetic energy cutoff of 520 eV were used in all the structural optimizations and total-energy calculations, and the exchange and correlation functionals were described within the Perdew−Burke−Ernzerhof generalized gradient approximation (GGA-PBE). The k-point grid in each dimension was set as 25 Å divided by the exact length of that dimension.

**Phase Stability Analysis:**

The thermodynamic stability was evaluated using the calculated DFT total energy. The stability of any phase was evaluated by comparing its energy to linear combinations of the energy of other phases (leading to the same composition) using the convex-hull construction. The stability analysis was performed versus all the compounds in our internal database, which includes both phases from the Inorganic Crystal Structure Database (ICSD) [Inorganic Crystal Structure Database; http://icsd.fiz-karlsruhe.de/icsd/] and some compounds generated from data-mined substitution rules.[139] The phase stability was quantified by evaluating the energy above the hull (ehull), which refers to the compound decomposition energy to materials at the hull. A non-negative value of the ehull energy indicates a thermodynamic driving force for decomposition into alternate phases. To correct the overestimation of the binding energy by the GGA-PBE functional, we followed

previous approaches[140,141] to apply constant energy corrections of −0.66 eV per S atom. On the basis of the DFT calculated charge density and wavefunction, we performed COHP analysis using the LOBSTER package.[136,137]

**Li-ion Diffusivity and Conductivity Calculations:**

AIMD simulation was used to investigate the ionic conductivity of Li ions. For all the AIMD calculations, an NVT ensemble was applied with a time step of 1 fs and a Nosé–Hoover thermostat[142] with a period of 100 fs. A minimal **Γ**-point-only grid was used with spin-polarized calculations. The AIMD simulations were run at 600 K, 700 K, 800 K, and 1000 K. All the data were fitted assuming Arrhenius behavior to obtain the activation energy, diffusion pre-factor, and room-temperature diffusivity. The lowest-energy atomic configurations were used as the initial configuration of the AIMD simulations.

## 2.8 Supporting Information

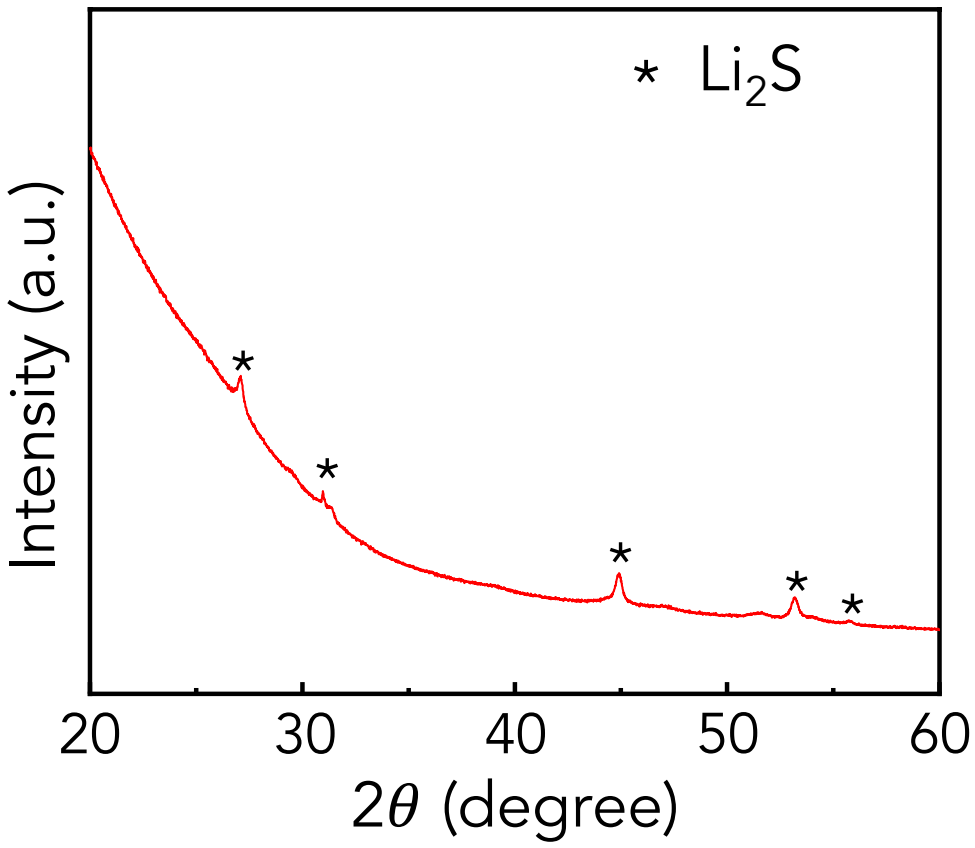


**Supplemental Figure 2.1 PXRD pattern of the synthesis product without excess $LiBH_4$.**

To prove the importance of excess $LiBH_4$, we tried synthesizing $Li_6PS_5BH_4$ with no excess $LiBH_4$. The precursors were mixed in the stoichiometric ratio ($\beta$-$Li_3PS_4$ : $LiBH_4$ : $Li_2S$ = 1: 1 : 1) and all other synthesis conditions are unchanged. Powder X-ray diffraction (PXRD) was conducted to analysis the synthesis product with no extra $LiBH_4$. Only the peaks of $Li_2S$ were found in PXRD results. No peak of argyrodite phase was found, indicating that $Li_6PS_5BH_4$ cannot be synthesized without excess $LiBH_4$.

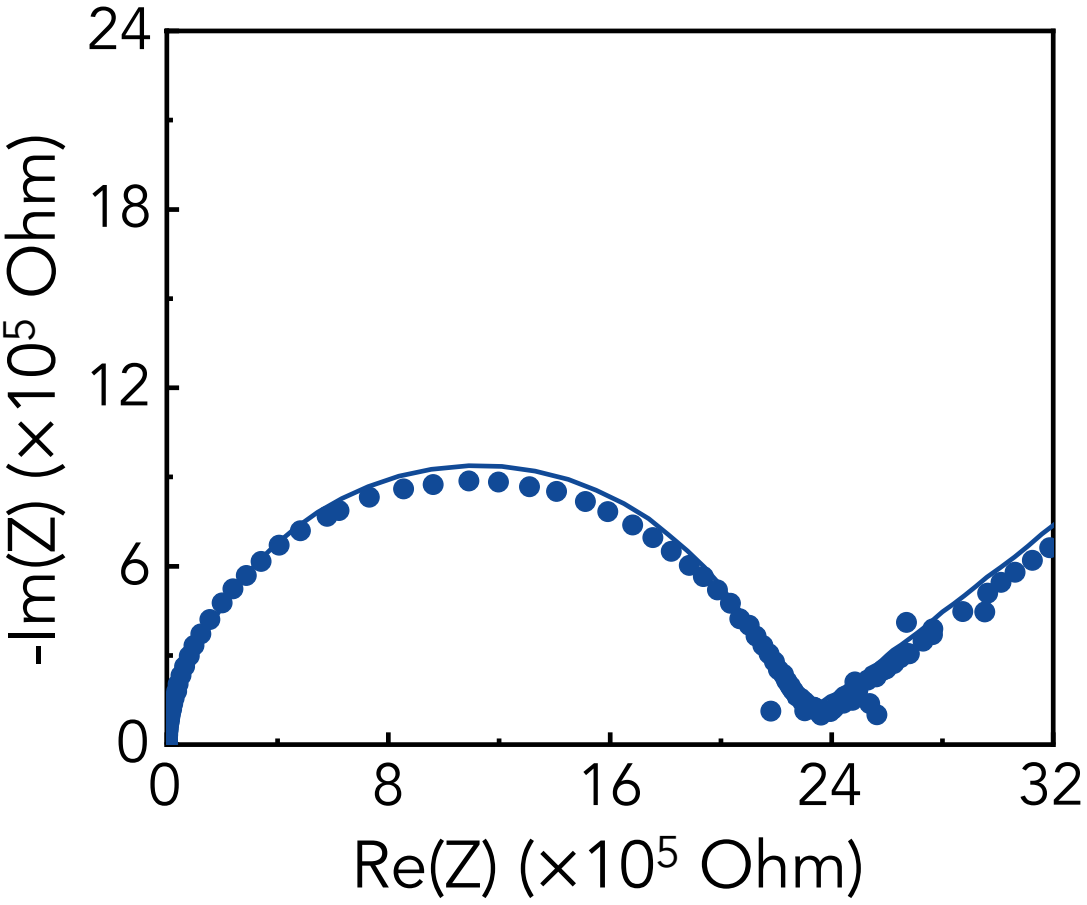


**Supplemental Figure 2.2 EIS plot of $LiBH_4$ at room temperature.**
The RT ionic conductivity of $LiBH_4$ is 9.72 x $10^{-5}$ mS/cm which is 5 orders lower than that of $Li_{5.91}PS_{4.91}(BH_4)_{1.09}$.

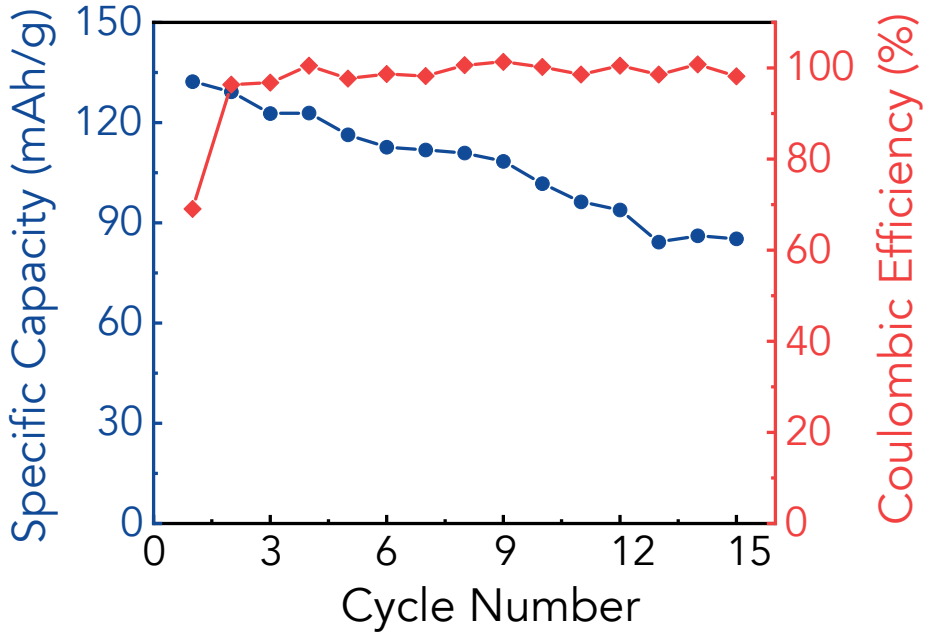


**Supplemental Figure 2.3 Specific capacity and Coulombic efficiency of(+) $LiNi_{0.5}Co_{0.2}Mn_{0.3}O_2$ | $Li_{5.91}PS_{4.91}(BH_4)_{1.09}$ | In (-) all-solid-state battery over 15 cycles.**
Related to Figure 2.9.

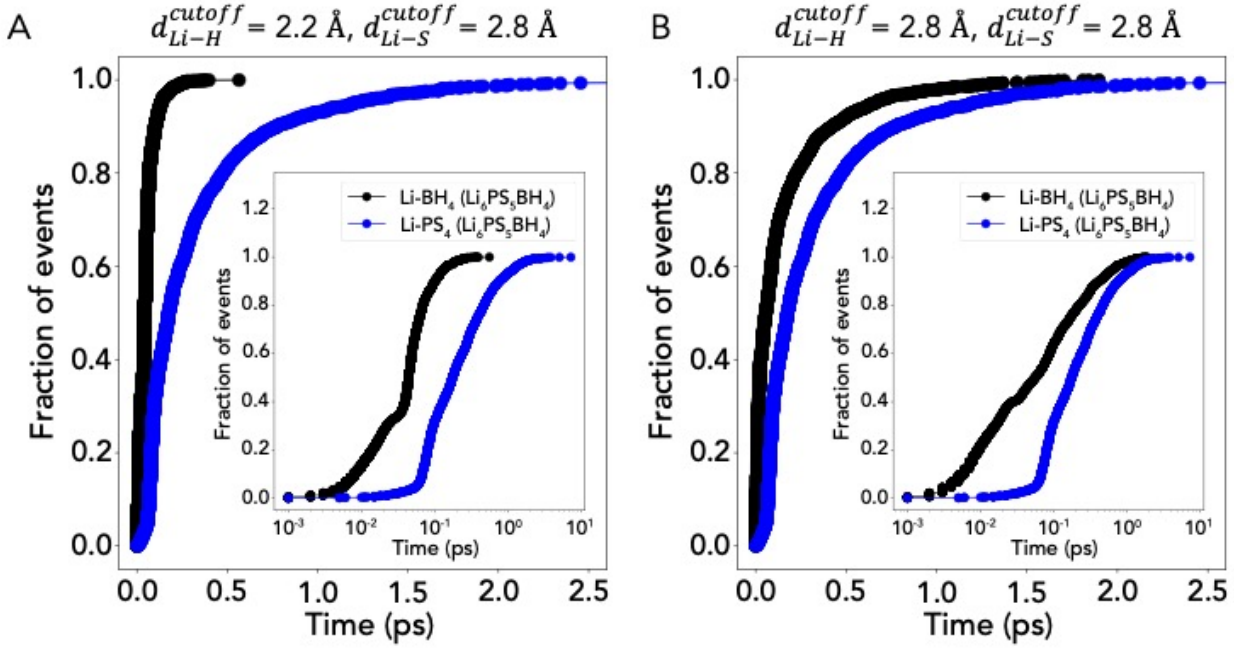


**Supplemental Figure 2.4 Comparison of event analysis at different Li-H cutoff distance.**
Related to Figure 4.

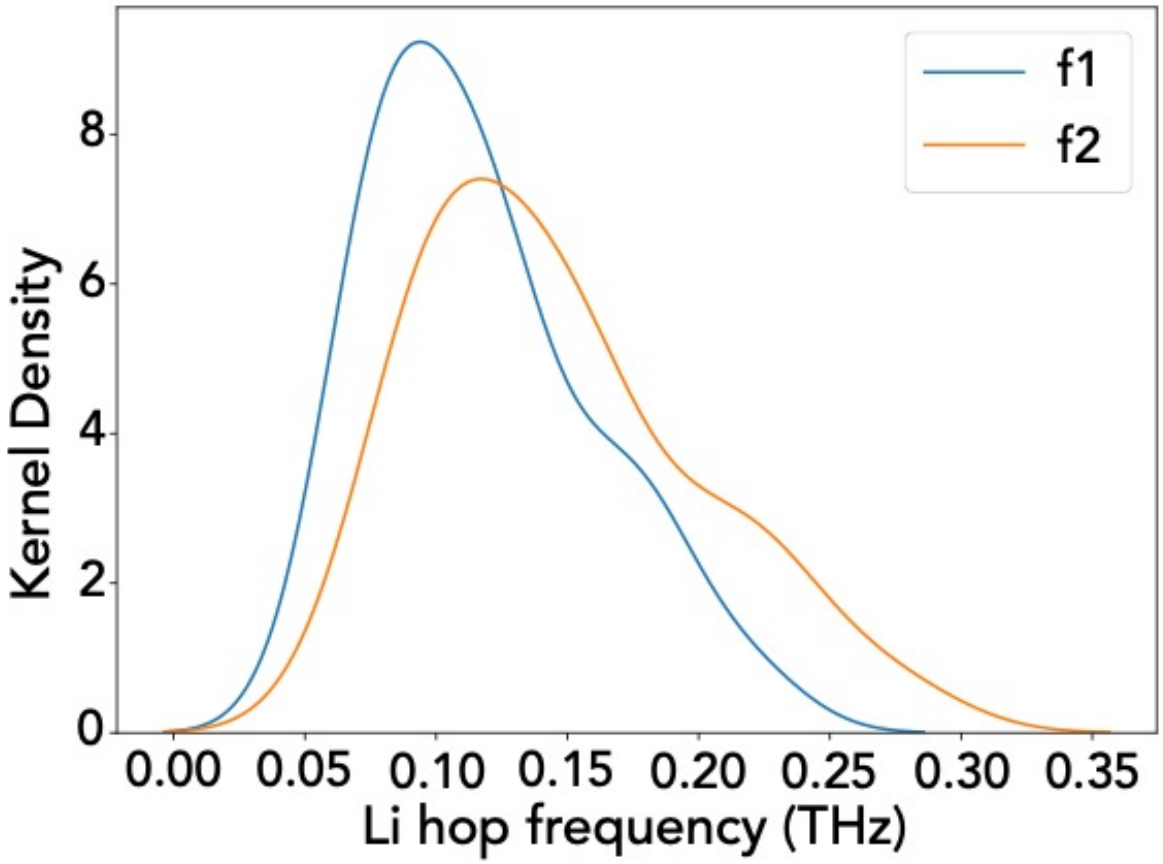


**Supplemental Figure 2.5 Calculated Li hopping frequency.**

We calculate the Li hopping frequency using $f = \frac{\mathrm{d}_{max}}{d_{cut}t}$, where $\mathrm{d}_{max}$ indicates the maximum displacement of Li within a time $t$, and $\mathrm{d}_{cut}$ indicates the Li hopping distance. We have plotted the kernel density with two different $\mathrm{d}_{cut}$ values, i.e., the distance between two 48h sites from the neighboring cage (shown as f1) or two 48h sites within the same cage (shown as f2). These two hopping mechanisms correspond to the so-called intra-cage jump and inter-cage jump in the previous paper[116]. It can clearly be seen that most Li ions have a hopping frequency of 0.05-0.2 THz, which is smaller than the stretching frequency and bending frequency of the B-H bond.

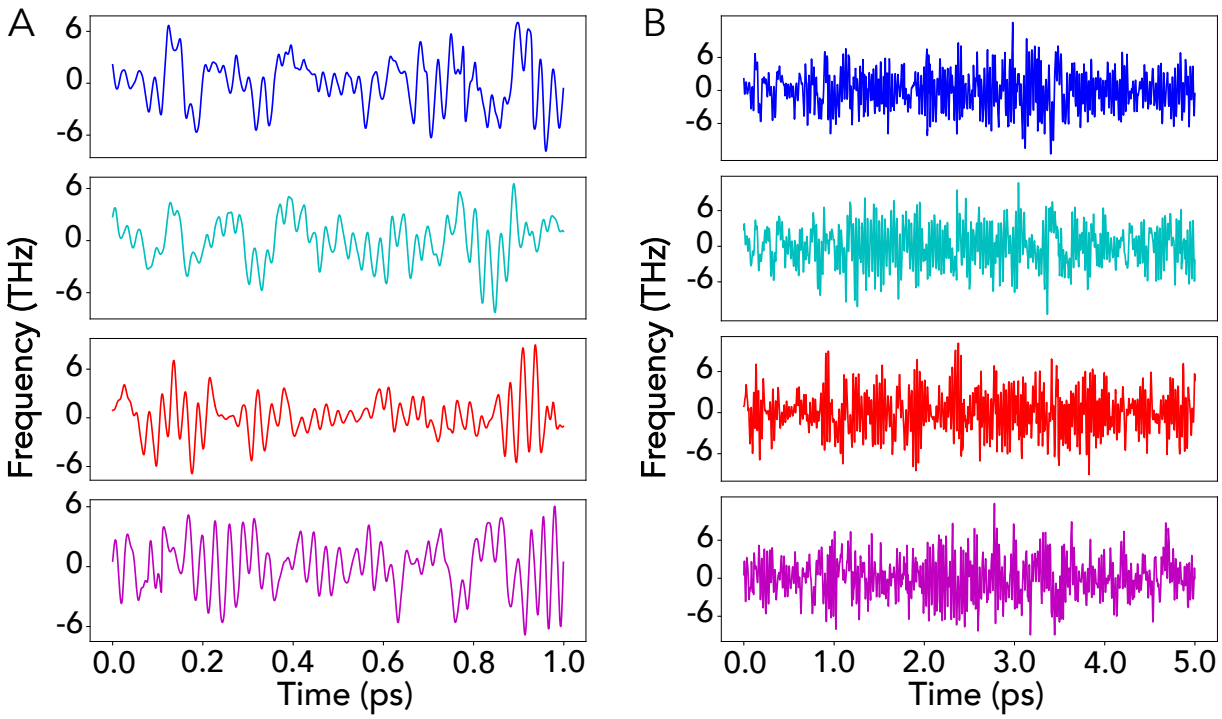


**Supplemental Figure 2.6 Computed bending frequency. as a function of time within the duration of (a) 1ps and (b) 5ps.**
Related to Figure 2.14.

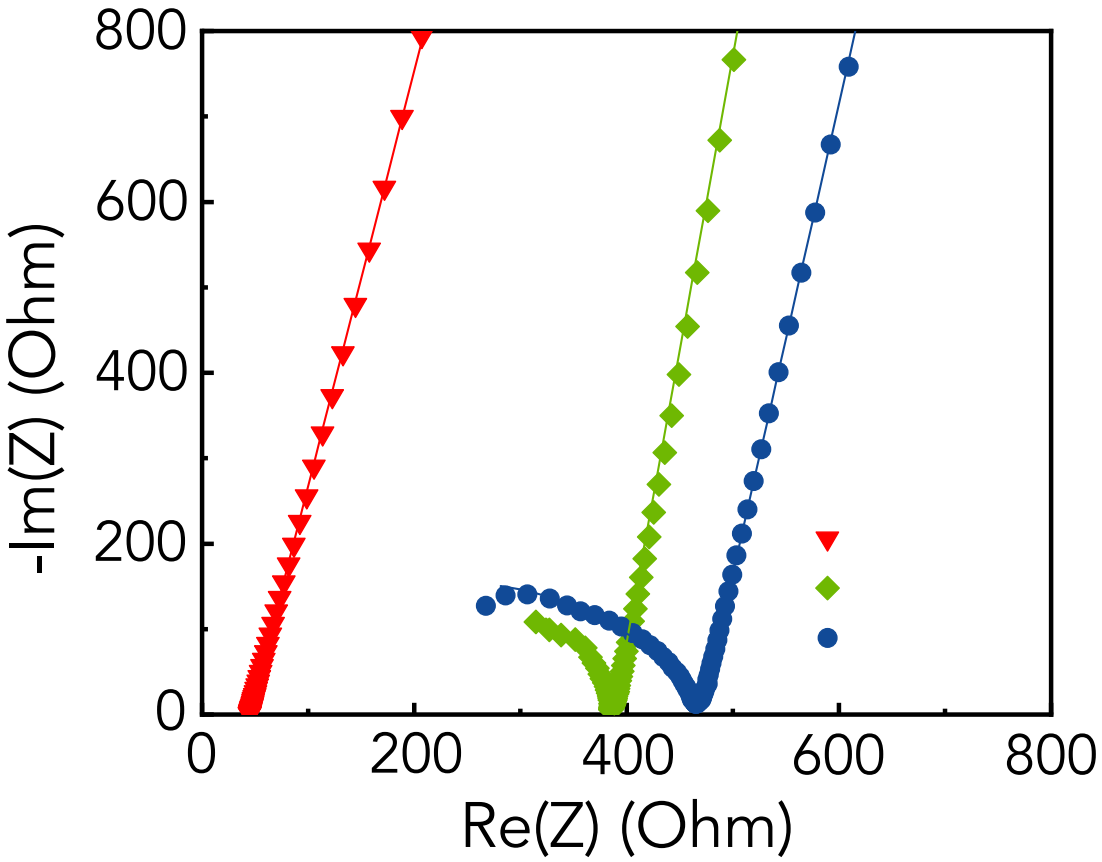


**Supplemental Figure 2.7 EIS of argyrodites prepared by the same synthesis approach.**

EIS plots of $BH_4$-argyrodite (LPSBH, red triangle), Cl-argyrodite (LPSCl, green rhombus), and Br-argyrodite (LPSBr, blue circle) all prepared by the same synthesis approach. The RT ionic conductivities of as-synthesized Cl-argyrodite and Br-argyrodite are 0.55 mS/cm and 0.46 mS/cm, which are even lower than the ionic conductivities of $Li_6PS_5Cl$ and $Li_6PS_5Br$ that we used as reference.

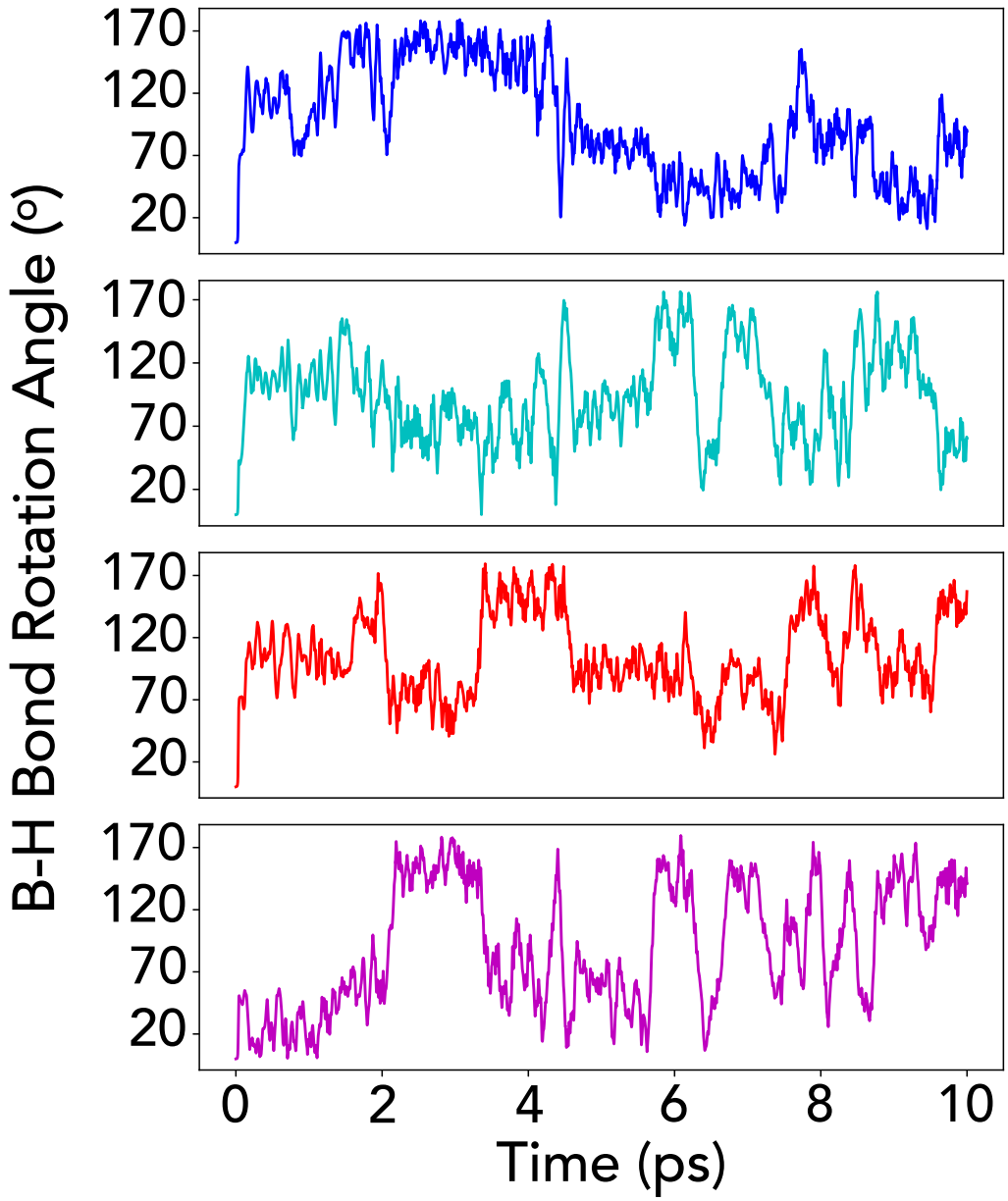


**Supplemental Figure 2.8 Computed rotation angle of B-H bonds as a function of time within the duration of 10 ps.**
Related to Supplemental Table 2.2.

**Supplemental Table 2.1 Energy differences by moving one Li from 48h site to 48h' site in cubic cell of $Li_6PS_5X$ (X = Cl, Br, I, $BH_4$). The super cell is 4 formula units of $Li_6PS_5X$ (X = Cl, Br, I, $BH_4$).**

| Formula | $Li_6PS_5Cl$ | $Li_6PS_5Br$ | $Li_6PS_5I$ | $Li_6PS_5BH_4$ |
|---|---|---|---|---|
| $E_{Diff}$ $(mev/atom)$ | 7.3 | 2.9 | -1.7 | 11.6 |

**Supplemental Table 2.2 Calculated Pearson's correlation of four B-H angles over a time frame of 5ps.**

| | B-H bond 1 | B-H bond 2 | B-H bond 3 | B-H bond 4 |
|---|---|---|---|---|
| B-H bond 1 | 1.0 | -0.29 | 0.27 | -0.07 |
| B-H bond 2 | -0.29 | 1.0 | -0.003 | 0.02 |
| B-H bond 3 | 0.27 | -0.003 | 1.0 | 0.09 |
| B-H bond 4 | -0.07 | 0.27 | 0.09 | 1.0 |

# Chapter 3 Explore oxide Li-ion superionic conductors with corner-sharing framework

## 3.1 Foreword

The work presented in this chapter was published in Jun, K., Sun, Y., Xiao, Y., Zeng, Y., Kim, R., Kim, H., Miara, L.J., Im, D., Wang, Y. and Ceder, G., 2022. Lithium superionic conductors with corner-sharing frameworks. *Nature Materials*, pp.1-8., and is reproduced here with the permission of co-authors.

## 3.2 Abstract

Superionic lithium conductivity has only been discovered in a few classes of materials, mostly found in thiophosphates and rarely in oxides. Herein, we reveal that corner-sharing connectivity of the oxide crystal structure framework promotes superionic conductivity, which we rationalize from the distorted lithium environment and reduced interaction between lithium and non-lithium cations. By performing a high-throughput search for materials with this feature, we discover ten new oxide frameworks predicted to exhibit superionic conductivity—from which we experimentally demonstrate $LiGa(SeO_3)_2$ with a bulk ionic conductivity of 0.11 mS $cm^{-1}$ and an activation energy of 0.17 eV. Our findings provide insight into the factors that govern fast lithium mobility in oxide materials and will accelerate the development of new oxide electrolytes for all-solid-state batteries.

## 3.3 Introduction

All-solid-state batteries are increasingly attracting attention as next-generation energy storage devices for application in consumer electronics and electric vehicles[143]. The all-solid-state design replaces the flammable organic liquid electrolyte in conventional batteries with an inorganic solid electrolyte (SE) and enables the use of high-energy electrodes, resulting in enhanced safety and high energy density[144]. A critical factor for the realization of such batteries is the development of SEs with high ionic conductivity and excellent electrochemical stability against both a lithium metal anode and high-voltage cathodes[72]. While high ionic conductivity obviously reduces cell impedance and may increase the

active materials loading in the cathode composite[145], it has recently also been shown to reduce the build-up of mechanical stress in the lithium metal anode[146].

Several sulfide-based inorganic SEs, such as $Li_{10}GeP_2S_{12}$ (LGPS)[27], $L_7P_3S_{11}$[147] and lithium argyrodites[112] exhibit high lithium ionic conductivity (>10 mS $cm^{-1}$) exceeding that of liquid electrolytes[44]. However, the limited chemical and electrochemical stability of the sulfides[86,88,148,149] and their possible $H_2S$ release upon air or water exposure[150,151] are potential safety concerns for both manufacturing and applications. In contrast, many oxide SEs have shown excellent air and electrochemical stability[86], but their ionic conductivities are generally lower than those of sulfide SEs[152]. Thus far, only a few oxide SEs (for example, Na superionic conductor (NASICON)-type lithium oxides[65], lithium garnets[45] and lithium perovskites[153]) have been discovered with room-temperature (RT) ionic conductivities ($\sigma_{RT}$) of the order of 0.1–1 mS $cm^{-1}$.

The discovery of new fast lithium-ion conductors could be accelerated if the structural and chemical features that govern facile lithium movement could be identified. In sulfides, finding superionic conductors has focused on crystal structures that provide a low-barrier ionic pathway between nearly energy-equivalent sites.[73] This has led to the principle that materials with a body-centred-cubic (bcc) arrangement of anions are more desirable than close-packed structures, as this bcc arrangement allows for lithium migration through face-sharing tetrahedral sites with low activation energy. This feature has been observed in the best-performing sulfide ionic conductors such as $L_7P_3S_{11}$, LGPS and its derivatives, and was used in the design of a new class of SE, $Li_{1+2x}Zn_{1-x}PS_4$.[60,154]

The guidelines for finding good sulfide lithium-ion conductors do not seem as applicable to oxide materials. The hypothetical oxide derivative of LGPS, $Li_{10}GeP_2O_{12}$, is predicted to exhibit ionic conductivity that is two orders of magnitude lower than that of LGPS[124] and has never been synthesized. Similar observations of lower ionic conductivity in oxides than sulfides have been made for Li superionic conductors (LISICON) versus thio-LISICON conductors.[71] The lower ionic conductivity of oxides is primarily attributed to the weaker screening ability of the oxygen anion relative to that of the sulfur anion, and this difference in screening power probably gives the arrangement of the non-lithium cations a larger influence on the lithium mobility in oxides than it does in sulfides.[145,155] While it is the near-sightedness of the cation electrostatics in sulfides that leads to the focus on the anion coordination for conductivity optimization, oxides require a different conceptual framework as the oxygen anion cannot effectively screen away the interaction with the other cations. The lack of design principles for superionic

conductors has led to a much lower success rate in finding new oxide conductors in computational screening efforts than has been the case for sulfides[156–161].

In this work, we identify a corner-sharing (CS) framework as a structural feature common to many oxide superionic conductors. By using this feature as a descriptor in high-throughput computational screening, we identify ten new oxide structural frameworks that are predicted to exhibit superionic conductivity. The concept is experimentally validated in $LiGa(SeO_3)_2$, a new oxide conductor that shows a very high bulk ionic conductivity of 0.11 mS cm$^{-1}$. Our findings suggest that corner sharing in the framework provides access to a highly distorted lithium environment and allows for percolating pathways through which lithium can move with a low energy barrier, thereby explaining the origin of the fast lithium diffusion in multiple known and predicted oxide superionic conductors.

## 3.4 Results

### 3.4.1 A structural commonality of lithium superionic conductors

A typical inorganic lithium-ion conductor has a crystal structure with anions serving as a backbone hosting fast-moving lithium and immobile non-lithium cations. Figure 3.1 presents the structures of three exemplary fast lithium-ion conductors with their non-lithium cation sites visualized as coloured polyhedrons. $Li_{1+x}Al_xTi_{2-x}(PO_4)_3$ represents a NASICON-type superionic conductor with an experimental $\sigma_{RT}$ of approximately 3 mS cm$^{-1}$ at $x = 0.3$.[65,162] $LiTa_2PO_8$ is a superionic conductor with ionic conductivity of 1.6 mS cm$^{-1}$ at RT.[163] $Li_{1+x}Ta_{1-x}Zr_xSiO_5$ has been predicted to be a fast ionic conductor and was successfully synthesized recently.[164,165] With sufficient excess lithium, its ionic conductivity is predicted to reach 6.1 mS cm$^{-1}$ at RT.

We argue here that these fast oxide conductors, in addition to ten other groups of oxide conductors that were previously predicted to be fast conductors (Supplemental Table 3.1), have important structural commonality and that this insight can be leveraged to find other fast ionic conductors. The non-lithium cation polyhedrons in these structures are interconnected by a corner-shared oxygen, and never share any common edges (O–O bond) or faces (O–O–O triangle), as shown in Figure 3.1D-E. For example, the framework of $Li_{1+x}Al_xTi_{2-x}(PO_4)_3$ consists of corner-shared Ti octahedrons and P tetrahedrons. To extract this structural feature in a rigorous manner, we first define the ‘framework’ of a compound as the set of coordination polyhedrons of immobile cations excluding lithium. A CS framework is defined as

a framework in which its polyhedrons are interconnected solely by one anion vertex or less (Figure 3.1F-G). Using this definition of a CS framework, we also include frameworks in which polyhedrons are isolated from one another (for example, the framework of LGPS or LISICON $Li_{2+2x}Zn_{1-x}SiO_4$ with $x > 0$[166,167] (Supplemental Figure 3.1). A non-corner-sharing (non-CS) framework is then defined as a framework in which at least one edge or face is shared among the framework polyhedrons (Figure 3.1D-E).

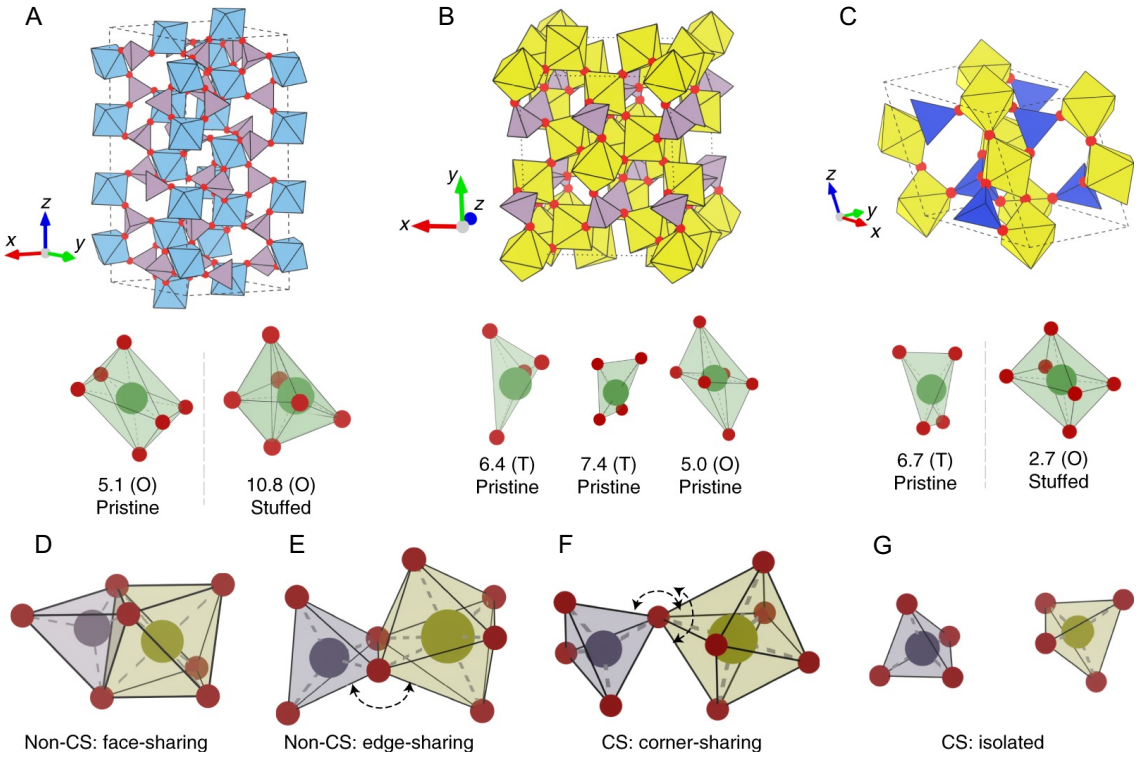


**Figure 3.1 Crystal structure of known superionic conductors with CS frameworks.**

Structures of known CS superionic conductors: $Li_{1+x}Al_xTi_{2-x}(PO_4)_3$ (**A**), $LiTa_2PO_8$ (**B**) and $Li_{1+x}Ta_{1-x}Zr_xSiO_5$ (**C**). The red spheres represent the oxygen atoms at the CS vertex. The lithium environments in each superionic conductor are shown below each framework. CSM values corresponding to tetrahedral (T) and octahedral (O) geometry of the lithium environment are provided for both the lithium when the composition $x$ is 0 (Pristine) and for the stuffed lithium compound when the composition $x$ is larger than 0 (Stuffed). Light blue, light violet, yellow and blue polyhedrons represent Ti, P, Ta and Si sites, respectively. **D**–**G**, The face-sharing (**D**), edge-sharing (**E**), CS (**F**) and isolated (**G**) connectivity of the framework are illustrated. All of the polyhedrons in **D**–**G** represent the polyhedrons of non-lithium

cations. The bidirectional arrows in **E** and **F** indicate the unconstrained rotation directions of the connected polyhedrons.

### 3.4.2 Screening superionic conductors with CS framework

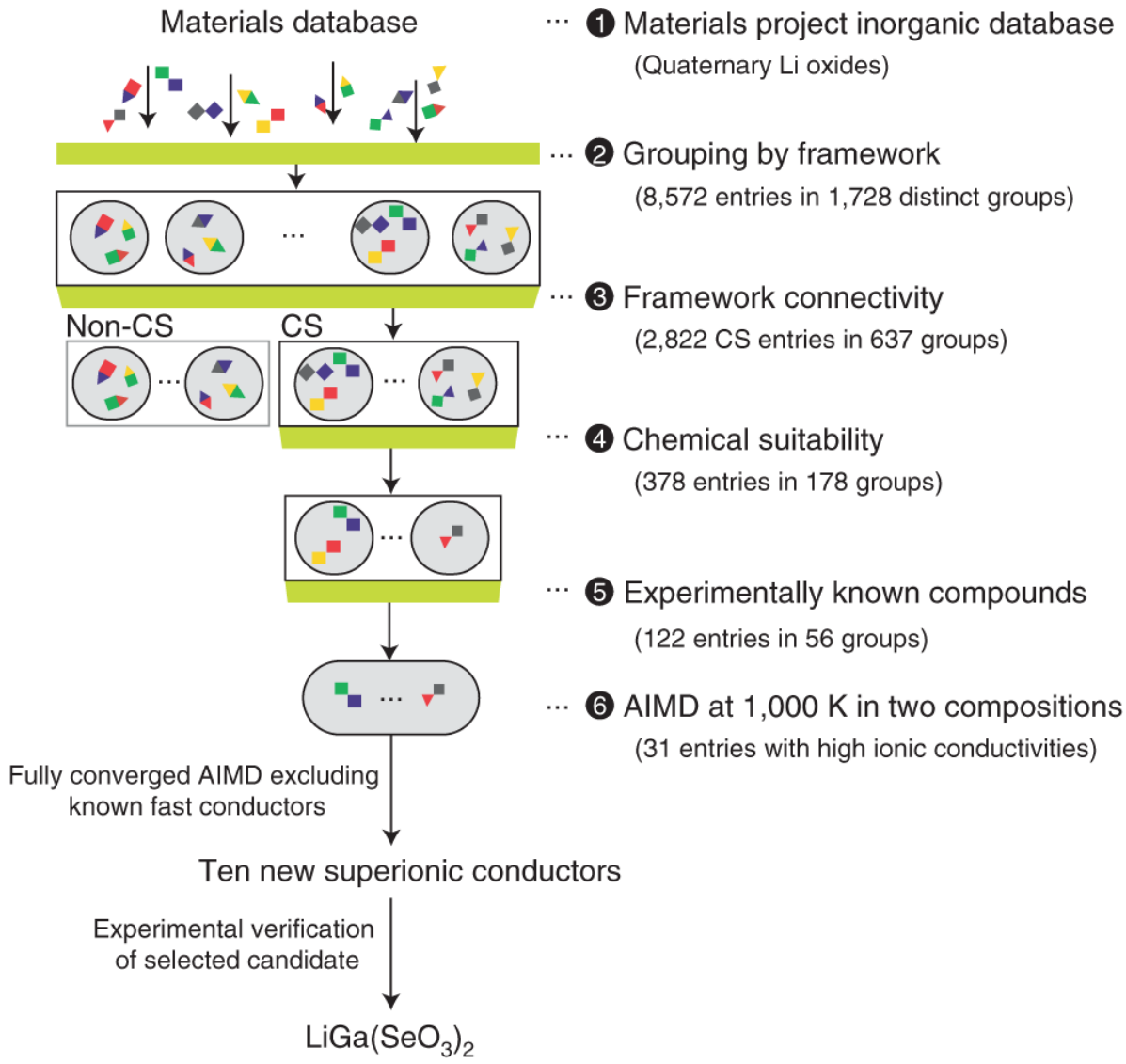


**Figure 3.2 Flowchart of the multi-step computational screening.**

The CS framework defined above can be used as a structural descriptor to discover other potential lithium superionic conductors. To demonstrate this, we perform a multi-step screening process using the Materials Project[168] inorganic crystal

structure database starting from 8,572 compounds of quaternary lithium oxides (Fig 3.2). These are classified into 1,728 distinct structure groups based on the geometry of the framework (anonymizing the species of the non-lithium cations) using a structural matching algorithm.[169] By analyzing the connectivity of polyhedrons in these groups, 637 groups with CS frameworks (2,822 compounds) are identified. Compounds with a computed band gap below 2 eV or compounds containing elements unsuitable for SEs are removed, leaving 378 compounds in 178 groups (see Supplemental Note 3.1 for details). Finally, only the compounds experimentally reported in the ICSD database[170] are selected for the next screening step, yielding 122 compounds in 56 distinct groups.

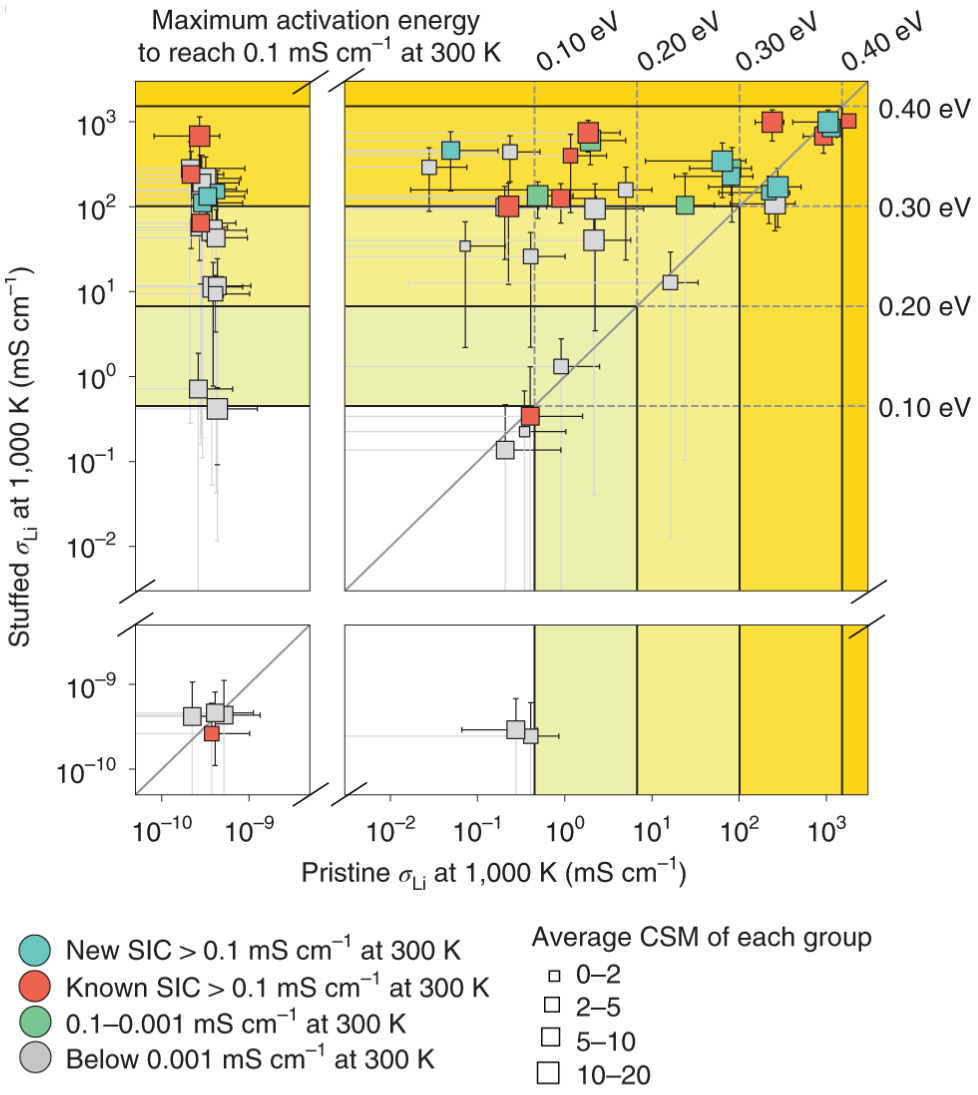


**Figure 3.3 Summary of calculated ionic conductivities of screened materials.**

At the final screening step, one candidate per structure group is selected for further investigation of its ionic conductivity using ab initio molecular dynamics (AIMD) with a target $\sigma_{RT}$ of 0.1 mS cm$^{-1}$ or higher. AIMD simulations are performed at 1,000 K for 10 ps for each candidate. Considering that excess lithium via subvalent doping of the stoichiometric phase is often required to achieve high conductivity (Figure 3.1A, C and Supplemental Table 3.2), the AIMD simulations are performed for two compositions for each candidate: the pristine structure (denoted as Pristine) and the structure with one excess lithium ion stuffed into the supercell (denoted as Stuffed). Details are provided in the Methodology.

In Figure 3.3, the AIMD conductivity at 1,000 K ($\sigma_{1,000\ K}$) of the 56 candidates for two compositions, Pristine and Stuffed, are plotted. Assuming an Arrhenius relationship with 0.3 eV activation energy, which is typical for well-known superionic conductors,[152] a value of $\sigma_{1,000\ K}$ above 101.18 mS cm$^{-1}$ is required to achieve more than 0.1 mS cm$^{-1}$ at RT. The minimal $\sigma_{1,000\ K}$ for other values of the activation energy (ranging from 0.1 to 0.4 eV) can be found from the vertical (for pristine) and horizontal (for stuffed) solid lines. Only four candidates exhibit negligible ionic conductivity in both the Pristine and Stuffed forms, and eight CS frameworks already exhibit high $\sigma_{1,000\ K}$ exceeding 101.18 mS cm$^{-1}$ in the Pristine form. By stuffing a single lithium ion into the supercell, 22 additional CS frameworks can activate high $\sigma_{1,000\ K}$ above 101.18 mS cm$^{-1}$. The orders-of-magnitude improvement of the conductivity upon lithium stuffing cannot be attributed to the quantitative increase of the lithium-ion carrier concentration but rather indicates a qualitative change in the energy landscape.

Lithium stuffing is expected to force lithium into high-energy sites and generate a local group of nearby lithium atoms for which additional Li–Li interaction energy is introduced. Multiple cases where excess lithium stuffing to the stoichiometric phase drastically reduces the activation energy and enhances the ionic conductivity have been reported (Supplemental Table 3.2). For example, the activation energy of $Li_{1+x}Ta_{1-x}Zr_xSiO_5$[165] (Figure 3.1C) decreases from 0.70 eV at the stoichiometric composition to 0.21 eV when the lithium content is increased to $x = 0.25$. These observations indicate that achieving an optimal lithium concentration is vital to activating fast lithium conduction in CS frameworks. Our sampling of both Pristine and Stuffed compositions captures and corroborates such trends.

Among the 56 CS frameworks (Supplemental Table 3.3), we rediscover 12 frameworks[159,161] that have been previously reported as lithium superionic conductors (Supplemental Table 3.1) confirming the selection criteria of our screening process. Among the remaining 44 frameworks, 22 frameworks

corresponding to the dark yellow region of Figure 3.3 (above the 0.3 eV activation line) exhibit a value of $\sigma_{1,000\ K}$ greater than 101.18 mS cm$^{-1}$ in either the Pristine or Stuffed composition. On these materials, fully converged multi-temperature AIMD simulation with appropriate subvalent dopants to introduce extra lithium are performed. This leads to ten new frameworks with conductivity over 0.1 mS cm$^{-1}$ at 300 K as summarized in Table 3.1. Detailed analysis of the ten screened conductors is provided in Supplemental Figures 3.2-3.11. Four frameworks with computed ionic conductivity of 0.001–0.1 mS cm$^{-1}$, as well as the remaining frameworks, are summarized in Supplemental Table 3.S4. In total, 22 from the 56 frameworks are demonstrated to exhibit superionic conductivity at RT. The success rate of 39% in screening superionic conductors based on the CS framework largely surpasses that of random selection[156,157] and other screening studies[161] and indicates that this framework is indeed a critical structural feature appearing in many existing and potential ionic conductors.

**Table 3.1 Summary of properties of 10 screened superionic conductors with a CS framework.**

| Materials Project ID | ICSD ID | Pristine composition | Target composition | $\sigma_{300\ K}$ (mS/cm) | $E_a$ (eV) | Pristine $E_{hull}$ (eV/atom) | Target $E_{hull}$ (eV/atom) | $E_d$ (eV/defect) |
|---|---|---|---|---|---|---|---|---|
| mp-1198930 | 250868 | $LiGa(SeO_3)_2$ | $LiGa(SeO_3)_2$ | 0.212 (0.013, 3.57) | 0.320 ± 0.070 | 0.0 | 0.0 | N/A |
| mp-973966 | 422056 | $LiIn(IO_3)_4$ | $LiIn(IO_3)_4$ | 18.0 (3.57, 90.9) | 0.155 ± 0.040 | 0.0 | 0.0 | N/A |
| mp-559441 | 39761 | $LiTiPO_5$ | $Li_{1+1/16}Ti_{1-1/16}Ga_{1/16}PO_5$ | 1.70 (0.098, 29.7) | 0.212 ± 0.071 | 0.013 | 0.019 | 0.79 |
| mp-14646 | 65025 | $Li_2Mg_2(SO_4)_3$ | $Li_{2+1/4}Mg_2(S_{11/12}P_{1/12}O_4)_3$ | 2.74 (0.145, 52.0) | 0.232 ± 0.073 | 0.0 | 0.011 | 0.81 |
| mp-552663 | 161499 | $LiScAs_2O_7$ | $Li_{1+3/8}Sc_{1-3/8}Mg_{3/8}As_2O_7$ | 23.3 (4.26, 128) | 0.177 ± 0.042 | 0.0 | 0.021 | 0.64 |
| mp-1020018 | 428002 | $Li_5B(SO_4)_4$ | $Li_{5+1/4}B(S_{15/16}P_{1/16}O_4)_4$ | 0.330 (0.0368, 4.90) | 0.330 ± 0.061 | 0.008 | 0.023 | 1.56 |
| mp-1020022 | 248343 | $Li_3B(PO_4)_2$ | $Li_{3+1/8}B(P_{15/16}Si_{1/16}O_4)_2$ | 0.166 (0.00721, 3.83) | 0.326 ± 0.078 | 0.014 | 0.028 | 1.63 |
| mp-1020015 | 192496 | $Li_2B_3PO_8$ | $Li_{2+1/8}B_3P_{7/8}Si_{1/8}O_8$ | 0.251 (0.00744, 8.44) | 0.269 ± 0.087 | 0.0 | 0.015 | 1.67 |
| mp-1222376 | 260590 | $LiZnBO_3$ | $Li_{1+2/16}Zn_{1-1/16}BO_3$ | 0.605 (0.0104, 35.3) | 0.220 ± 0.101 | 0.008 | 0.009 | 0.12 |
| mp-556799 | 94355 | $Li_3In(BO_3)_2$ | $Li_{3+1/8}In_{7/8}Zn_{1/8}(BO_3)_2$ | 0.121 (0.0027, 5.33) | 0.300 ± 0.094 | 0.004 | 0.009 | 0.50 |

The pristine and target composition, extrapolated Li-ion conductivity of the target composition at 300 K ($\sigma_{300\ K}$), activation energy of the target composition ($E_a$), pristine and target energy above the hull ($E_{hull}$), and dopant incorporation energy ($E_d$) are listed. The pristine and target compositions are the same if no dopants are introduced. For conductivity and activation energy, estimation of their upper and lower bounds (error bar) are included.

### 3.4.3 Experimental validation of predicted superionic conductors

We pursued $LiGa(SeO_3)_2$ for experimental verification as it does not require excess lithium stuffing to achieve high conductivity, and is predicted to have a three-dimensional diffusion channel, which is desirable in SEs to avoid channel-blocking issues by lithium/cation anti-site defects[171] in lower-dimensional channels. In addition, the compound has been previously synthesized[172] but was not considered as a lithium ionic conductor. Using a solid-state method, we successfully synthesized $LiGa(SeO_3)_2$. Figure 3.4 shows the X-ray diffraction (XRD) pattern of the synthesized $LiGa(SeO_3)_2$, which agrees well with its reference pattern except for some small impurity peaks. The pellet was densified using spark plasma sintering (Supplemental Supplemental Figure 3.12). While full density was not achieved, the scanning electron microscope (SEM) image in the inset of Figure 3.4 shows good connectivity between particles in the densified matrix.

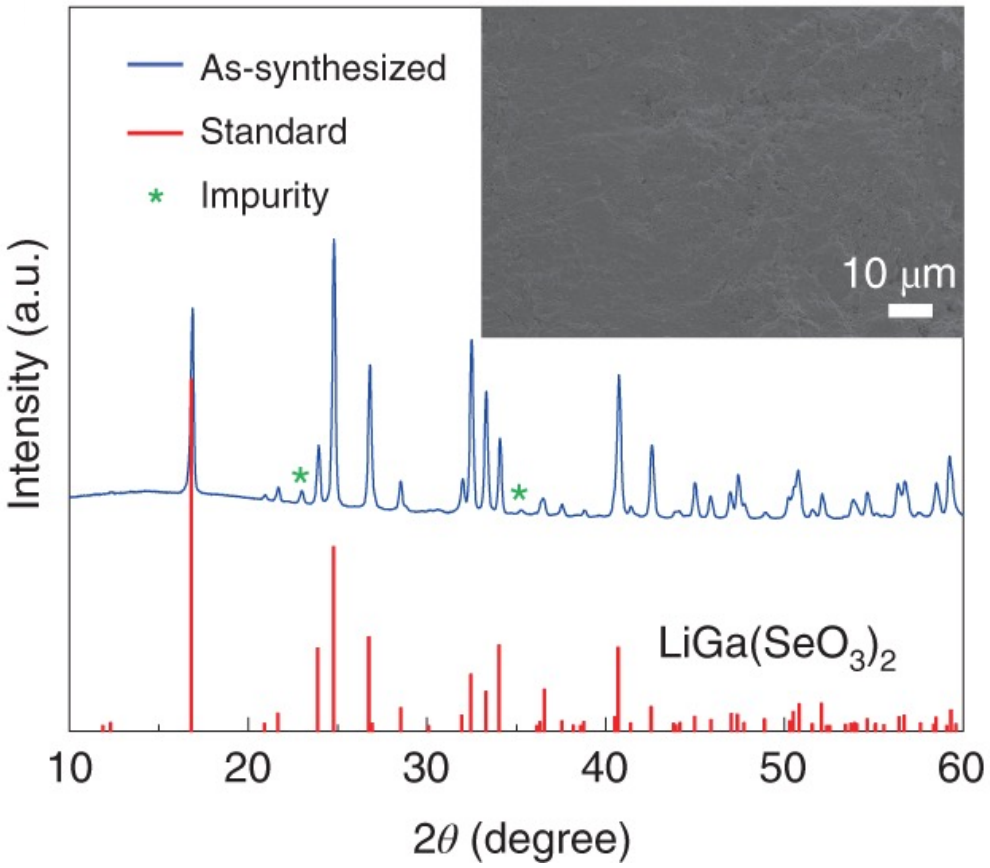


**Figure 3.4 XRD pattern of $LiGa(SeO_3)_2$ with the SEM image of the densified pellet.**

By analyzing the impedance response of a In/$LiGa(SeO_3)_2$/In lithium-blocking cell, we obtained a bulk ionic conductivity of 0.11 mS $cm^{-1}$ at 25 °C, which is in excellent agreement with our prediction of 0.212 mS $cm^{-1}$. The electronic conductivity measured at 25 °C in a d.c. polarization experiment is at least two orders of magnitude lower than the ionic conductivity.

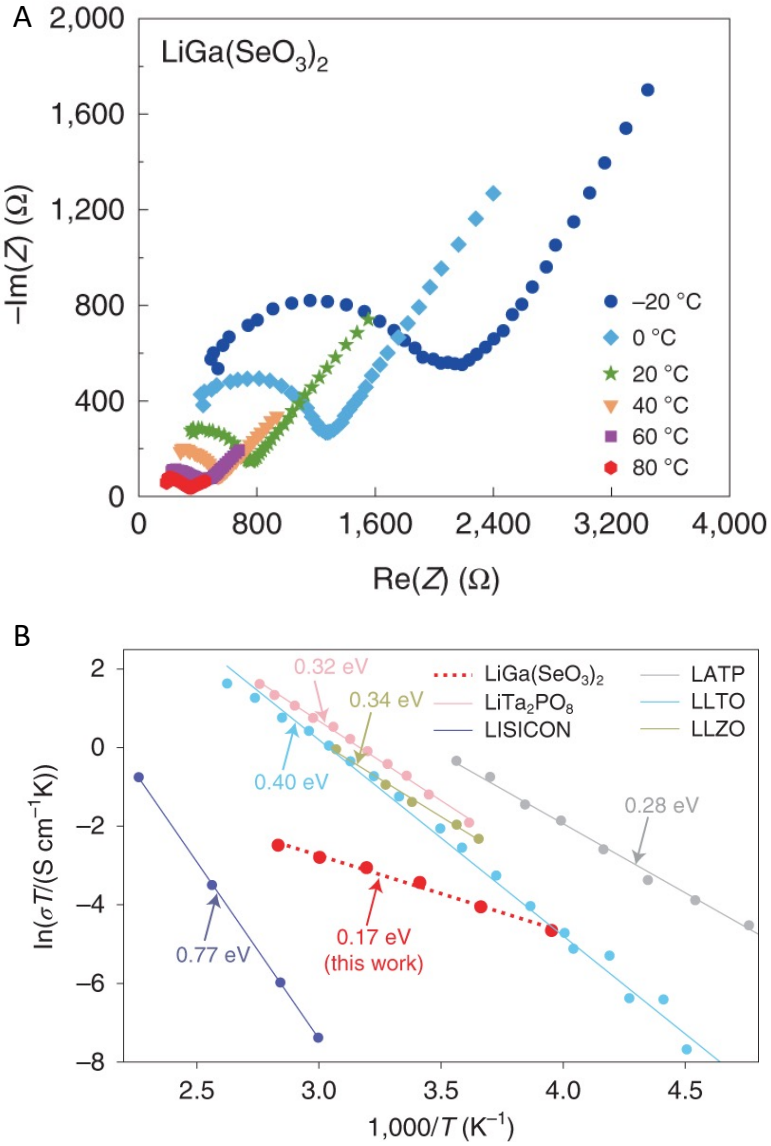


**Figure 3.5 Ionic conductivity and activation energy of $LiGa(SeO_3)_2$.**
**(A)** Temperature-dependent impedance (*Z*) plots of $LiGa(SeO_3)_2$. The plotted semicircle represents the bulk ionic conductivity. **(B)** An Arrhenius plot of the bulk ionic conductivities in comparison to the bulk ionic conductivities of other oxide superionic conductors $LiTa_2PO_8$, LISICON, $Li_{1+x}Al_xTi_{2-x}(PO_4)_3$, $Li_{3x}La_{2/3-x}TiO_3$ (LLTO) and $Li_7La_3Zr_2O_{12}$ (LLZO). a.u., arbitrary units.

$LiGa(SeO_3)_2$ also shows a remarkably low bulk activation energy of 0.17 eV, the lowest value among any known oxide lithium-ion conductors[45,153,162,163,166] (Figure 3.5B). See Methodology and Supplemental Figure 3.13-3.14 for electrochemical analysis. The high ionic conductivity and low activation energy of $LiGa(SeO_3)_2$ validate our prediction that high ionic conductivity can be enabled by CS frameworks, and encourages further investigation of the predicted materials. The fact that the crystal structure of $LiGa(SeO_3)_2$ has been experimentally known[172] yet never thought to exhibit superionic conductivity demonstrates the predictive power of our high-throughput screening in expanding the currently limited list of oxide superionic conductors.

## 3.5 Discussion

### 3.5.1 Distorted Li sites in CS framework

To reveal the physical origin of the high ionic conductivity in the CS frameworks, we take a two-track strategy by systematically investigating both the individual lithium-site geometry as well as the sites' relationship with the framework. We compare the lithium coordination environments in 2,822 compounds with CS frameworks (637 groups) to those in 5,750 compounds with non-CS frameworks (1,091 groups) by calculating the Continuous Symmetry Measure[173] (CSM), where a minimum of 0 corresponds to a perfectly symmetric coordination environment and the maximum of 66.7 corresponds to infinite elongation along one direction[174] (Supplemental Note 3.2).

Figure 3.6 compares the CSM values of octahedral and tetrahedral lithium environments in CS and non-CS frameworks including both occupied and unoccupied lithium sites for each framework. We find that the CS frameworks generally provide a much wider range of degree of distortion in lithium sites, similar to our observations for the three CS superionic conductors in Figure 3.1. The CSM values of tetrahedral and octahedral sites of the CS frameworks are evenly distributed up to a value as high as 15, indicating that the lithium ions are frequently accessing highly distorted environments. However, most of the non-CS frameworks have CSM values near 0, indicating a high propensity for a non-CS framework to provide a highly symmetric environment. Therefore, our analysis indicates that symmetric tetrahedral and octahedral sites are much less frequently provided in CS frameworks. Supplemental Figure 3.15-3.16 provide details of the same set of data with the occupied and unoccupied lithium sites separately analyzed, revealing the

same trend. Details are provided in the Methodology section and Supplemental Note 3.3.

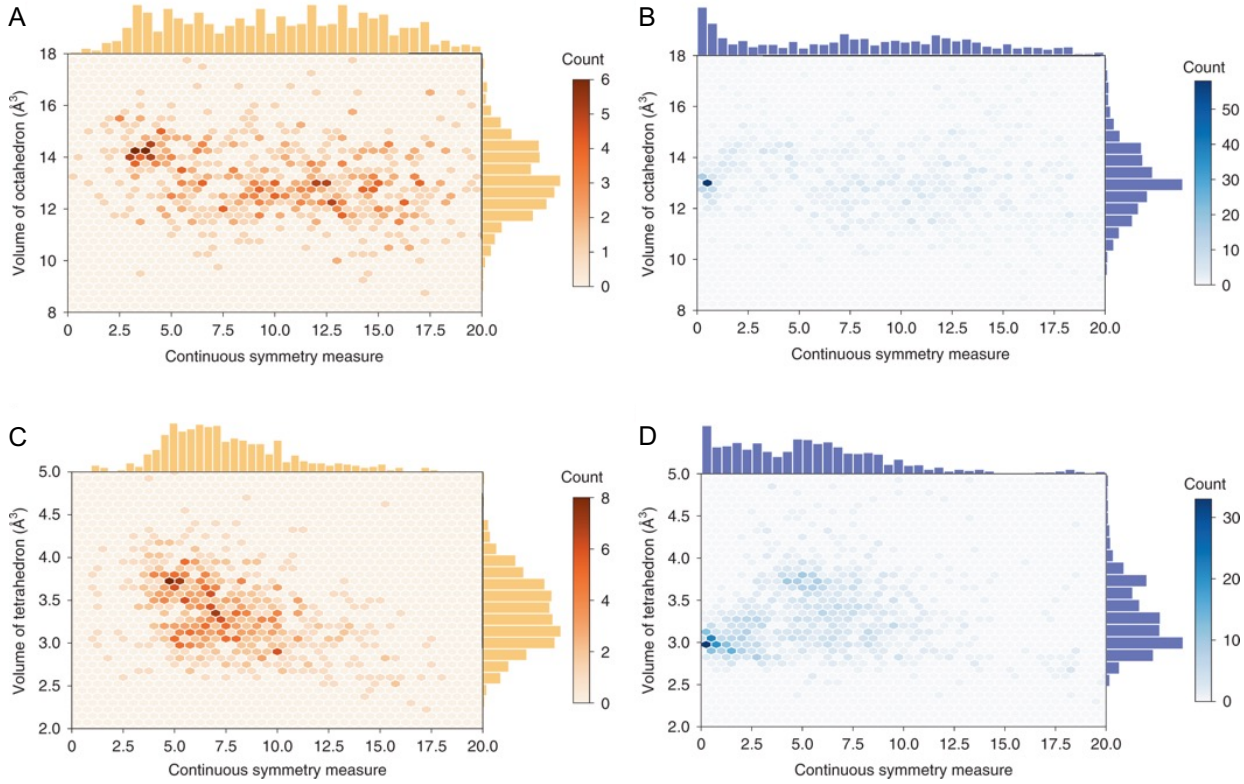


**Figure 3.6 Lithium environment in oxide materials with CS and non-CS framework.**
The octahedral lithium environment for CS (**A**) and non-CS frameworks (**B**), and tetrahedral lithium environment for CS (**C**) and non-CS frameworks (**D**). The colour intensities indicate the number of entries that are populated in a given hexagon. These analyses include both the occupied and unoccupied lithium sites.

The high distortion of lithium sites in structures with a CS framework can be understood from the geometry of the framework polyhedrons. Although lithium can accommodate various extents of distortion, the non-lithium polyhedrons that build up the framework are nearly perfectly symmetric (Supplemental Figure 3.17). This is attributed to the highly covalent nature of bonding in the polyhedra ($PO_4$, $SiO_4$, $SO_4$) or the lower ionic nature of non-lithium metal polyhedrons (Mg octahedron, Ta octahedron, Al tetrahedron) compared with lithium. In contrast, the Li–O bond has a highly ionic nature because lithium's low electronegativity limits the degree of hybridization with the oxygen atom. Therefore, the equilibrium crystal structures prioritize the formation of perfectly symmetric framework polyhedra over a symmetric lithium environment. Furthermore, the degrees of freedom for the relative

positioning of two adjacent non-lithium polyhedrons significantly increase as less oxygen anions are shared between them, as illustrated in Figure 3.1D-G. The higher degrees of freedom in the arrangement of the framework polyhedrons leads to a more irregular geometry of its interstitial space, explaining why CS frameworks tend to have lithium environments with notably larger distortion. We note that a perfectly symmetric lithium environment is not necessarily prohibited in a CS framework, as observed in the perfect tetrahedral lithium sites in CS LISICON frameworks (Supplemental Figure 3.1). Rather, the CS framework allows for a wide range of CSM values, which includes everything from perfect to highly distorted environments.

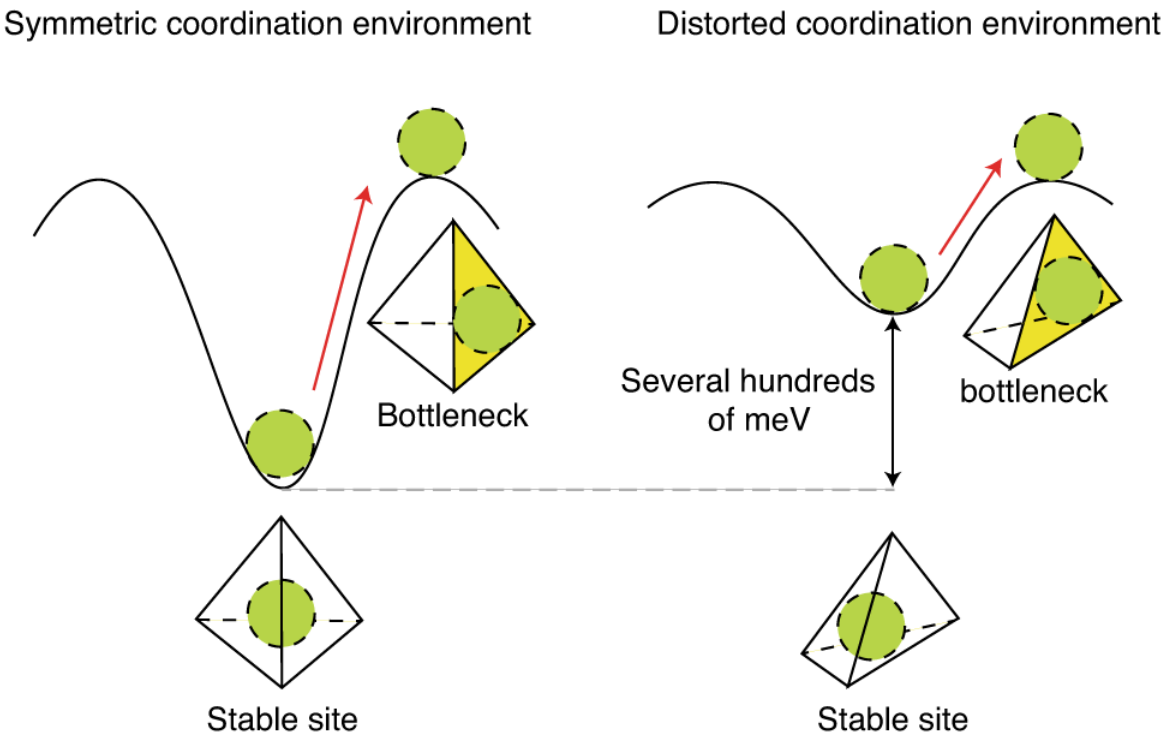


**Figure 3.7 Schematic illustration of the destabilization of lithium sites due to the distortion of the lithium environment.**

The distorted lithium sites in CS frameworks are the key to achieving a lithium-ion energy landscape with low migration energy. Lithium ions have higher energy in the distorted sites than in the symmetric ones. Therefore, migration of lithium from a distorted coordination environment within a CS framework results in a reduction of its activation energy, as illustrated in Figure 3.7. To illustrate the effectiveness of lithium site distortion in enhancing the ionic conductivity, we calculate the kinetically resolved activation energy[175] ($E_{KRA}$) for lithium migration in model

structures with different levels of distortion. $E_{KRA}$ is used to remove the effect of site energy difference on the overall activation energy and solely probes the effect of distortion of the initial site on the migration energy while being independent of the energy state of the final site. To continuously sample a wide range of lithium environments, we trace a Bain path, which is a distortion trajectory that connects a bcc anion lattice to a face-centred cubic (fcc) anion lattice and evaluate the lithium migration energy for different polyhedral volumes, as shown in Figure 3.8. This path enables us to continuously evaluate the effect of distortion on the lithium migration barrier, starting from a perfectly symmetric lithium environment in an fcc anion framework and reaching highly distorted environments as larger strains are applied. Details are provided in the Methodology section.

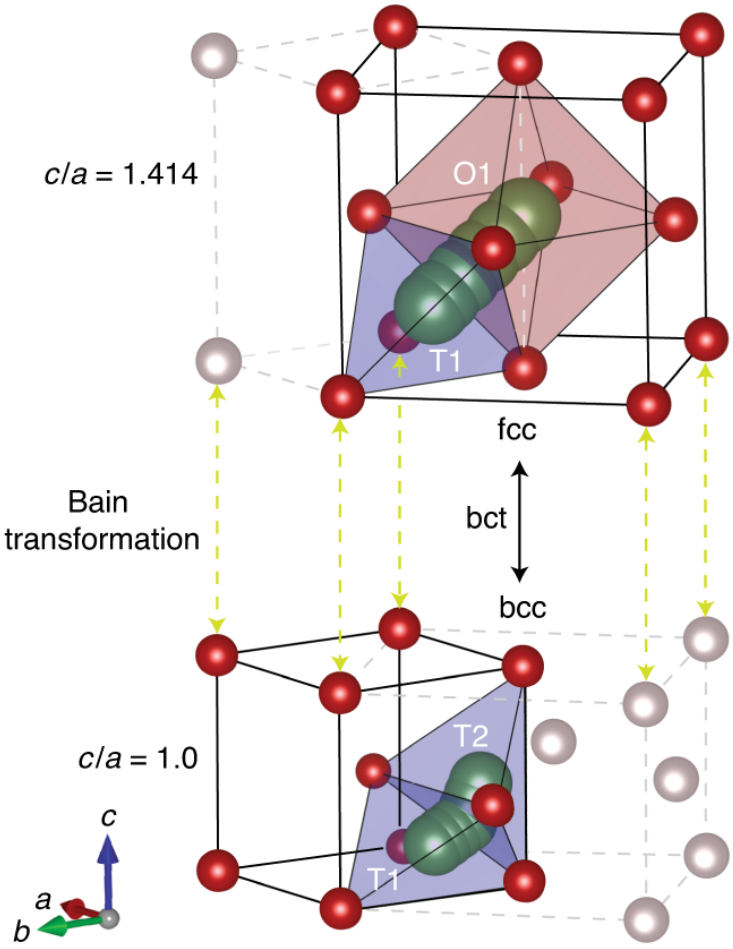


**Figure 3.8 Schematic illustration of Bain transformation model.**
The lithium activation in a wide range of coordination environments is evaluated using model structures along the path of Bain transformation. The shaded triangular face is the bottleneck for lithium migration from its initial site. The lithium and oxygen atoms are shown as green and red (beige if outside the unit cell) circles, respectively.

Figure 3.9 shows the calculated $E_{KRA}$ as a function of polyhedral volume for a series of CSM values from 0 (perfect polyhedrons) to CSM = 4 (significant distortion).

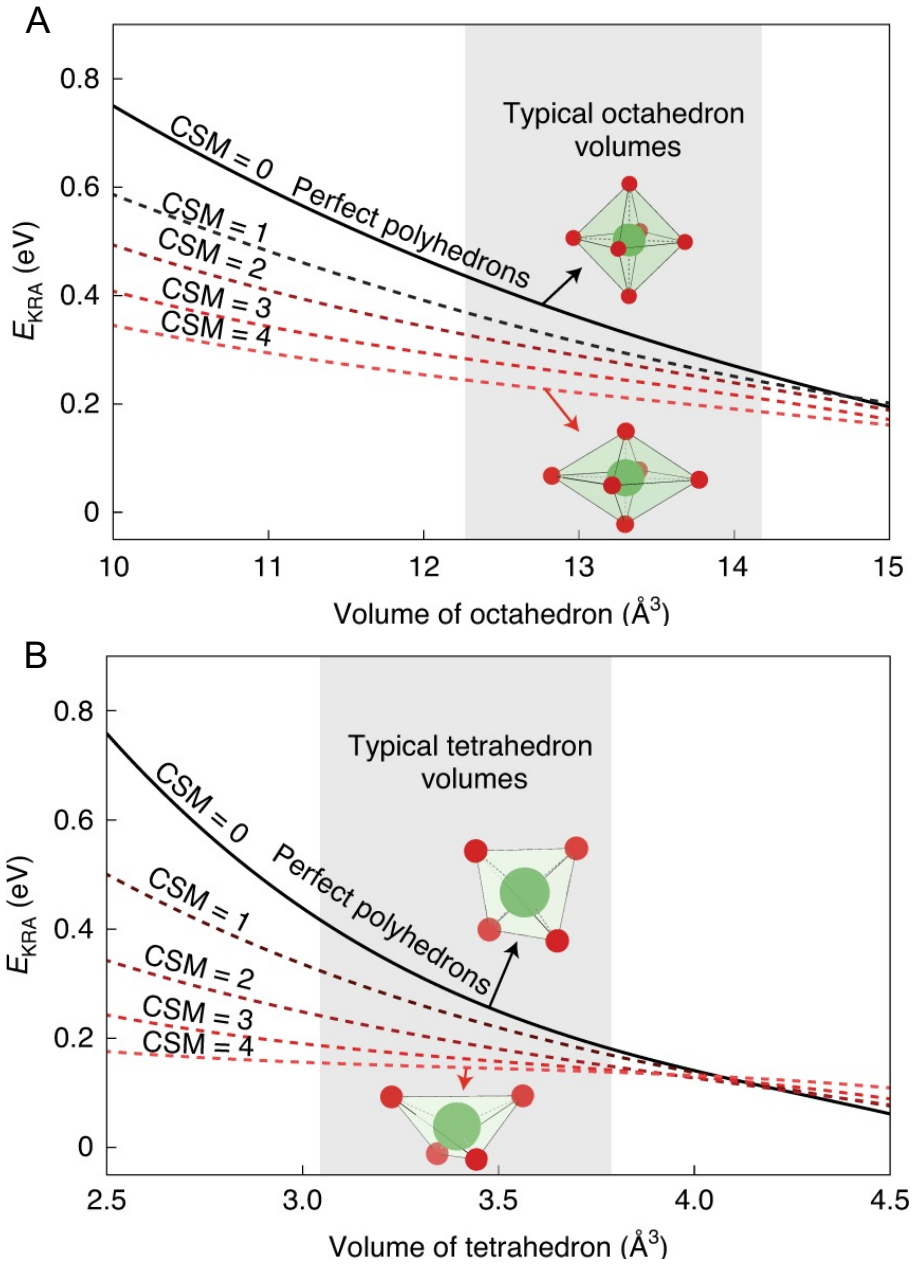


**Figure 3.9 $E_{KRA}$ as a function of polyhedral volume for a series of CSM values.** Calculated lithium-ion kinetically resolved activation energies ($E_{KRA}$) in these model systems are shown for both octahedral (**A**) and tetrahedral (**B**) sites ranging from CSM = 0 (perfect polyhedrons) to CSM = 4. Typical octahedral and tetrahedral volumes from our lithium environment analysis explained in the Methodology section are shown in grey shades. bct, body-centred-tetragonal.

We find that, throughout the typical volume ranges of lithium polyhedrons, $E_{KRA}$ decreases by as much as several hundreds of meV with increasing distortion of the lithium polyhedrons. Our calculations clearly demonstrate that distorting the lithium sites raise their site energies and reduce the energy gap to the transition state, leading to higher ionic conductivity. The effect of the polyhedral volume on the migration barrier is more complicated, with the barrier generally increasing for a smaller polyhedron except for the most distorted polyhedron. The results here align with our previous work[73] and provide a different perspective on the low activation barrier in materials with a bcc anion lattice, where the tetrahedral sites are naturally distorted with a CSM value of 2.3 even for the perfect bcc geometry. Our analysis is also aligned with recent work[159,161,173] that notes the distortion of the anion lattice in superionic conductors.

### 3.5.2 Reduced cation interactions in CS framework

We now demonstrate that the arrangement of the Li sites within the structure of CS frameworks also promotes fast ionic motion. We define the polyhedral packing ratio $\alpha$ as (equation 3.1):

$$\alpha = \frac{Volume\ of\ framework\ polyhedrons}{Volume\ of\ unit-cell} \tag{3.1}$$

Figure 3.10 shows that CS frameworks have a remarkably lower polyhedral packing ratio than non-CS frameworks.

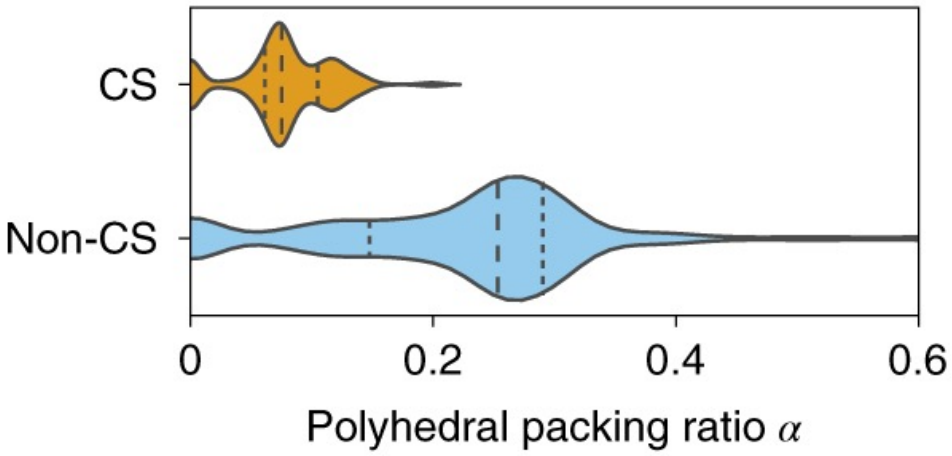


**Figure 3.10 Comparison of the polyhedral packing ratio α of CS and non-CS framework.**

This allows a large fraction of lithium sites to be distant from non-Li cations and reduce the electrostatic repulsion from them. Specifically, Figure 3.11 compares the likelihood of a lithium site being distant from any non-Li cations. The site ratio β is defined as (equation 3.2):

$$\beta = \frac{Distant\ Li\ sites}{Total\ available\ Li\ sites} \tag{3.2}$$

*Distant Li-sites* count the number of Li-sites that do not have any non-Li cations within the cutoff distance of 1.95 Å; for shorter distances than the cutoff, any lithium will form a face-sharing connection with adjacent framework polyhedron (see Methodology section). β is significantly higher for the CS framework, indicating that they have a much higher proportion of Li sites that experience reduced electrostatic interaction from the non-Li cations.

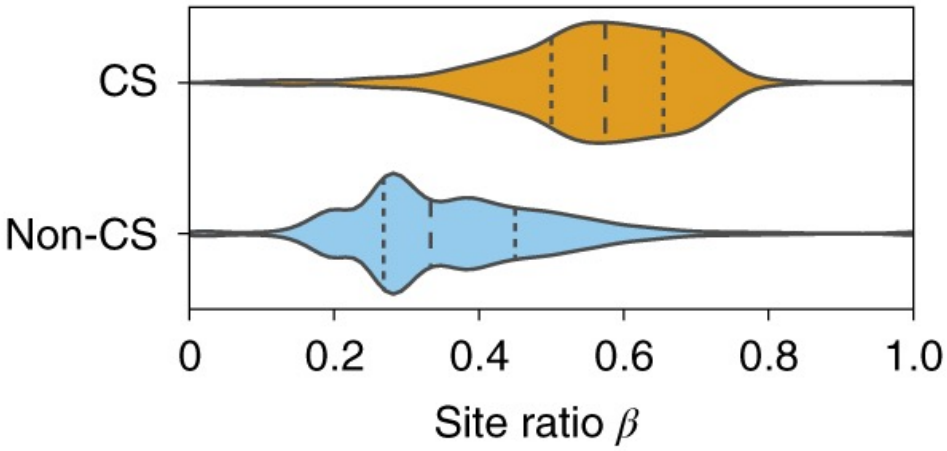


**Figure 3.11 Comparison of the distant site ratio β of CS and non-CS framework.**

Here we define a reduced-repulsion (RR) channel as a percolating channel of distant lithium sites (see Methodology section). By following the RR channel, lithium ions minimize the interaction with non-lithium cations and travel through a relatively flat energy landscape. We show in Figure 3.12, for three examples from the screened candidates, that the RR channels match well with the actual lithium diffusion pathways obtained from AIMD simulations. Considering the weaker screening ability of oxygen anions and the pronounced effect of the arrangement of non-lithium cations on lithium diffusion, RR channels should play a more critical role in oxide conductors than in sulfide conductors.

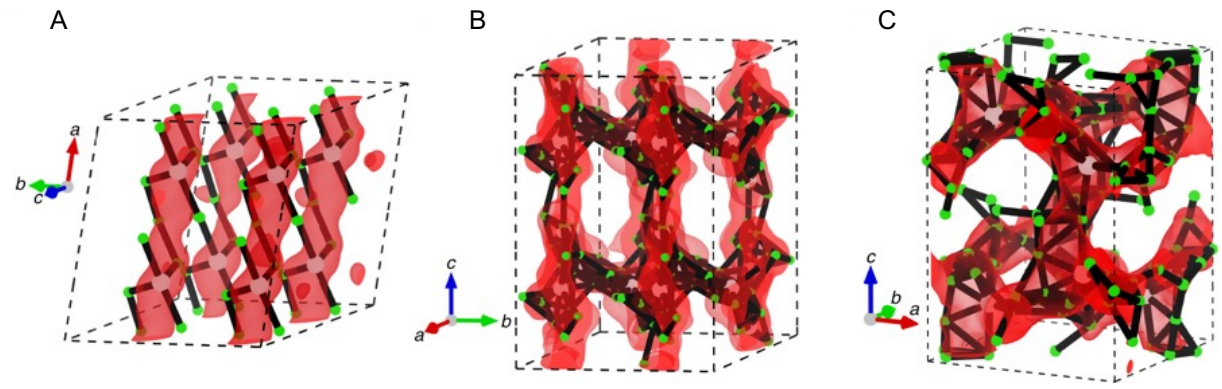


**Figure 3.12 RR channels in three screened conductors with CS frameworks.** The RR channels (solid black lines) in three screened conductors with CS frameworks, $LiScAs_2O_7$ (**A**), $Li_3B(PO_4)_2$ (**B**), and $Li_2Mg_2(SO_4)_3$ (**C**), are shown together with the lithium probability densities from AIMD simulations (red isosurfaces). Isosurfaces are shown in red at $P_0$/100 (**A**), $P_0$/1,000 (**B**) and $P_0$/1,000 (**C**), where $P_0$ is the maximum value of the probability density. The RR channels are shown as connected black edges. The green and white spheres represent occupied and unoccupied lithium sites, respectively, in each crystal structure.

We also find that the CS frameworks are more likely to form high-dimensional RR channels. Figure 3.13 shows that while over 75% of the CS frameworks have a three-dimensional RR channel, more than 75% of the non-CS frameworks have lower-dimension RR channels. Materials with low-dimensional diffusion channels, especially one-dimensional channels, may have limited macroscopic conductivity because of the detrimental effect of channel-blocking defects.[171]

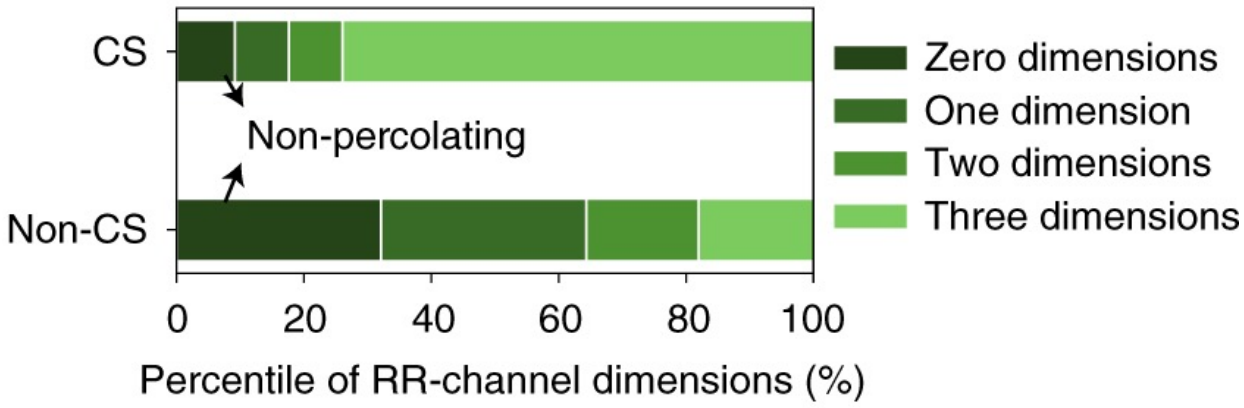


**Figure 3.13 Comparison of the dimension of RR channels of CS and non-CS framework.**

The advantage of CS frameworks can be demonstrated in an exemplary way by taking two compounds ($LiSbP_2O_7$ and $LiNbWO_6$) that can form in both a CS and non-CS polymorph. We find that while the non-CS frameworks exhibit either poor or non-existing lithium motion in AIMD simulations, the CS polymorphs provide fast lithium transport (see the detailed analysis in Supplemental Note 3.4). We note that the similar definition of percolating 0-transition metal (TM) channels in disordered rocksalt cathode materials[176] is actually a subset of our definition of RR channels here. When lithium follows an oct–tet–oct path, as in closed-packed oxides, its migration energy is lowest when the intermediate tetrahedral site face shares with no transition metals (0-TM channels).

In addition to the two aforementioned advantages, the flexible nature of the CS connectivity can promote lithium migration by facilitating relaxation of the framework to accommodate the lithium-ion passing through the bottleneck. As more anions are shared between adjacent cation polyhedrons, the flexibility of the framework to relax during a lithium migration event decrease. While face-sharing connectivity requires at least three commonly shared anions, CS structures have at most one common anion vertex being shared between adjacent cation polyhedrons. This loose restriction on the framework connectivity provides a large number of degrees of freedom for the framework polyhedrons to relax (for example, rotation) and give way for the migrating lithium ion. The rotation of framework polyhedrons in Li,[177,178] Na[122] and Mg[179] ion conductors is an example of the facile relaxation allowed in CS frameworks.

Other oxide superionic conductors with large rare-earth cations such as garnets and perovskites do not have CS frameworks because of their large La polyhedrons, but the origin of their high ionic conductivity can be well understood using similar structural features. The structure of garnet $Li_7La_3Zr_2O_{12}$ is built from large eight-coordinated La polyhedrons, edge-shared among themselves, and Zr octahedrons. Throughout the tet–oct–tet channel connecting 24d and 96h sites, the minimum distance between any Li site and its nearest Zr or La site in a garnet is 2.95 Å (Supplemental Note 3.5). Although the octahedral (96h) Li site face shares with the La polyhedrons, the distance between them is 3.07 Å, which is significantly larger than typical face-sharing distances. Therefore, the tet–oct–tet pathways in garnet structures are indeed RR channels. A similar argument can be made for perovskites (Supplemental Note 3.6). Therefore, although these frameworks form edge/face-sharing connections, the presence of large La cations in garnet and perovskite creates sufficient space to make the lithium pathway a RR channel. Furthermore, the lithium environment in the off-symmetric A site of perovskite can be classified as a highly distorted octahedral site with a CSM value of 16.5–17.4. The fact that the perovskite

structure does not provide any regular tetrahedral or octahedral lithium site suggests its high similarity to the CS frameworks.

## 3.6 Conclusion

In summary, our study highlights the CS framework as an important structural feature of a large class of lithium superionic conductors. The fast diffusion of lithium in such CS frameworks is rationalized by the distorted lithium-site environments these structures create, and from their low polyhedral density creating well-connected RR channels, which minimize electrostatic repulsion from non-lithium cations as lithium ions travel through them. The strong predictive power of the CS structural descriptor was demonstrated in a high-throughput screening, leading to the discovery of ten new frameworks with high computed conductivity. Among them, $LiGa(SeO_3)_2$ was experimentally verified as a new superionic conductor with low activation energy. Our findings provide fundamental insights into the physical attributes that allow fast lithium conduction and project an exciting direction towards the accelerated discovery of superionic conductors for all-solid-state batteries.

## 3.7 Methodology

### 3.7.1 Identifying lithium sites in crystal structures

The algorithm to identify occupied and unoccupied lithium sites in a crystalline lithium oxide is described in Supplemental Figure 3.18. A Delaunay tetrahedralization algorithm[180] was used on the $O^{2-}$ anion lattice to generate '*T* tetrahedral sites' (*T* sites). For each existing lithium ion, a 'lithium polyhedral site' (*L* sites) was constructed by finding its coordinating anions (cutoff distance ≤ 3 Å), and similar for '*M* polyhedral sites' (*M* sites) for each non-lithium (*M*) cation. Two sites were defined to be 'in conflict' with each other if their centre distance was ≤1 Å. Next, any *T* sites that were 'in conflict' with any *M* sites were removed, and the remaining *T* sites were recursively merged if they were both distorted (Robert/Roux factor ≤ 0.94)[181] and too close to each another (centre distance ≤ 1.1 Å). This step produced 'candidate polyhedral sites' (*P* sites) consisting of the unmerged *T* sites and also the new sites from merging. Finally, we designated any *P* sites that were 'in conflict' with any *L* sites as the occupied lithium sites and the remaining *P* sites as the unoccupied lithium sites. All numerical values were selected to reproduce the known lithium sites in experimentally identified structures, including garnet,

NASICON, layered $LiCoO_2$ and spinel $LiMn_2O_4$. In the newly predicted structures, stuffed lithium was inserted in the lowest energy site according to DFT calculations.

### 3.7.2 Coordination environments in CS and non-CS frameworks

Two CSM values of each lithium site were calculated referencing to a perfect tetrahedron and a perfect octahedron, and denoted as $CSM_{tet}$ and $CSM_{oct}$, respectively. The site was then assigned as a tetrahedral site if $CSM_{tet}$ was smaller than $CSM_{oct}$ (that is, if the site was geometrically closer to a perfect tetrahedron than to a perfect octahedron) and vice versa (Supplemental Note 3.3). To remove the bias in our dataset towards fcc anion frameworks resulting from extensive experimental studies on cathode materials, all the structures were grouped by the geometry of their frameworks using a structural matching algorithm.[169] A representative structure was randomly selected from each group. $CSM_{tet}$ and $CSM_{oct}$ values were averaged over all tetrahedral and octahedral lithium sites in the structure, respectively, to represent the coordination environments in the group.

### 3.7.3 Phase stability of compounds with aliovalent dopants

Density functional theory (DFT) calculations were performed with the Perdew–Burke–Ernzerhof generalized gradient approximation[182] (GGA) using the projector augmented wave method[183] as implemented in the Vienna ab initio simulation package[184]. A mixed scheme of the GGA and GGA + U methods was used[185], and the selection of *k*-point grid and energy cutoff was consistent with the computational settings in the Materials Project[168]. The phase stability of each compound was evaluated by generating the convex hull formed by the ground-state phases in the chemical space defined by all of the elements in the material, including the dopant species using the pymatgen software package.[169] Materials above the convex hull are expected to decompose into their nearest phase on the facet of the convex hull. The energy above the hull as well as the dopant (defect) incorporation energy were calculated to evaluate the stability of the doped compound. The dopant incorporation energy was calculated as (equation 3.3)[186]:

$$E_d = E_{doped} - E_{pristine} + \sum_i \Delta n_i \mu_i \tag{3.3}$$

where $E_{doped}$ and $E_{pristine}$ are the DFT energies of the supercells with and without dopants, $\mu_i$ is the chemical potential of the element $i$ on the convex hull and $\Delta n_i$ is

the change in the number of atoms of element *i* in the supercell to introduce the dopants.

### 3.7.4 Lithium site distortion and its effect on lithium migration barrier

Bcc anion frameworks with volumes between 10 $Å^3$ per O and 34 $Å^3$ per O at an interval of 1 $Å^3$ per O were generated covering the typical volume range of the tetrahedral and octahedral lithium sites in the lithium oxides, as shown in Figure 3.6. To sample various degrees of distortion of lithium environments, a Bain transformation was applied by elongating the *c* axis from $c/a = 0.4$ to $c/a = 1.7$ at an interval of 0.05. Structures with $c/a$ values that are not 1.0 (bcc) or 1.414 (fcc) have body-centred-tetragonal anion frameworks. $E_{KRA}$ was calculated from the site energies of the T1 site, the T2 or O1 site and the planar triangular bottleneck using DFT structure optimization. The discrete results at various distortions and volumes were interpolated to obtain the $E_{KRA}$ as a function of CSM and volume per polyhedron. Sample points where the lithium placed at the O1 site escapes from the octahedral site after relaxation or where the site energy at the planar triangular bottleneck is lower than the T1 site or the T2 or O1 site were excluded.

### 3.7.5 Identification of RR channel

In computing the site ratio $\beta$ and identifying the RR channels, we searched for lithium sites that have no non-lithium cations within a radius of 1.95 Å. This cutoff distance between a lithium site and its nearest non-lithium cation was chosen to set the boundary between a corner- or edge-sharing connectivity and a face-sharing connectivity. A typical lithium non-lithium cation distance of a corner- or edge-sharing connectivity is larger than 1.95 Å, whereas that of a face-sharing connectivity is smaller than 1.95 Å. For example, the distance between the edge-sharing P and Li polyhedrons is 2.69 Å in $LiFePO_4$, that of a CS Zr–Li connection is 2.94 Å in LLZO and that of a CS Li–Mn is 3.49 Å in spinel $LiMn_2O_4$. In contrast, the distance between an octahedral site and a face-sharing activated tetrahedral site in lithium disordered rocksalt is 1.79 Å.[176] We identify RR channels by connecting nearby lithium sites within 2.3 Å and determine the dimensionality of the RR channels by evaluating their percolation in the crystal structure.

### 3.7.6 AIMD simulations

AIMD simulations were performed using gamma-point-only sampling of *k*-space and a plane-wave energy cutoff of 520 eV. Spin polarized calculations were performed if the magnetic moment appeared during the DFT total energy calculation. In the short AIMD of lithium-stuffed compounds, a background charge was applied to retain the oxidation states of the framework atoms. For both the short AIMD simulation and the fully converged AIMD simulation, the samples were heated to the target temperature over 2 ps using velocity scaling, and then were equilibrated at the target temperature for 5 ps in the NVT ensemble (i.e. constant number of atoms, volume and temperature) using a Nosé–Hoover thermostat. For the short AIMD, we then performed the simulation for diffusion in the NVT ensemble for 10 ps. For the fully converged AIMD simulation of the ten new superionic conductors, we sampled diffusion events for 100–500 ps per temperature in the NVT ensemble until the diffusion coefficient converged. For each compound, at least five temperatures were simulated for the linear fitting of the Arrhenius relationship. The diffusion coefficient was evaluated using the mean squared displacement based on the methodology established in previous work.[124] The lithium ionic conductivity was calculated from the diffusion coefficient based on the Einstein relation. No signs of melting at high temperature were observed. Error analysis was performed based on the empirical relationship between the total mean squared displacement and the relative standard deviation of the diffusion coefficient.[187] In a few cases with insufficient numbers of hopping events, the lower limit of the error bar was drawn in light grey arbitrarily down to 1/1,000 of the computed conductivity from the 10 ps AIMD simulation.

### 3.7.7 Synthesis

$LiGa(SeO_3)_2$ was synthesized via a solid-state method. Here 0.2096 g lithium carbonate ($Li_2CO_3$, Sigma-Aldrich, 99.99% trace metal basis), 0.5316 g gallium (III) oxide ($Ga_2O_3$, Sigma-Aldrich, >99.99 trace metal basis) and 1.2588 g selenium dioxide ($SeO_2$, Sigma-Aldrich, >99.9 trace metal basis) were mixed in the appropriate stoichiometric ratio. The mixtures were hand ground in an agate mortar for 15 min and transferred into a zirconium oxide ball mill jar together with two large zirconium oxide balls (10 mm in diameter) and 25 small zirconium oxide balls (5 mm in diameter). The mixture was then ball milled (SpexSamplePrep 8000 M) for 1 h. After ball milling, the mixture was pressed into pellets 6.0 mm in diameter under a pressure of 2.0 metric tons for 4 min. The pellets were put into an alumina combustion boat and calcined at 310 °C for 48 h under argon flow to obtain

$LiGa(SeO_3)_2$. All the experimental procedures are carried out in an argon atmosphere with <0.1 ppm of $O_2$ and $H_2O$.

## 3.7.8 Electrochemical characterization

The lithium-ion conductivity was evaluated using electrochemical impedance spectroscopy (EIS) with indium metal as blocking electrodes at temperature ranging from −20 °C to 80 °C. As-synthesized $LiGa(SeO_3)_2$ was sintered to a ~1-mm-thick pellet with a diameter of 12.7 mm via spark plasma sintering (Thermal Technology LLC, Model DCS25). LiCl (3 wt%) was used as a sintering additive. During the sintering, the powder was uniaxially compressed using a WC-6% Co press die under a pressure of 160 MPa at 300 °C. The as-obtained pellet was then sandwiched between two indium films and transferred into Bio-Logic leak-tight sample holders (CESH) for EIS measurements. EIS measurements were performed using an EC-Lab Electrochemistry, SP300 (Bio-Logic). The measurements were conducted at the initial open-circuit voltage in the frequency range of 7 MHz to 100 mHz with the application of a 10-mV signal amplitude. A Bio-Logic intermediate temperature system was used to control the temperature of the sample holder. The electronic conductivity was evaluated using a d.c. polarization test. A 20 mV d.c. voltage was applied on the $In/LiGa(SeO_3)_2/In$ cell.

## 3.7.9 Structural characterization

Powder XRD data was collected using a Rigaku MiniFlex 600 diffractometer with Cu Kα radiation. SEM images were obtained on a Zeiss Gemini Ultra-55 analytical field-emission scanning electron microscope at the Molecular Foundry at Lawrence Berkeley National Laboratory.

## 3.8 Supporting information

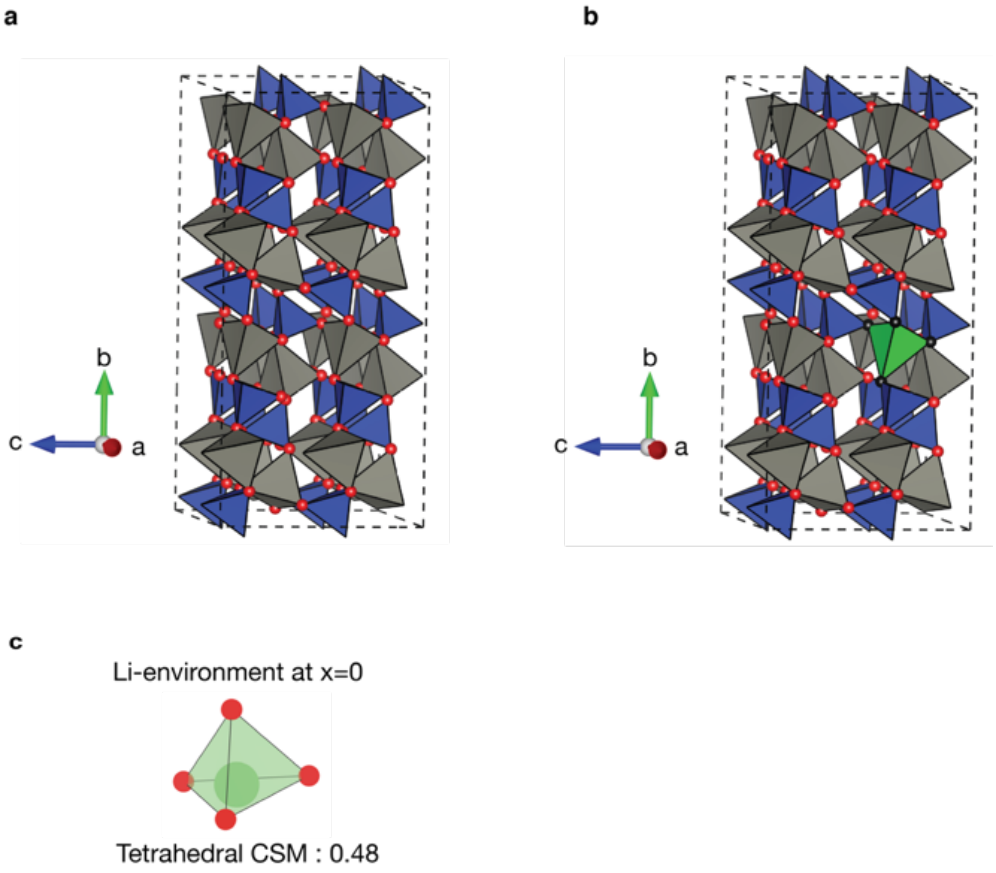


**Supplemental Figure 3.1 Isolated polyhedron in LISICON $Li_{2+2x}Zn_{1-x}SiO_4$ framework at x>0.**
LISICON-type conductors are isostructural to γ-$Li_3PO_4$ and have the composition $Li_{2+2x}M_{1-x}XO_4$ (M=Zn, Mg, Ca and X=Ge, Si, Ti). Optimal conductivity in the LISICON framework is achieved at x=0.75, where the framework is stuffed with lithium in the M site as well as interstitial sites. (a) A typical LISICON compound $Li_2ZnSiO_4$ forms a CS framework of a Zn tetrahedron (grey) and Si tetrahedron (blue). The CS oxygen vertexes are shown as red spheres. (b) As lithium atoms are stuffed into the framework (x>0 in $Li_{2+2x}Zn_{1-x}SiO_4$), part of the Zn tetrahedrons are substituted by the stuffed Li (green tetrahedron). The green tetrahedron is not included in the framework because the framework is defined by the set of polyhedrons of *non-Li cations*. Therefore, the black oxygen vertex becomes isolated in the framework. These frameworks with an isolated oxygen vertex are included in the CS frameworks. (c) The Li environment at x=0 is shown. The CSM value is 0.48, indicating that nearly perfect symmetry is not prohibited in CS frameworks.

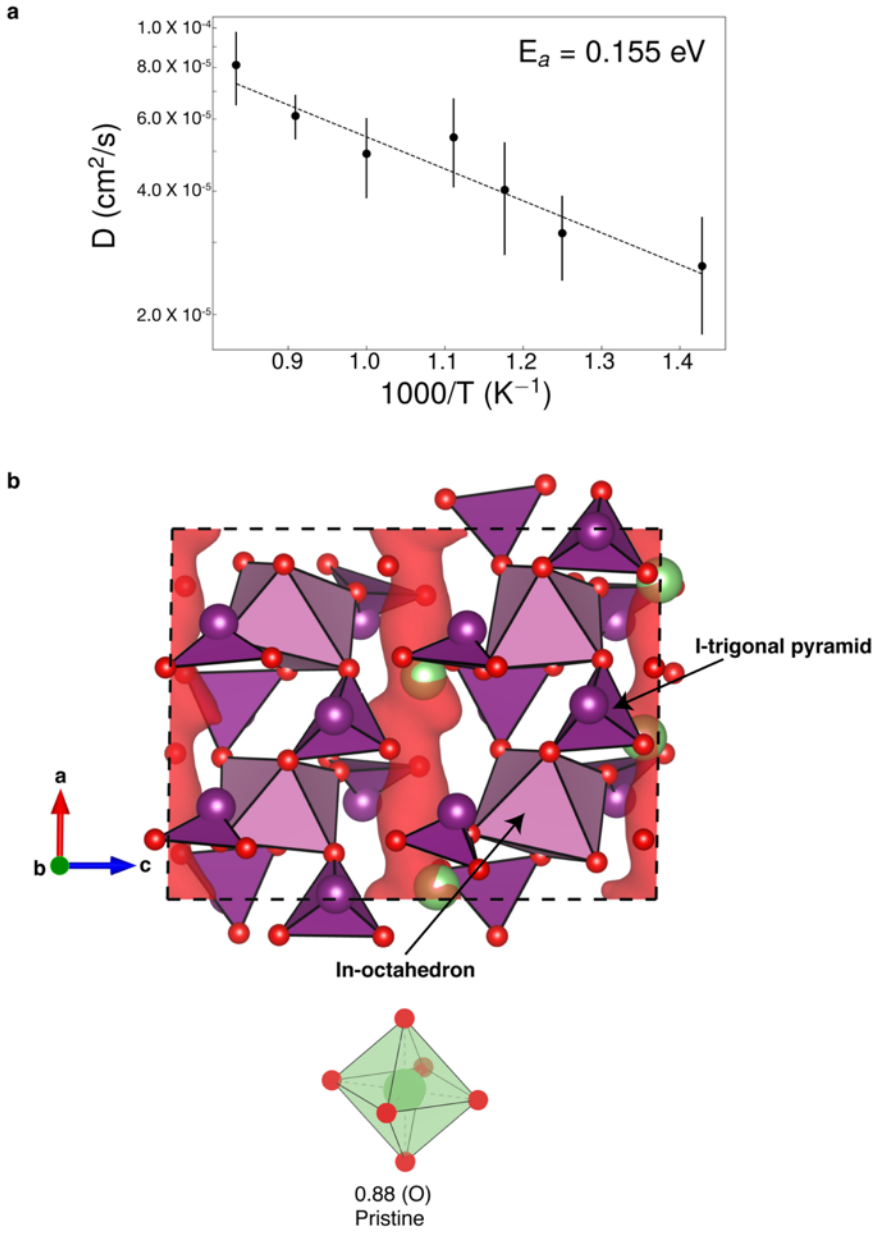


**Supplemental Figure 3.2 In-depth analysis of novel SIC $LiIn(IO_3)_4$.**
(a) Arrhenius plot of Li-ion diffusion coefficient showing an activation energy of 155 ± 40 meV. (b) Isosurface of Li-ion probability density from AIMD simulation at 1000 K. It shows the isosurface of $P = P_{max} / 100$ (red), where $P_{max}$ is the maximum value of the probability density. The CS frameworks in $LiIn(IO_3)_4$ consist of In octahedrons (light violet) and I trigonal pyramids (dark purple). The green and red spheres represent Li and O atoms, respectively. The Li environment is illustrated below as well.

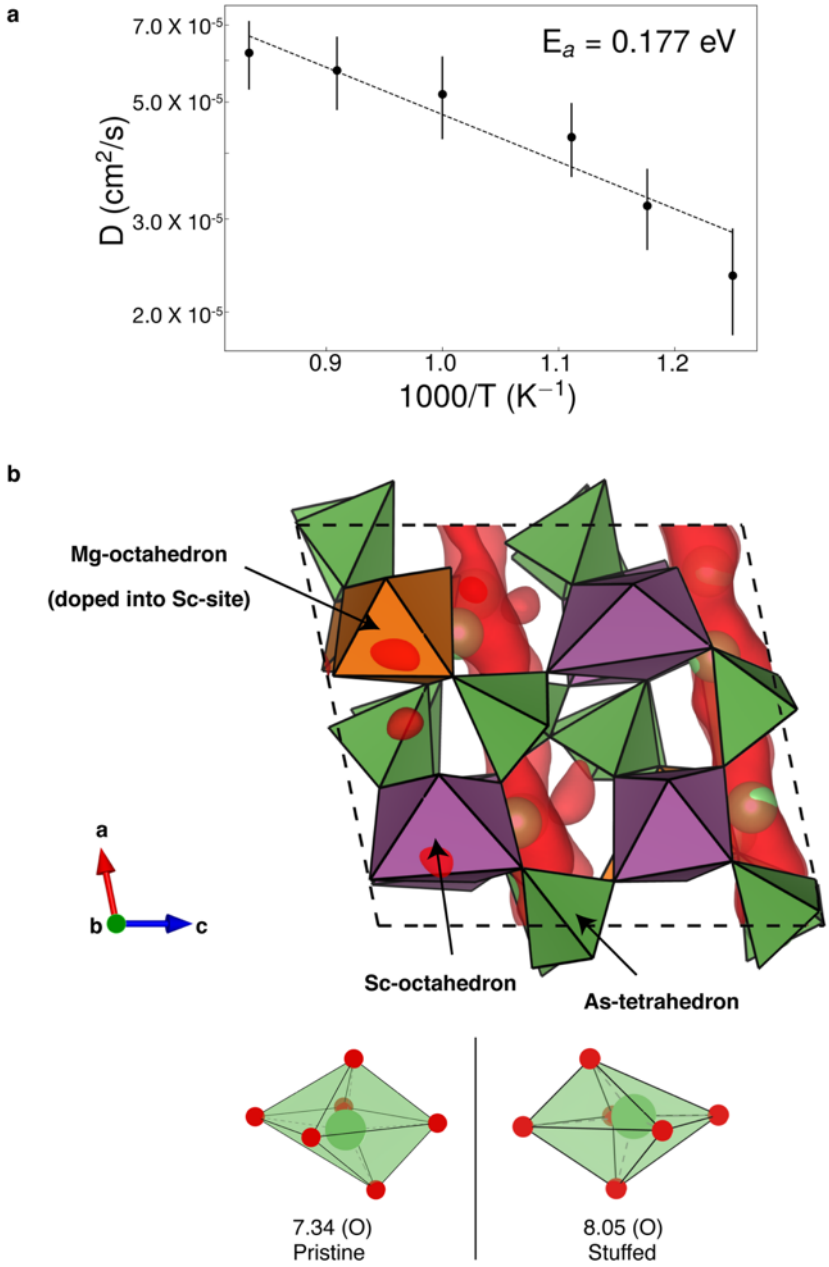


**Supplemental Figure 3.3 In-depth analysis of novel SIC $LiScAs_2O_7$.**
(a) Arrhenius plot of Li-ion diffusion coefficient showing an activation energy of 177 ± 42 meV. (b) Isosurface of Li-ion probability density from AIMD simulation at 1000 K. It shows the isosurface of $P = P_{max} / 100$ (red), where $P_{max}$ is the maximum value of the probability density. The CS frameworks in $LiScAs_2O_7$ consist of Sc octahedrons (violet) and As tetrahedrons (green). The orange octahedron represents the Mg dopant substituting the Sc octahedron. The green spheres represent Li atoms. The Li environments are illustrated below as well.

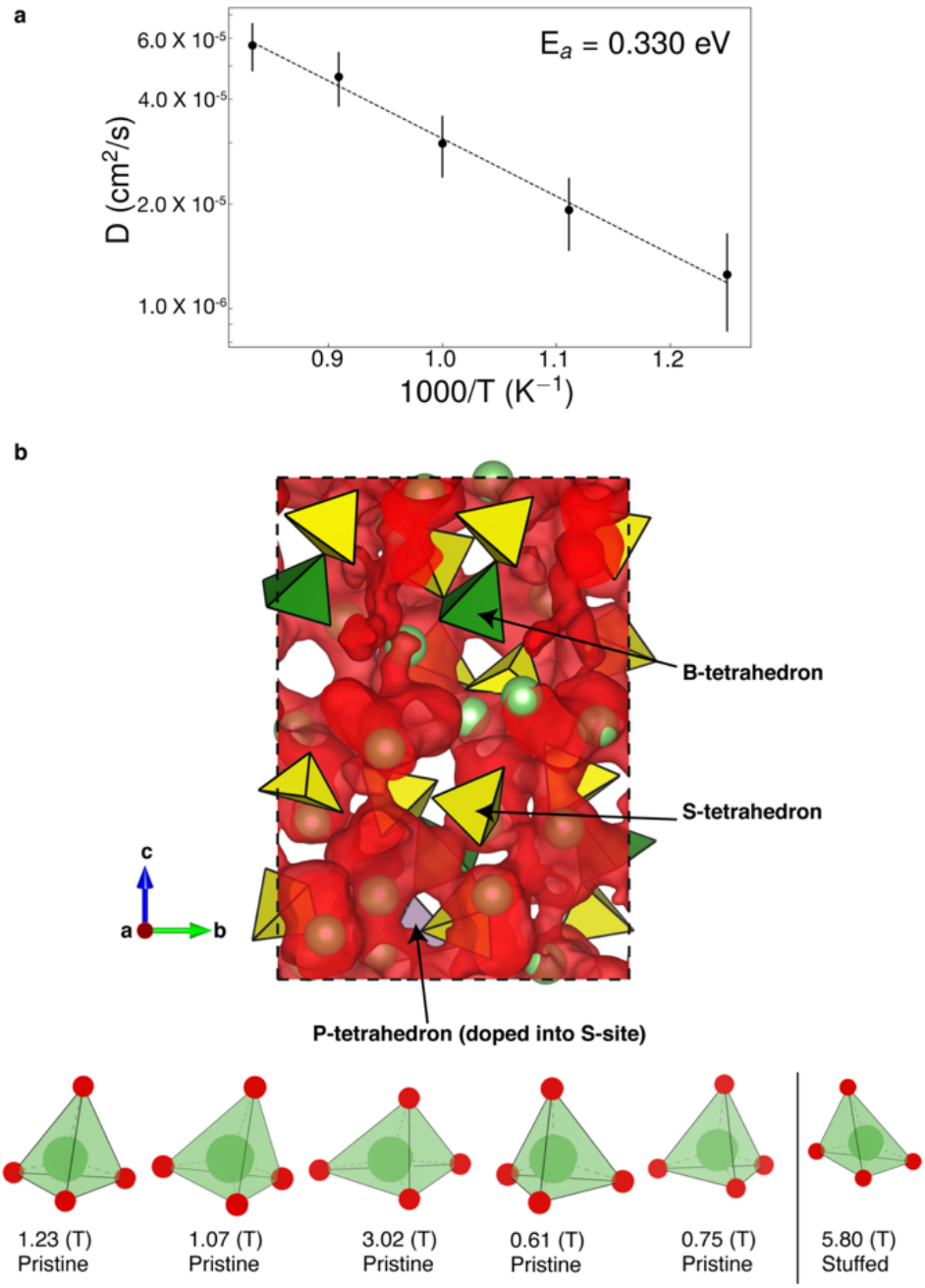


**Supplemental Figure 3.4 In-depth analysis of novel SIC $Li_5B(SO_4)_4$.**
(a) Arrhenius plot of Li-ion diffusion coefficient showing an activation energy of 330 ± 61 meV. (b) Isosurface of Li-ion probability density from AIMD simulation at 1000 K. It shows the isosurface of $P = P_{max} / 50$ (red), where $P_{max}$ is the maximum value of the probability density. The CS frameworks in $Li_5B(SO_4)_4$ consist of B tetrahedrons (green) and S tetrahedrons (yellow). The light-violet tetrahedron represents P dopant substituting the S tetrahedron. The green spheres represent Li atoms. The Li environments are illustrated below as well.

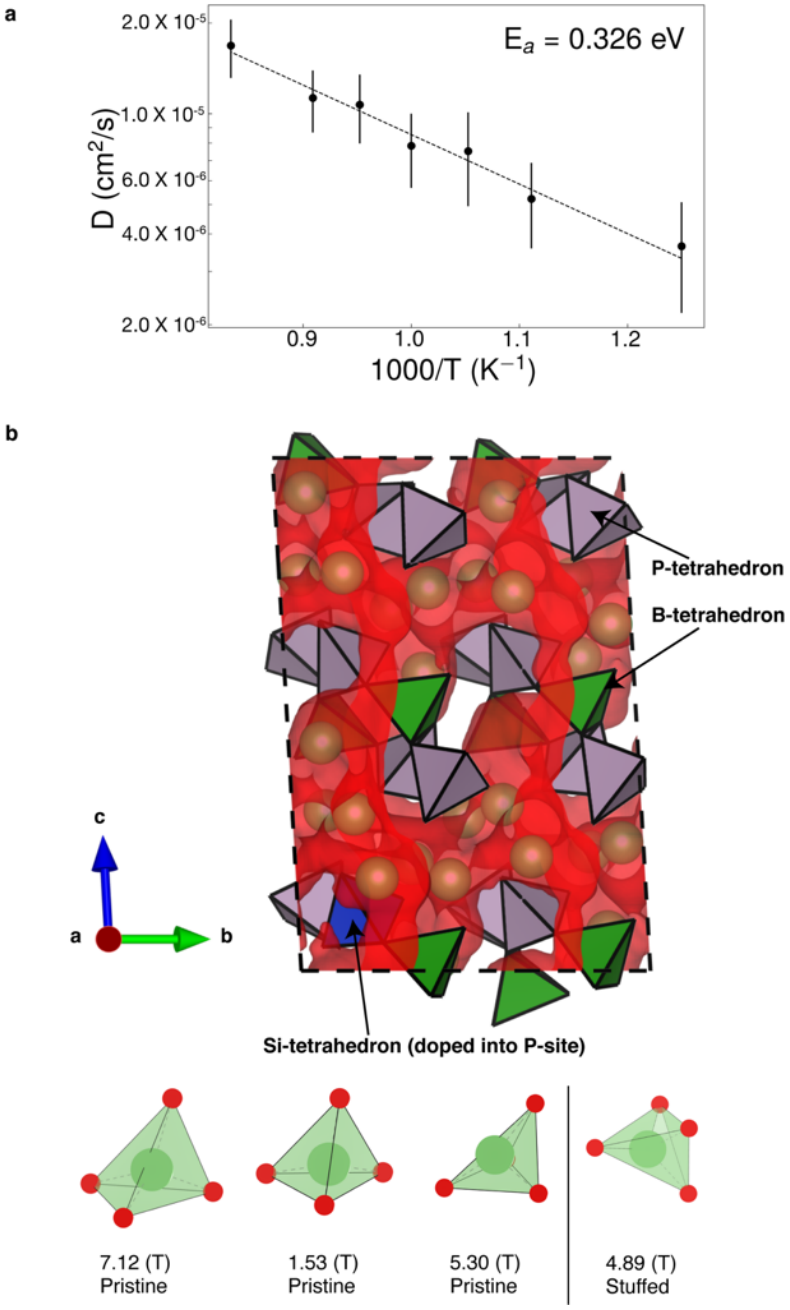


**Supplemental Figure 3.5 In-depth analysis of novel SIC $Li_3B(PO_4)_2$.**
(a) Arrhenius plot of Li-ion diffusion coefficient showing an activation energy of 326 ± 78 meV. (b) Isosurface of Li-ion probability density from AIMD simulation at 1000 K. It shows the isosurface of $P = P_{max} / 500$ (red), where $P_{max}$ is the maximum value of the probability density. The CS frameworks in $Li_3B(PO_4)_2$ consist of B tetrahedrons (green) and P tetrahedrons (light violet). The blue tetrahedron represents Si dopant substituting the P tetrahedron. The green spheres represent Li atoms. The Li environments are illustrated below as well.

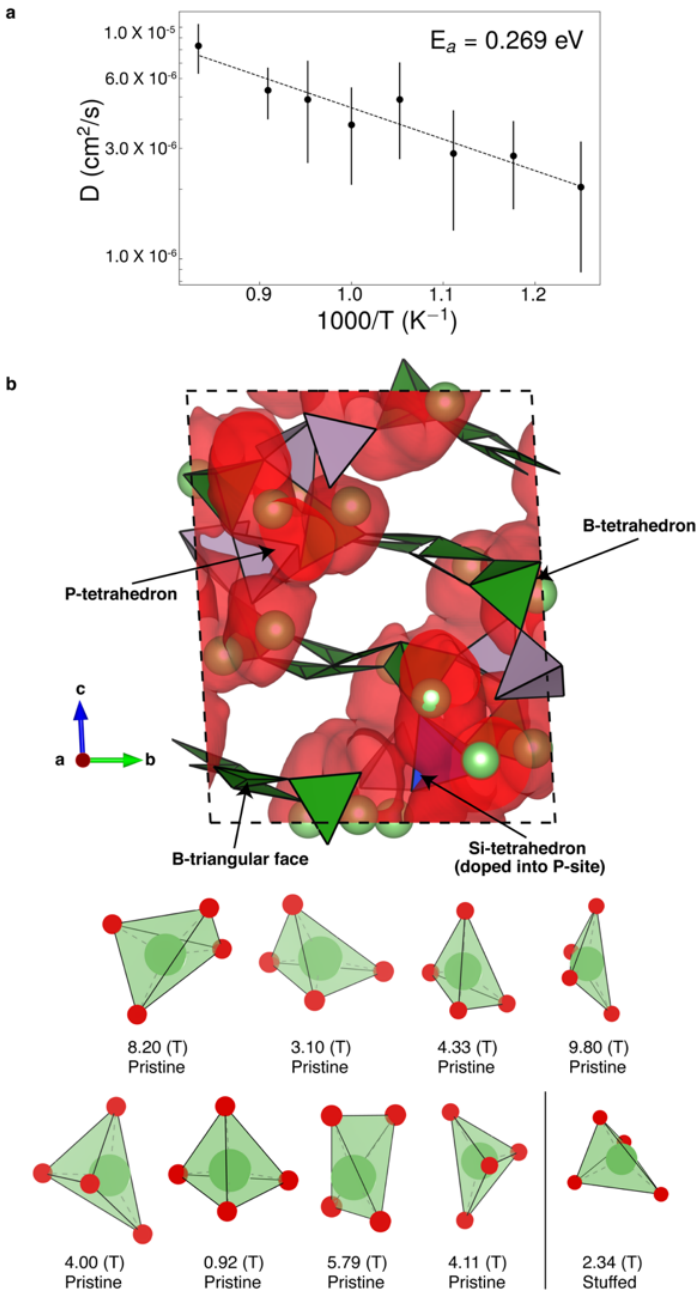


**Supplemental Figure 3.6 In-depth analysis of novel SIC $Li_2B_3PO_8$.**
(a) Arrhenius plot of Li-ion diffusion coefficient showing an activation energy of 269 ± 87 meV. (b) Isosurface of Li-ion probability density from AIMD simulation at 1000 K. It shows the isosurface of P = $P_{max}$ / 1000 (red), where $P_{max}$ is the maximum value of the probability density. The CS frameworks in $Li_2B_3PO_8$ consist of B tetrahedrons (green), B triangular planar faces (green), and P tetrahedrons (light violet). The blue tetrahedron represents Si dopant substituting the P tetrahedron. The green spheres represent Li atoms. The Li environments are illustrated below as well.

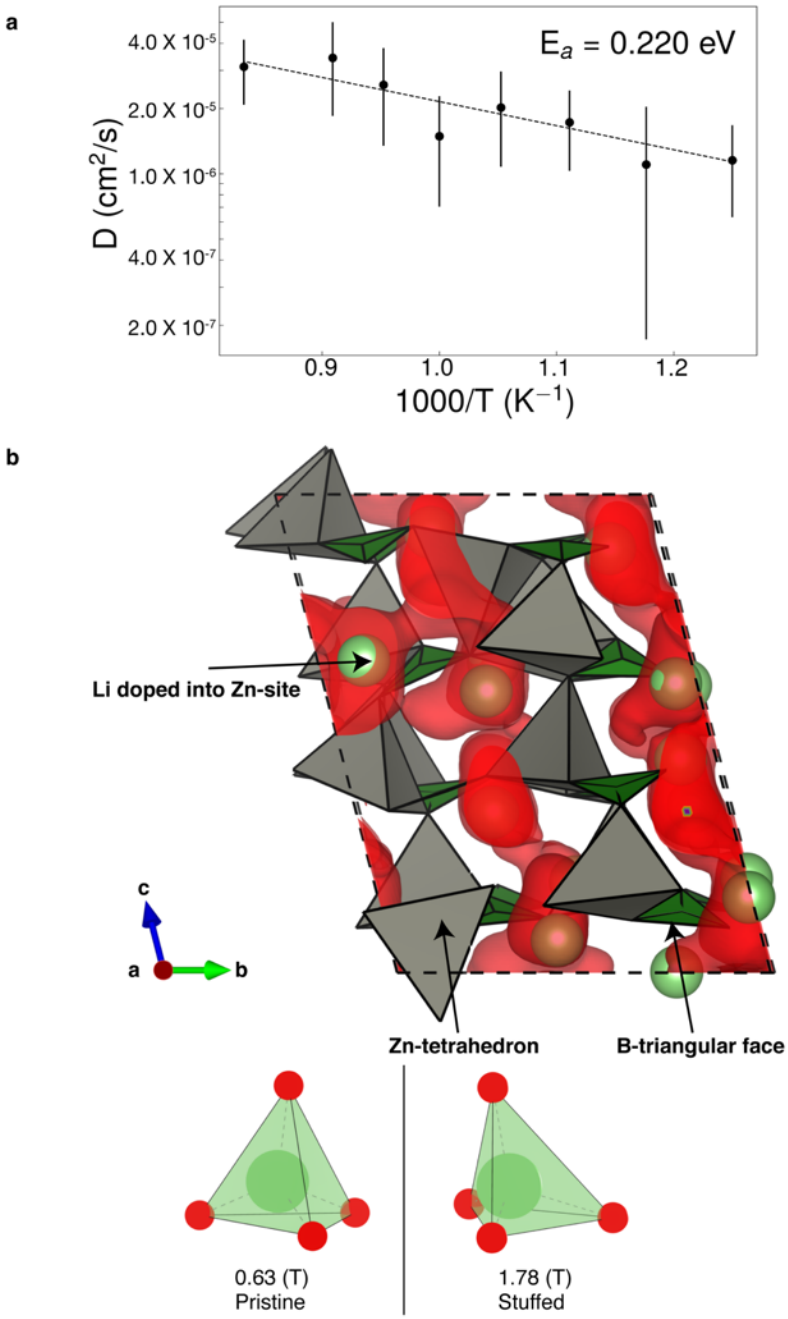


**Supplemental Figure 3.7 In-depth analysis of novel SIC $LiZnBO_3$.**
(a) Arrhenius plot of Li-ion diffusion coefficient showing an activation energy of 220 ± 101 meV. (b) Isosurface of Li-ion probability density from AIMD simulation at 1000 K. It shows the isosurface of $P = P_{max} / 500$ (red), where $P_{max}$ is the maximum value of the probability density. The CS frameworks in $LiZnBO_3$ consist of Zn tetrahedrons (green) and B triangular-planar faces (green). The green spheres represent Li atoms. The Li atom that is substituting a Zn tetrahedron is marked. The Li environments are illustrated below as well.

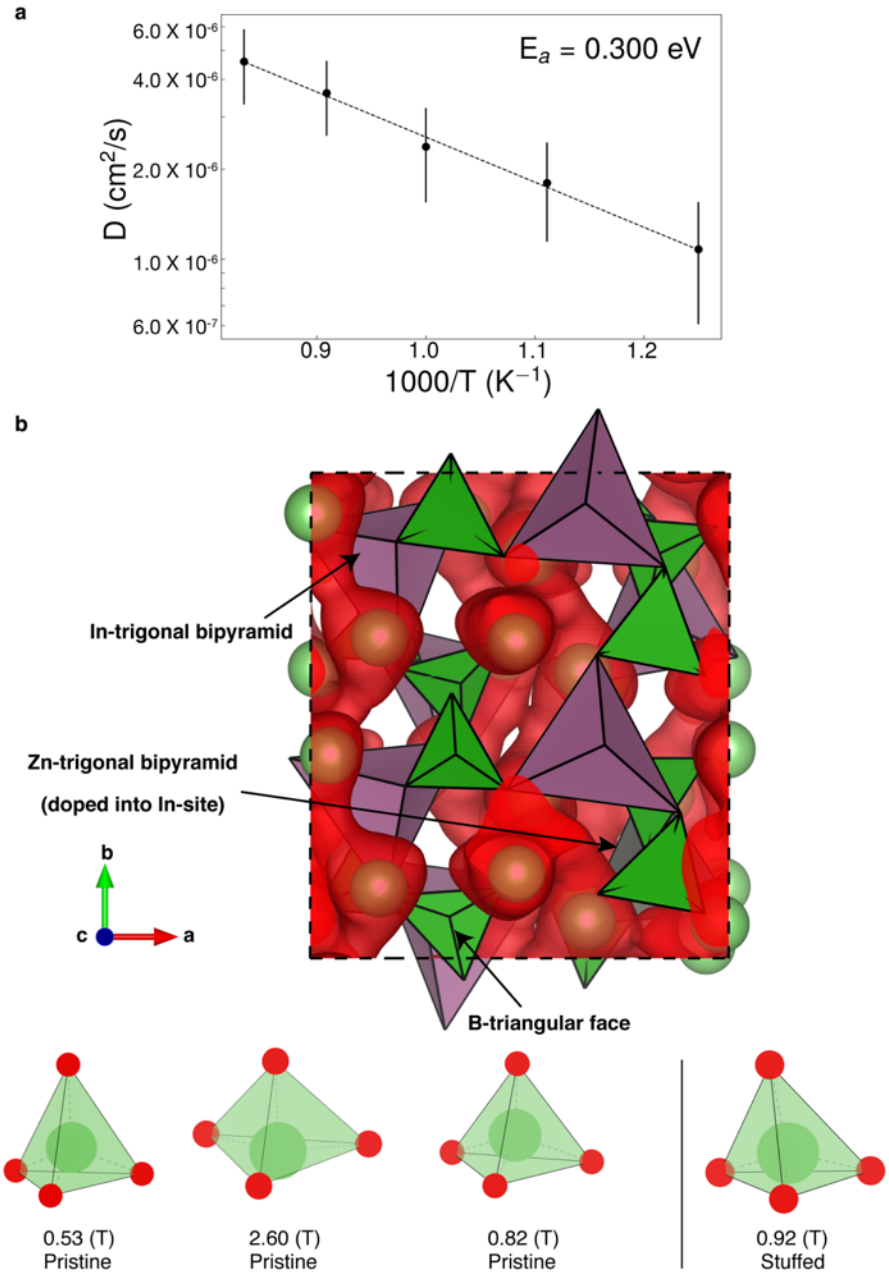


**Supplemental Figure 3.8 In-depth analysis of novel SIC $Li_3In(BO_3)_2$.**
(a) Arrhenius plot of Li-ion diffusion coefficient showing an activation energy of 300 ± 94 meV. (b) Isosurface of Li-ion probability density from AIMD simulation at 1000 K. It shows the isosurface of $P = P_{max} / 500$ (red), where $P_{max}$ is the maximum value of the probability density. The CS frameworks in $Li_3In(BO_3)_2$ consist of In trigonal bipyramids (violet) and B triangular-planar faces (green). The dark-grey trigonal bipyramid represents the Zn dopant substituting the P trigonal pyramid. The green spheres represent Li atoms. The Li environments are illustrated below as well.

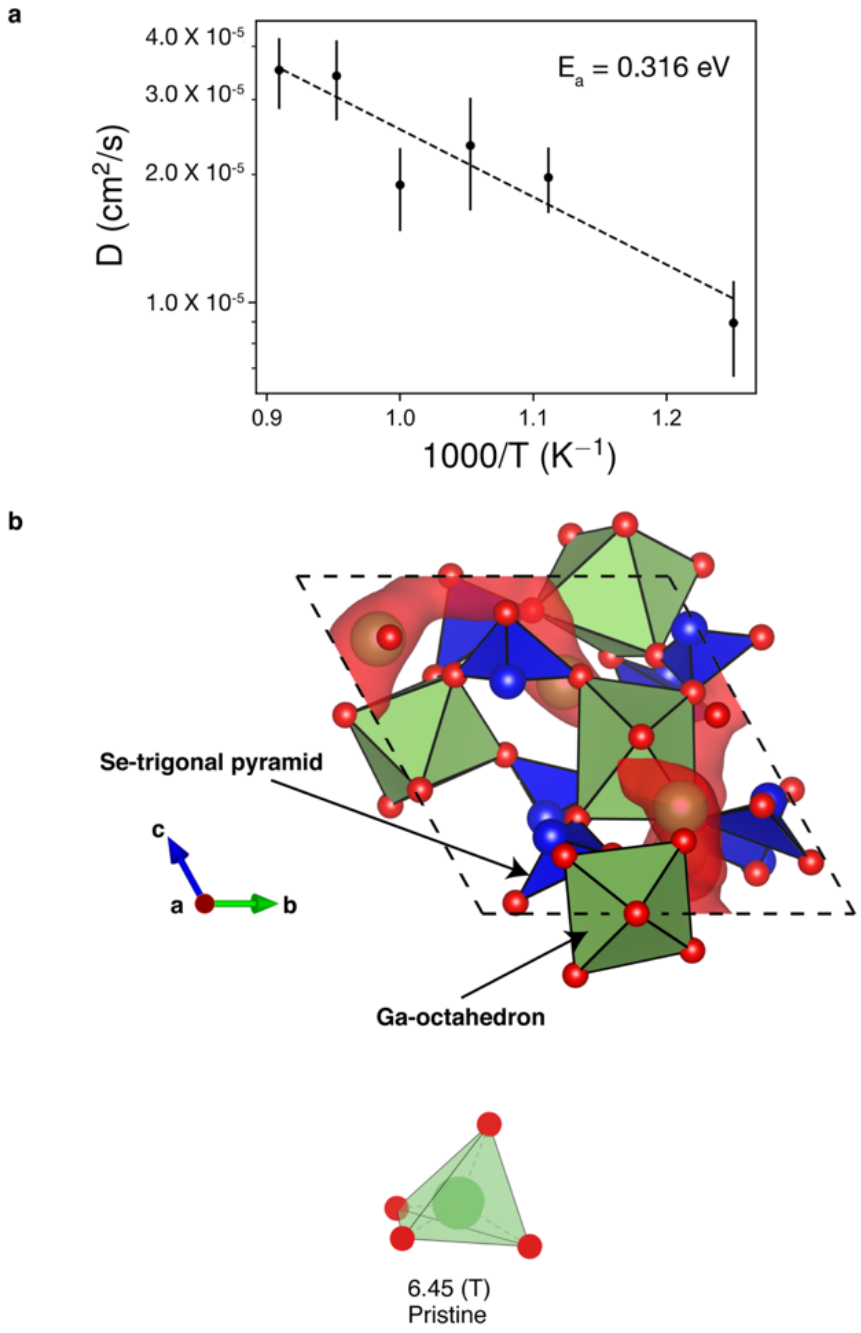


**Supplemental Figure 3.9 In-depth analysis of novel SIC $LiGa(SeO_3)_2$.**
(a) Arrhenius plot of Li-ion diffusion coefficient showing an activation energy of 320 ± 70 meV. (b) Isosurface of Li-ion probability density from AIMD simulation at 1000 K. It shows the isosurface of $P = P_{max} / 100$ (red), where $P_{max}$ is the maximum value of the probability density. The CS frameworks in $LiGa(SeO_3)_2$ consist of Se trigonal pyramids (blue) and Ga octahedrons (green). The green spheres represent Li atoms. The Li environment is illustrated below as well.

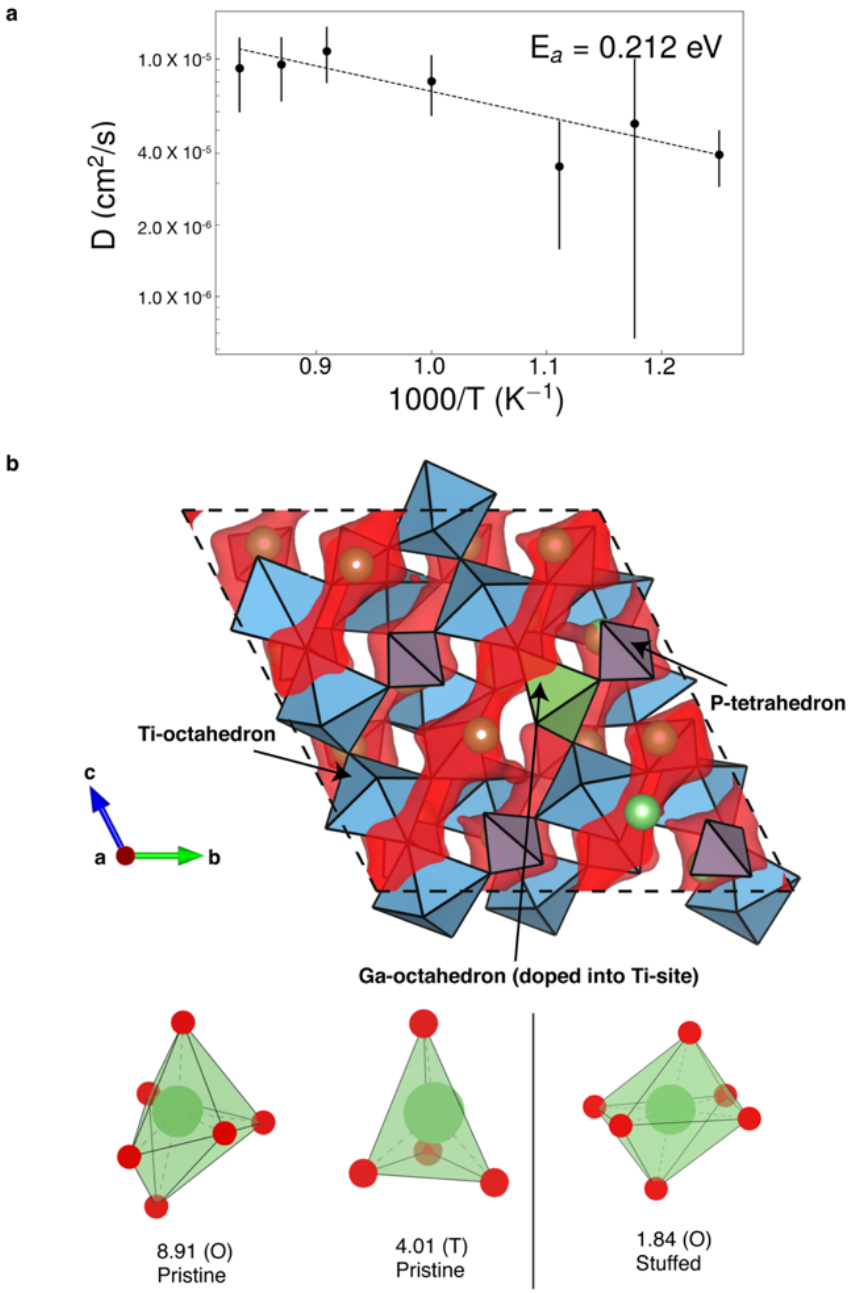


**Supplemental Figure 3.10 In-depth analysis of novel SIC $LiTiPO_5$.**
(a) Arrhenius plot of Li-ion diffusion coefficient showing an activation energy of 212 ± 71 meV. (b) Isosurface of Li-ion probability density from AIMD simulation at 1000 K. It shows the isosurface of $P = P_{max} / 100$ (red), where $P_{max}$ is the maximum value of the probability density. The CS frameworks in $LiTiPO_5$ consist of Ti octahedrons (light blue) and P tetrahedrons (light violet). The green octahedron represents Ga dopant substituting the Ti octahedron. The green spheres represent Li atoms. The Li environments are illustrated below as well.

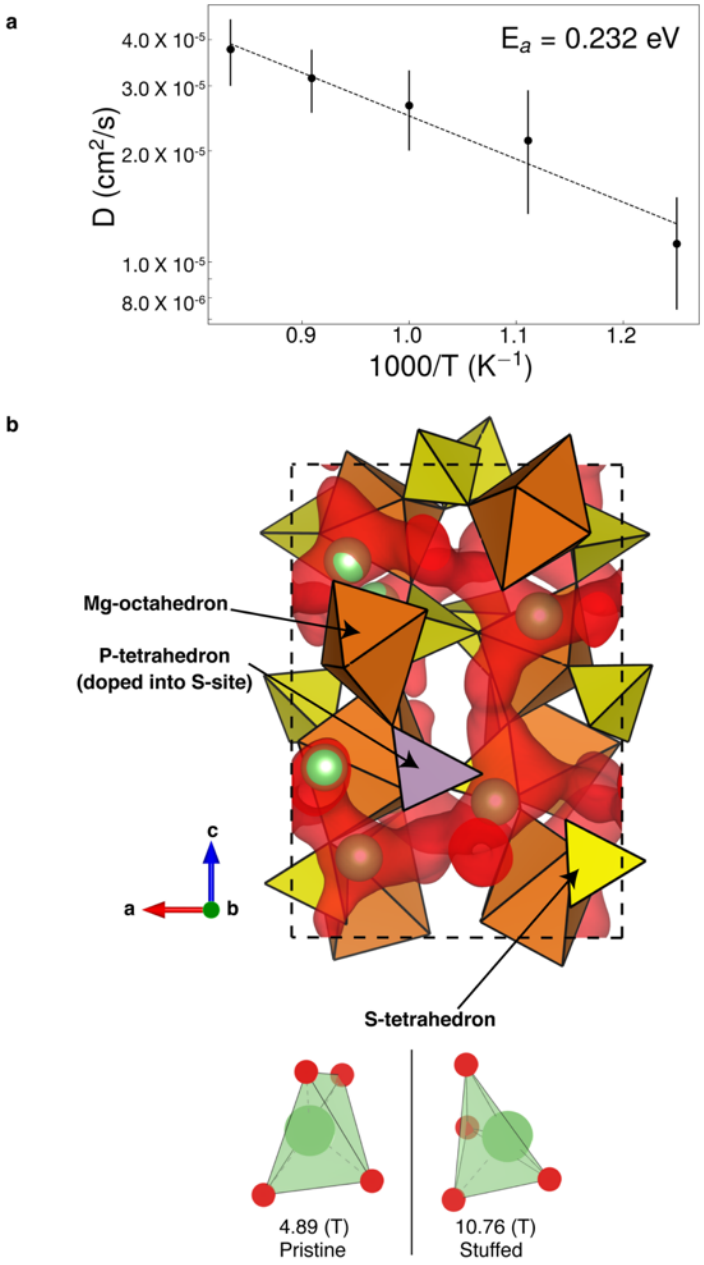


**Supplemental Figure 3.11 In-depth analysis of novel SIC $Li_2Mg_2(SO_4)_3$.**
(a) Arrhenius plot of Li-ion diffusion coefficient showing an activation energy of 232 ± 73 meV. (b) Isosurface of Li-ion probability density from AIMD simulation at 1000 K. It shows the isosurface of $P = P_{max} / 100$ (red), where $P_{max}$ is the maximum value of the probability density. The CS frameworks in $Li_2Mg_2(SO_4)_3$ consist of Mg octahedron (orange) and S tetrahedron (yellow). The light-violet tetrahedron represents P dopant substituting the S tetrahedron. The green spheres represent Li atoms. The Li environments are illustrated below as well.

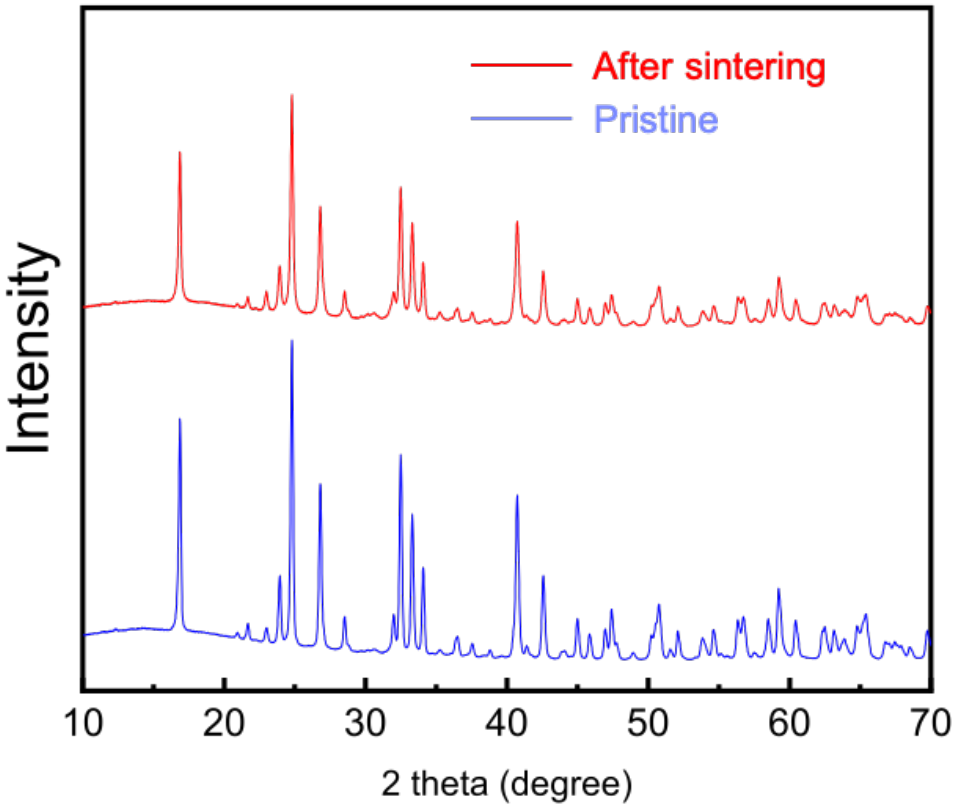


**Supplemental Figure 3.12 Comparing X-ray diffraction before and after spark plasma sintering.**
This shows that the main $LiGa(SeO_3)_2$ phase is well maintained after the densification via spark plasma sintering.

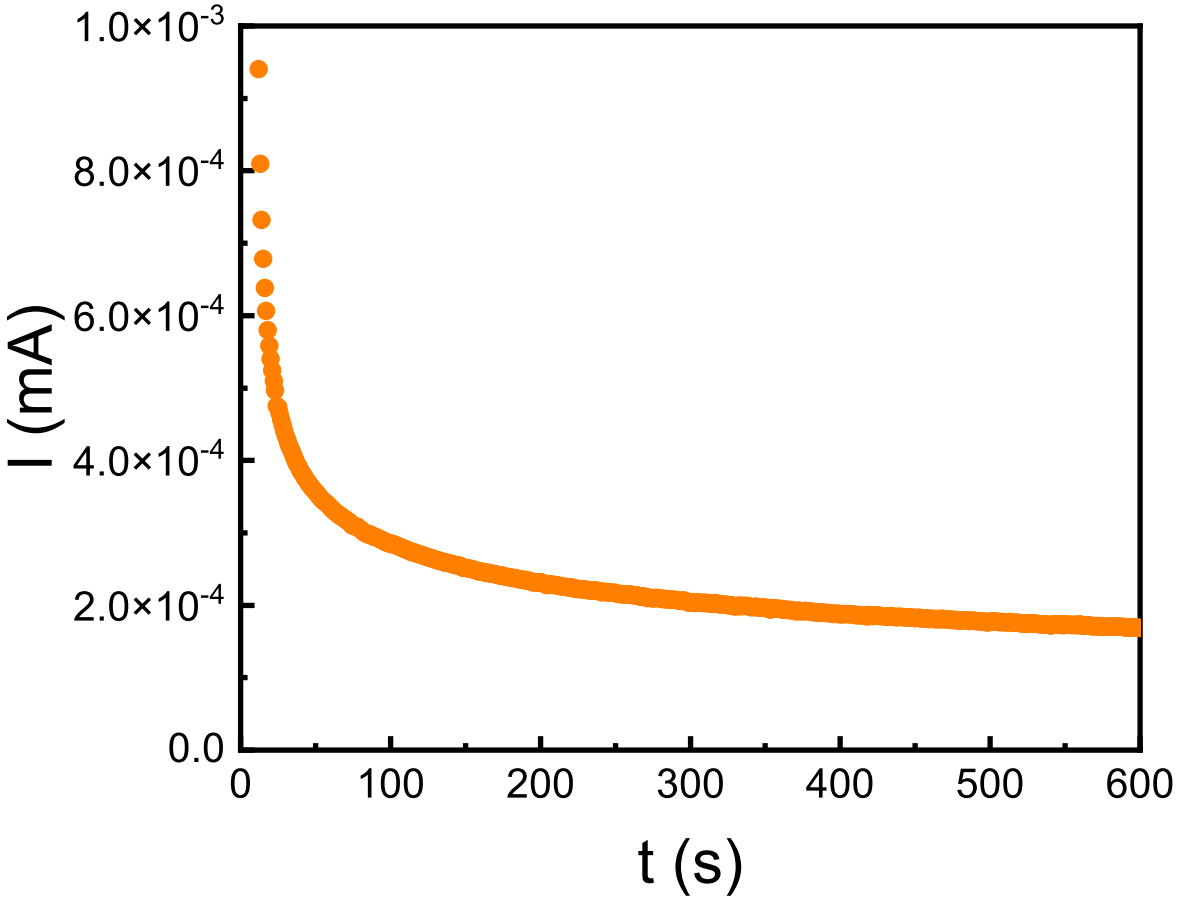


**Supplemental Figure 3.13 DC polarization test of In / $LiGa(SeO_3)_2$ / In cell.** 20 mV with respect to the open circuit voltage was applied to In/$LiGa(SeO_3)_2$/In cell. The electronic conductivity is $8 \times 10^{-7}$ S/cm.

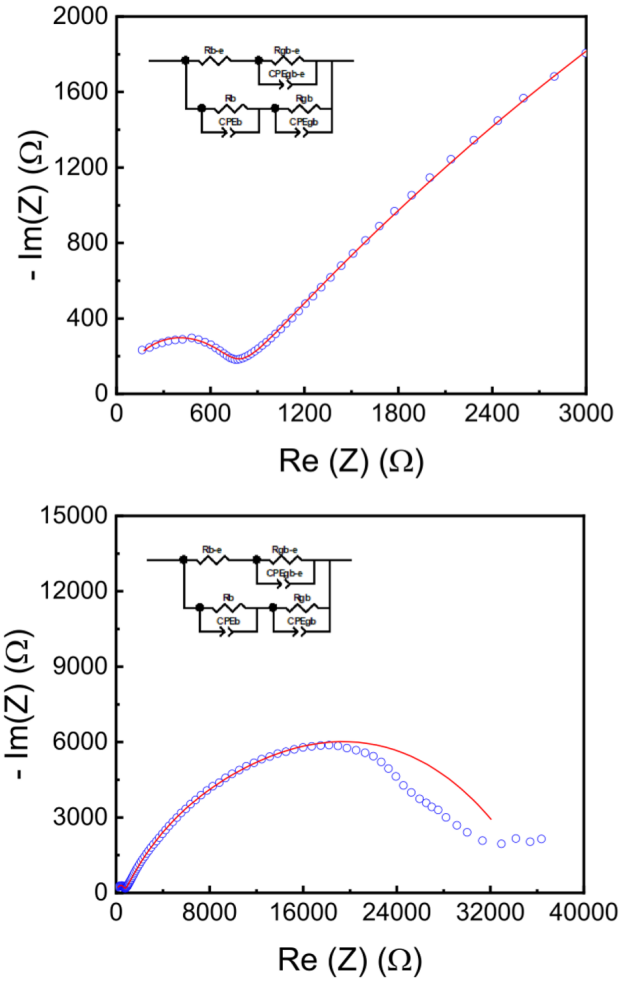


| | |
|---|---|
| $R_{b\text{-}e}$ | 23089 |
| $R_{gb\text{-}e}$ | 61818 |
| $CPE_{gb\text{-}e}$-T | $1.16\times10^{-5}$ |
| $CPE_{gb\text{-}e}$-P | 0.44116 |
| $R_b$ | 712.4 |
| $CPE_b$-P | $1.39\times10^{-9}$ |
| $CPE_b$-T | 0.83303 |
| $R_{gb}$ | 62462 |
| $CPE_{gb}$-P | $5.42\times10^{-6}$ |
| $CPE_{gb}$-T | 0.49503 |

**Supplemental Figure 3.14 Fitting EIS result of In/$LiGa(SeO_3)_2$/In cell with equivalent circuits.**

$R_{b\text{-}e}$: electronic resistance of bulk, $R_{gb\text{-}e}$: electronic resistance of grain boundary, $R_b$: ionic resistance of bulk, $R_{gb}$: ionic resistance of grain boundary. According to the fitting results, the pellet densified by spark plasma sintering still have a large grain-boundary resistance. It is due to that the pellet was sintered at a pretty low temperature. Since $LiGa(SeO_3)_2$ will decompose over 400 °C,[172] high temperature sintering is not applicable. Better performance is expected if the pellet is well-sintered.

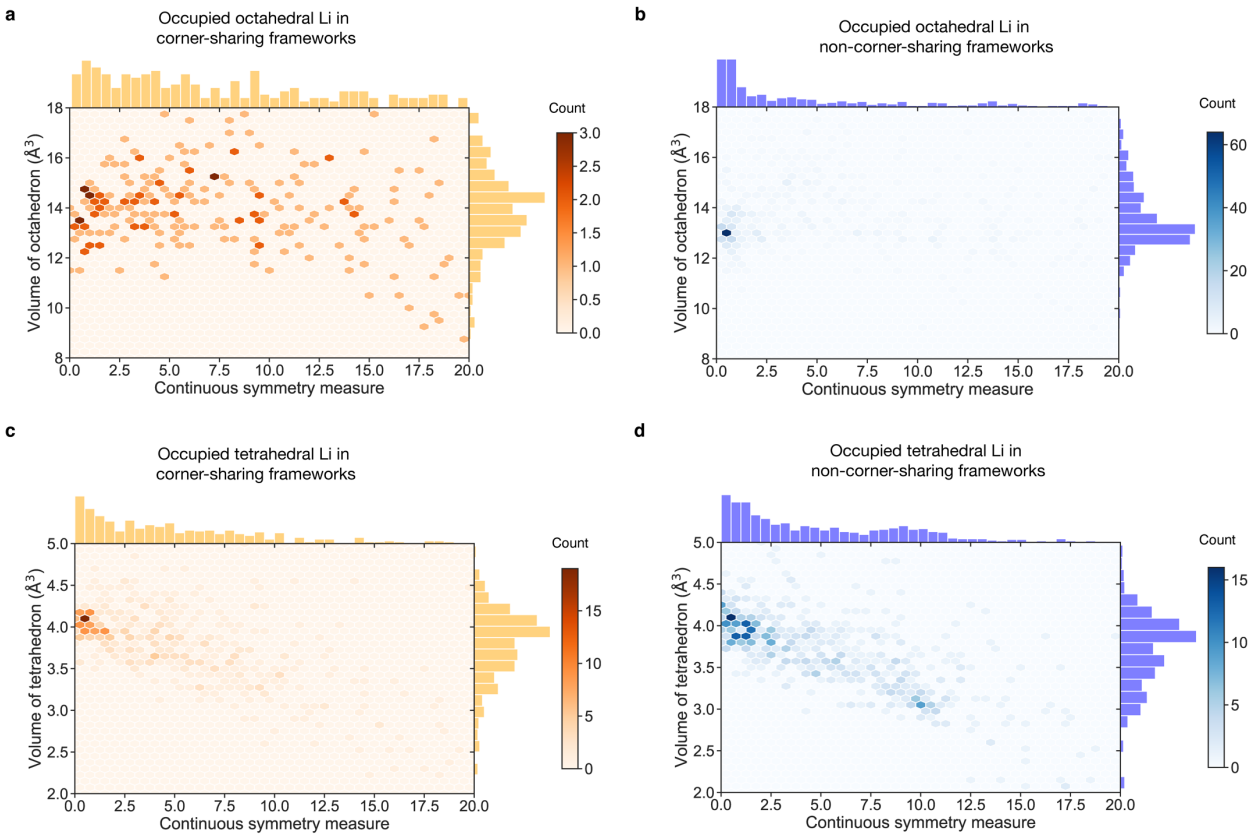


**Supplemental Figure 3.15 Comparison of the occupied lithium sites in CS and non-CS frameworks.**

The occupied octahedral lithium environment for CS (a) and non-CS frameworks (b), and the occupied tetrahedral lithium environment for CS (c) and non-CS frameworks (d). The color intensities indicate the number of entries that are populated in a given hexagon. Both the occupied tetrahedral and octahedral sites are more distorted in CS frameworks than in non-CS frameworks.

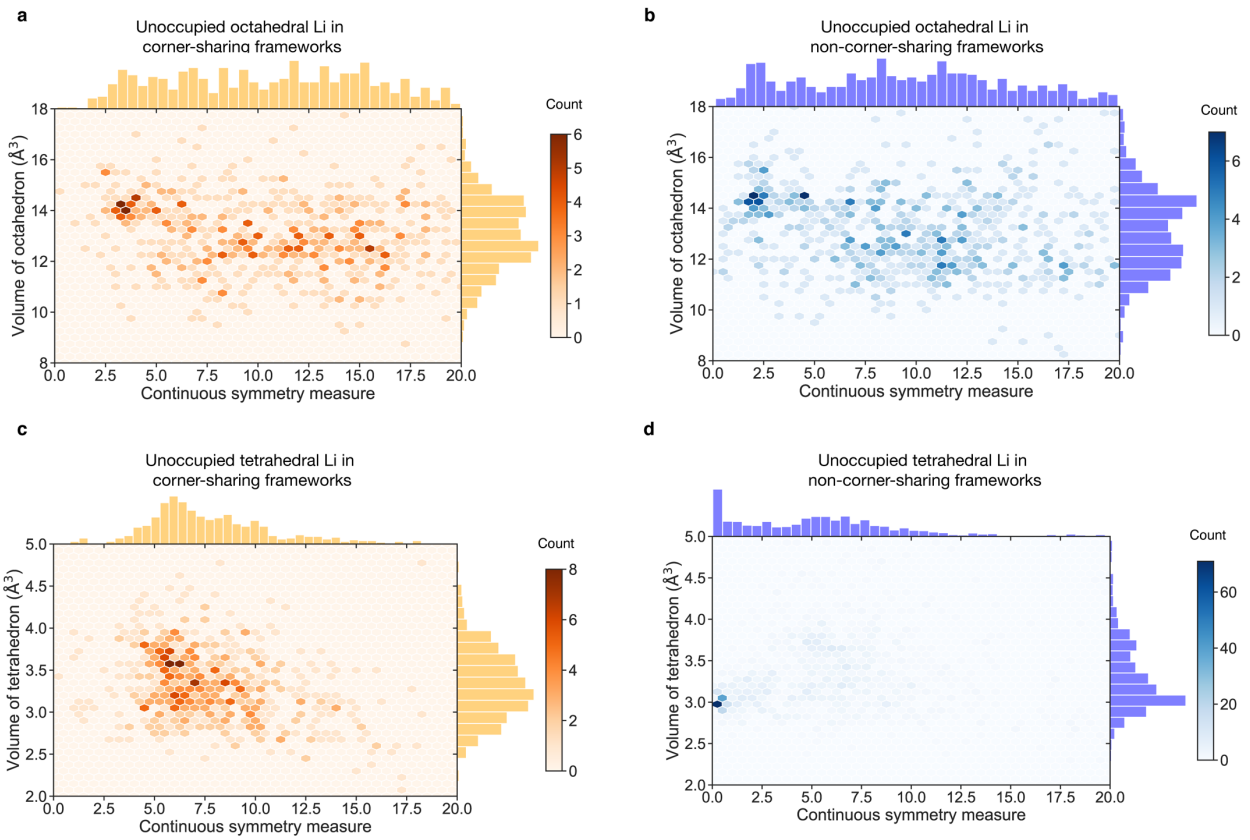


**Supplemental Figure 3.16 Comparison of unoccupied lithium sites in CS and non-CS frameworks.**

The unoccupied octahedral lithium environment for CS (a) and non-CS frameworks (b), and the unoccupied tetrahedral lithium environment for CS (c) and non-CS frameworks (d). The color intensities indicate the number of entries that are populated in a given hexagon. Both the unoccupied tetrahedral and octahedral sites are more distorted in CS frameworks than in non-CS frameworks.

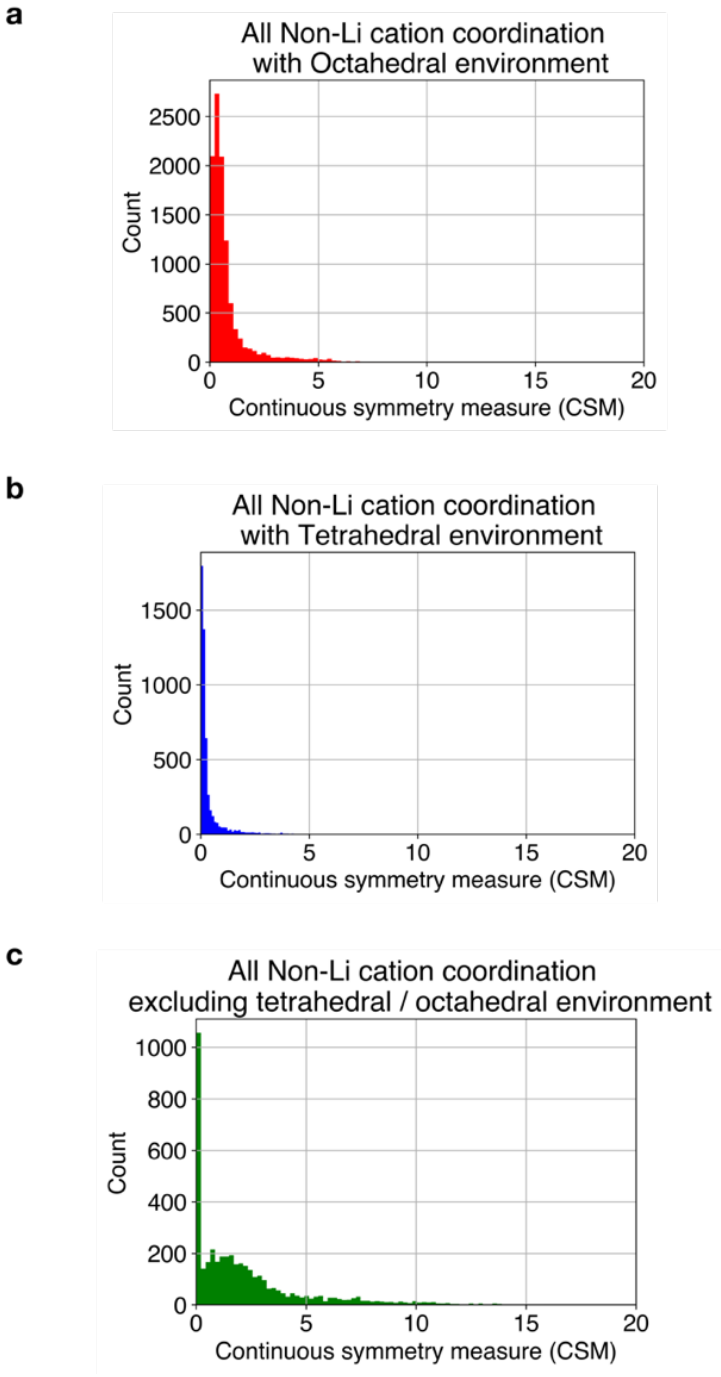


**Supplemental Figure 3.17 Analysis of CSM value of non-Li polyhedrons in quaternary Li oxides.**
The distribution of CSM values of non-Li cations in octahedral environment (a), in tetrahedral environment (b) and in coordination environment other than octahedral or tetrahedral environment (c). The non-Li-cation polyhedrons tend to be highly symmetric with their distribution peaking at a CSM value of 0. The non-Li cations of the 8,572 quaternary Li oxides in Figure 3.2 are analyzed here.

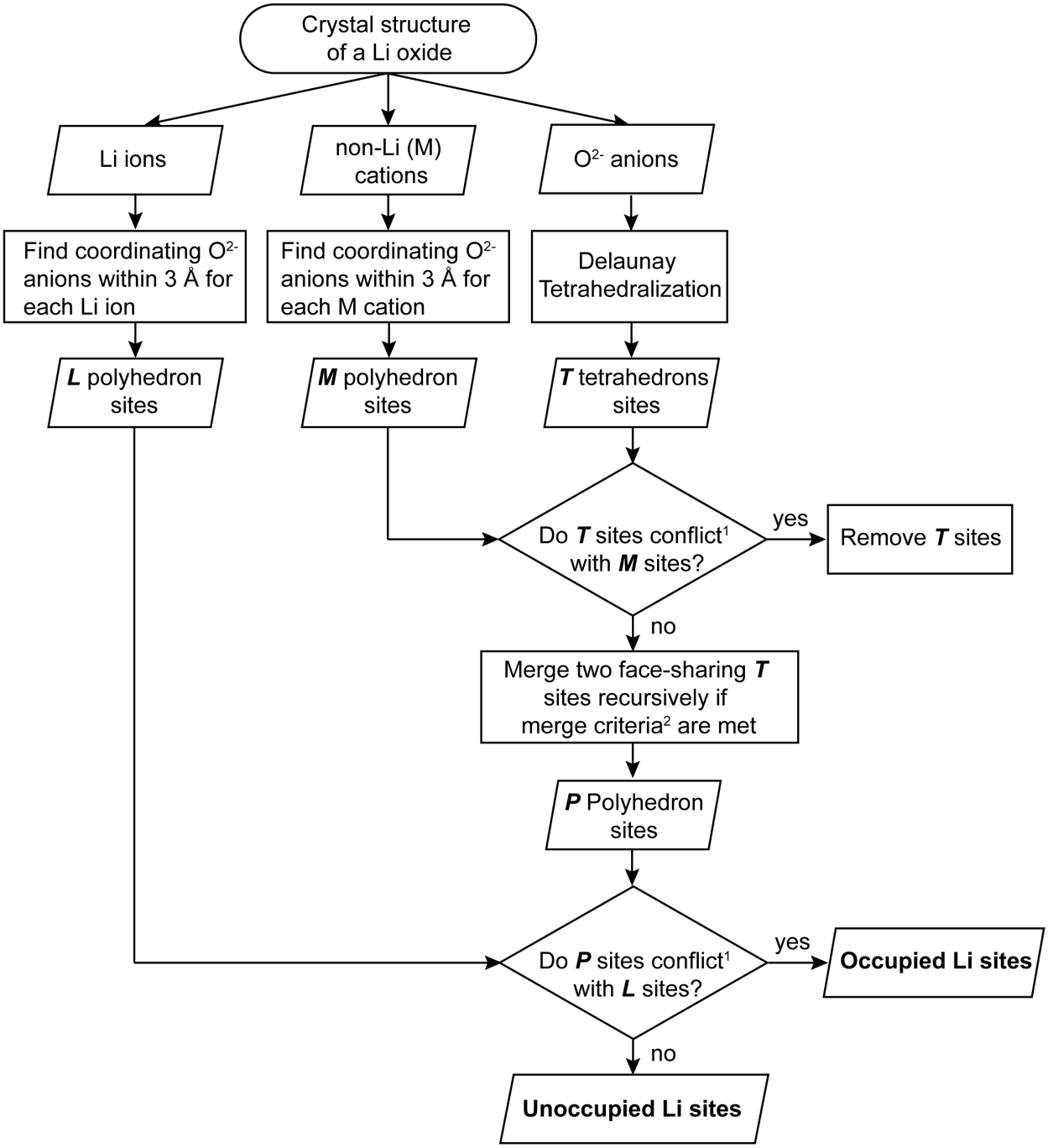


[1]Two sites are in "conflict" if their center distance ≤ 1 Å.
[2]Merge criteria for face-sharing ***T*** sites: 1) both sites are "distorted" with Robert/Roux factor ≤ 0.94, and 2) their center distance ≤ 1.1 Å.

**Supplemental Figure 3.18 Flowchart describing the algorithm to identify occupied and unoccupied Li sites in the crystal structure of a Li oxide compound.**

## Supplemental Table 3.1 Change of activation energy upon stuffing excess lithium in fast oxide Li-ion conductors.

| Type | Composition | Pristine $E_a$ (eV) | Stuffed Composition | Stuffed $E_a$ (eV) | Note | Reference |
|---|---|---|---|---|---|---|
| NASICON -type | $LiTi_2(PO_4)_3$ | 0.35 | $Li_{1.2}Al_{0.2}Ti_{1.8}(PO_4)_3$ | 0.28 | - | K. Arbi et. al.[162] |
| Garnet | $Li_3Nd_3Sb_2O_{12}$ | 1.34 | $Li_7La_3Zr_2O_{12}$ | 0.32 | 0.32 eV in LLZO is at 18–50 °C | M. O'Callaghan et. al.[188] M. O'Callaghan et. al.[189] R. Murugan et. al.[45] |
| LISICON-type | $Li_2ZnGeO_4$ ($\gamma$-$Li_3PO_4$ type) | Very low $\sigma_{Li}$ at elevated T | $Li_{3.5}Zn_{0.25}GeO_4$ (First reported LISICON) | 0.24 | 0.24 eV is at high temperature regime. | P. G. Bruce et. al.[190] H. Y-P. Hong[166] |
| | $Li_2ZnSiO_4$ (Monoclinic, $\gamma$-$Li_3PO_4$ type) | 0.88 | $Li_{3.55}(Ge_{0.45}Si_{0.1}V_{0.45})O_4$ | 0.37 | This compound has one of the highest $\sigma_{RT}$ of 0.058 mS/cm among LISICON frameworks | G. Zhao et. al.[191] |
| Ta-silicate | $LiTaSiO_5$ | 0.70 | $Li_{1.125}Ta_{0.875}Zr_{0.125}SiO_5$ | 0.25 | - | X. Xiong et. al.[165] Q. Wang et. al.[164] X. He et. al.[192] |
| Al-silicate | $LiAlSiO_4$ | 0.43 | $Li_{1.25}Al_{1.25}Si_{0.75}O_4$ | 0.28 | - | X. He et. al.[192] |

## Supplemental Table 3.2 Summary of the AIMD screening of 56 frameworks.

| Group Index | Materials Project ID | Composition | ICSD ID | $\sigma_{Pristine}$ at 1000 K (mS/cm) | $\sigma_{Stuffed}$ at 1000 K (mS/cm) | $\sigma_{Max}$ at 1000 K (mS/cm) | Higher conductivity (Pristine or Stuffed) | Classification |
|---|---|---|---|---|---|---|---|---|
| 1 | mp-1239225 | $Li_7SiPO_8$ | 238601 | 1804.1 | 1020.5 | 1804.1 | Pristine | Known SIC[193] |
| 2 | mp-1020018 | $Li_5B(SO_4)_4$ | 428002 | 1143.1 | 843.23 | 1143.1 | Pristine | Novel SIC |
| 3 | mp-14646 | $Li_2Mg_2(SO_4)_3$ | 65025 | 1047.6 | 798.43 | 1047.6 | Pristine | Novel SIC |
| 4 | mp-14399 | $LiAlSiO_4$ | 32595 | 239.25 | 987.08 | 987.08 | Stuffed | Known SIC[161,192] |
| 5 | mp-14488 | $Li_3In_2(PO_4)_3$ | 60948 | 928.40 | 675.88 | 928.40 | Pristine | Known SIC[161] |
| 6 | mp-18640 | $LiTi_2(PO_4)_3$ | 183669, 95979, 184088 | 1.8572 | 740.24 | 740.24 | Stuffed | Known SIC[65,162,194] |
| 7 | mp-560209 | $Li_9Al_3P_8O_{29}$ | 50957 | 1E-10 | 677.29 | 677.29 | Stuffed | Known SIC[161] |
| 8 | mp-1020106 | $LiB(SO_4)_2$ | 425174 | 1.9671 | 599.79 | 599.79 | Stuffed | Novel conductor with conductivity between 0.001 and 0.1 mS/cm |
| 9 | mp-552663 | $LiScAs_2O_7$ | 161499 | 0.049222 | 457.83 | 457.83 | Stuffed | Novel SIC |
| 10 | mp-1222486 | $Li_5Al(SiO_4)_2$ | 80593 | 0.23554 | 440.36 | 440.36 | Stuffed | High activation energy |
| 11 | mp-6097 | $Li_3Al(BO_3)_2$ | 6169, 54858, 51754, 20434, 51755 | 1.1641 | 397.16 | 397.16 | Stuffed | Known SIC[159] |
| 12 | mp-1020015 | $Li_2B_3PO_8$ | 192496 | 64.018 | 344.00 | 344.00 | Stuffed | Novel SIC |
| 13 | mp-1222367 | $LiLa(WO_4)_2$ | 184015 | 0.027841 | 290.66 | 290.66 | Stuffed | High E above the hull |
| 14 | mp-540083 | $LiMo(PO_4)_2$ | 81074 | 82.716 | 281.95 | 281.95 | Stuffed | Novel conductor with conductivity |

| | | | | | | | | |
|---|---|---|---|---|---|---|---|---|
| | | | | | | | | between 0.001 and 0.1 mS/cm |
| 15 | mp-18147 | $LiGaSiO_4$ | 65125 | 1E-10 | 281.25 | 281.25 | Stuffed | High activation energy |
| 16 | mp-1198930 | $LiGa(SeO_3)_2$ | 250868 | 278.20 | 170.79 | 278.20 | Pristine | Novel SIC |
| 17 | mp-6425 | $Li_3In_2(PO_4)_3$ | 62878, 62333 | 258.00 | 108.20 | 258.00 | Pristine | High activation energy |
| 18 | mp-10517 | $LiScP_2O_7$ | 91496 | 1E-10 | 239.75 | 239.75 | Stuffed | Known SIC[161] |
| 19 | mp-1020022 | $Li_3B(PO_4)_2$ | 248343 | 80.838 | 227.17 | 227.17 | Stuffed | Novel SIC |
| 20 | mp-973966 | $LiIn(IO_3)_4$ | 422056 | 219.61 | 145.94 | 219.61 | Pristine | Novel SIC |
| 21 | mp-13182 | $Li_2TiGeO_5$ | 250297 | 1E-10 | 214.94 | 214.94 | Stuffed | High activation energy |
| 22 | mp-565827 | $LiMoIO_6$ | 156006 | 1E-10 | 190.56 | 190.56 | Stuffed | High activation energy |
| 23 | mp-557756 | $Li_4Zn(PO_4)_2$ | 59640 | 1E-10 | 160.97 | 160.97 | Stuffed | High activation energy |
| 24 | mp-1222561 | $Li_5Ga(GeO_4)_2$ | 78513 | 5.0105 | 157.67 | 157.67 | Stuffed | High activation energy |
| 25 | mp-559441 | $LiTiPO_5$ | 39761 | 1E-10 | 137.34 | 137.34 | Stuffed | Novel SIC |
| 26 | mp-557104 | $LiAlB_2O_5$ | 51314 | 0.48977 | 134.29 | 134.29 | Stuffed | Novel conductor with conductivity between 0.001 and 0.1 mS/cm |
| 27 | mp-556799 | $Li_3In(BO_3)_2$ | 94355 | 1E-10 | 132.11 | 132.11 | Stuffed | Novel SIC |
| 28 | mp-560297 | $LiTaSiO_5$ | 39648 | 0.90127 | 125.22 | 125.22 | Stuffed | Known SIC[164,165] |
| 29 | mp-1222376 | $LiZnBO_3$ | 260590 | 1E-10 | 122.68 | 122.68 | Stuffed | Novel SIC |
| 30 | mp-557177 | $Li_2Al(BO_2)_5$ | 279578 | 23.980 | 103.75 | 103.75 | Stuffed | Novel conductor with conductivity between 0.001 and 0.1 mS/cm |
| 31 | mp-6456 | $LiNbGeO_5$ | 39464, 40536 | 0.22692 | 100.75 | 100.75 | Stuffed | Known SIC[161] |
| 32 | mp-556655 | $Li_2AlBO_4$ | 50612 | 0.20554 | 98.702 | 98.702 | Stuffed | |
| 33 | mp-559987 | $LiAl(PO_3)_4$ | 74860 | 2.2268 | 94.263 | 94.263 | Stuffed | |
| 34 | mp-557012 | $Li_3Sc(BO_3)_2$ | 241234, 261256 | 1E-10 | 64.284 | 64.284 | Stuffed | Known SIC[161] |
| 35 | mp-1020060 | LiB(S2O7)2 | 425175 | 1E-10 | 57.527 | 57.527 | Stuffed | |
| 36 | mp-558808 | $LiAl(SiO_3)_2$ | 98845 | 1E-10 | 52.607 | 52.607 | stuffed | |
| 37 | mp-556165 | $LiB(CO_2)_4$ | 281623 | 1E-10 | 42.884 | 42.884 | Stuffed | |
| 38 | mp-1198324 | $Li_2B_8SeO_{15}$ | 424079 | 2.1597 | 40.261 | 40.261 | Stuffed | |
| 39 | mp-8184 | $Li_2ZnGeO_4$ | 34362 | 0.072392 | 34.332 | 34.332 | Stuffed | |
| 40 | mp-16996 | $Li_3GaSiO_5$ | 72100 | 0.40620 | 25.918 | 25.918 | Stuffed | |
| 41 | mp-556544 | $LiAlSiO_4$ | 66137 | 16.288 | 12.776 | 16.288 | Pristine | |
| 42 | mp-652479 | $LiZnPO_4$ | 65764, 203174 | 1E-10 | 11.678 | 11.678 | Stuffed | |
| 43 | mp-1080241 | $Li_2Ge(S_2O_7)_3$ | 424358 | 1E-10 | 11.366 | 11.366 | Stuffed | |
| 44 | mp-567070 | $LiMoAsO_6$ | 59822 | 1E-10 | 9.4296 | 9.4296 | Stuffed | |
| 45 | mp-1222820 | $Li_2MgGeO_4$ | 8280, 166547 | 0.91052 | 1.3124 | 1.3124 | Stuffed | |
| 46 | mp-6782 | $Li_2ZrTeO_6$ | 71488, 202648, 71489 | 1E-10 | 0.71371 | 0.71371 | Stuffed | |
| 47 | mp-6442 | $LiAl(Si_2O_5)_2$ | 194284, 194287, 194288, 194285, | 1E-10 | 0.41688 | 0.41688 | Stuffed | |

| | | | | | | | | |
|---|---|---|---|---|---|---|---|---|
| | | | 194286, 100348, 31283, 174007 | | | | | |
| 48 | mp-559689 | $LiAlSiO_4$ | 97909 | 0.40797 | 1E-10 | 0.40797 | Pristine | |
| 49 | mp-8873 | $LiGeBO_4$ | 67535 | 0.40257 | 0.34091 | 0.40257 | Pristine | Known SIC[159] |
| 50 | mp-569027 | $LiMoAsO_6$ | 15035 | 0.34572 | 0.22482 | 0.34572 | Pristine | |
| 51 | mp-1222533 | $Li_4SiGe_3O_{10}$ | 26836 | 0.27519 | 1E-10 | 0.27519 | Pristine | |
| 52 | mp-556861 | $LiY(PO_3)_4$ | 162784 | 0.20802 | 0.13658 | 0.20802 | Pristine | |
| 53 | mp-556531 | $LiSi_2BO_6$ | 90849 | 5.1106E-10 | 3.5011E-10 | 5.1106E-10 | Pristine | |
| 54 | mp-1222571 | $LiAlSi_3O_8$ | 81980 | 2.4297E-10 | 3.3740E-10 | 3.3740E-10 | Stuffed | |
| 55 | mp-11189 | $Li_2MgSiO_4$ | 95972 | 2.5194E-10 | 3.2659E-10 | 3.2659E-10 | Stuffed | Known SIC[159] |
| 56 | mp-555743 | $LiZnPO_4$ | 50950 | 2.9732E-10 | 2.4053E-10 | 2.9732E-10 | Pristine | |

The 56 corner-sharing (CS) frameworks shown in Figure 3.3 are listed here. $\sigma_{Pristine}$ and $\sigma_{Stuffed}$ denote the conductivity of the Pristine and Stuffed structure from the 10-ps AIMD simulation at 1000 K, respectively. $\sigma_{Max}$ is the maximum value between the Pristine and Stuffed conductivity. The higher conductivity indicates whether the Pristine or Stuffed conductivity is larger. Each candidate is indexed by $\sigma_{Max}$ (group index). Candidates with $\sigma_{Max}$ exceeding 101.18 mS/cm (group index 1–30) were prioritized in designing superionic conductors. They are further classified as *known superionic conductors (SICs)*, *novel superionic conductors*, *novel conductors with conductivity between 0.001 and 0.1 mS/cm*, or others. Detailed information about these candidates is provided in Table 3.1 (novel superionic conductors), Supplemental Table 3.2 (known superionic conductors) and Supplemental Table 3.3 (others).

**Supplemental Table 3.3 CS frameworks previously reported to show Li-ion conductivity above 0.1 mS/cm at room temperature.**

The group index (corresponding to Supplemental Table 3.1), pristine composition of the CS framework, specific composition reported to exhibit superionic conductivity, Li-ion conductivity at 300 K ($\sigma_{300\ K}$), activation energy ($E_a$), and the method for measuring the ionic conductivity are summarized.

| Materials Project ID | Group Index | Pristine composition | Composition exhibiting superionic conductivity | $\sigma_{300\ K}$ (mS/cm) | $E_a$ (eV) | Method and Reference | Notes |
|---|---|---|---|---|---|---|---|
| mp-1239225 | 1 | $Li_7SiPO_8$ | $Li_4Al_{1/3}Si_{1/6}Ge_{1/6}P_{1/3}O_4$ | 0.9 | 0.28 | Classical MD | $\gamma$-$Li_3PO_4$ solid solution similar to LISICON-type Experimental $\sigma_{300\ K}$ in this framework span up to 0.058 mS/cm. |
| mp-14399 | 4 | $LiAlSiO_4$ | $Li_{1.25}Al_{1.25}Si_{0.75}O_4$ | 1.3 | 0.28 | AIMD | - |
| mp-14488 | 5 | $Li_3In_2(PO_4)_3$ | $Li_{3.5}In_2P_{2.5}Ge_{0.5}O_{12}$ | 1.4 | 0.26 | AIMD | - |
| mp-18640 | 6 | $LiTi_2(PO_4)_3$ | $Li_{1.3}Al_{0.3}Ti_{1.7}(PO_4)_3$ | 3.0 | 0.2~ 0.35 | Impedance spectroscopy | NASICON-type superionic conductors |
| mp-560058 | 7 | $Li_9Ga_3P_8O_{29}$ | $Li_{9.5}Ga_3Ge_{0.5}P_{7.5}O_{29}$ | 0.12 | 0.33 | AIMD | - |
| mp-6097 | 11 | $Li_3Al(BO_3)_2$ | $Li_{2.5}Al(B_{0.75}C_{0.25}O_3)_2$ | 0.36 | 0.26 | AIMD | - |
| mp-10517 | 18 | $LiScP_2O_7$ | $Li_{1.33}ScSi_{0.33}P_{1.67}O_7$ | 0.17 | 0.28 | AIMD | - |
| mp-5602979 | 28 | $LiTaSiO_5$ | $Li_{1.25}Ta_{0.75}Zr_{0.25}Si_5$ | 6.1 | 0.21 | AIMD | - |
| mp-6456 | 31 | $LiNbGeO_5$ | $Li_{1.25}Nb_{0.75}Sn_{0.25}GeO_5$ | 0.24 | 0.30 | AIMD | - |
| mp-557012 | 34 | $Li_3Sc(BO_3)_2$ | $Li_{3.375}Mg_{0.375}Sc_{0.625}(BO_3)_2$ | 0.10 | 0.37 | AIMD | - |
| mp-8874 | 49 | $LiSiBO_4$ | $Li_{1.375}SiB_{0.875}O_4$ | 0.31 | 0.31 | AIMD | - |
| mp-17288 | 55 | $Li_2ZnSiO_4$ | $Li_{2.5}Zn_{0.75}SiO_4$ | 3.1 | 0.20 | AIMD | 10-ps AIMD was performed for mp-11189, which belongs to the same framework group. |
| - | - | $LiTa_2PO_8$ | $LiTa_2PO_8$ | 1.6 | 0.32 | Impedance spectroscopy | This compound is a novel crystal structure with CS framework that was first discovered in 2018 and is not listed in Materials Project or the ICSD database. |

**Supplemental Table 3.4 CS frameworks showing Li-ion conductivity below 0.1 mS/cm.**

CS frameworks that were not able to be designed as a superionic conductor are listed. The group index (corresponding to Supplemental Table 3.1), composition of the CS framework, Li-ion conductivity at 300 K ($\sigma_{300\,K}$), activation energy ($E_a$), and details of each candidate are summarized. Some candidates with extrapolated conductivity between 0.001 and 0.1 mS/cm are highlighted in green for potential enhancement of ionic conductivity by introducing higher concentration of dopants.

| Group Index | Materials Project ID | Composition | $\sigma_{300\,K}$ (mS/cm) | $E_a$ (eV) | Summary | Notes |
|---|---|---|---|---|---|---|
| 8 | mp-1020106 | $LiB(SO_4)_2$ | 0.00672 (1.620E-5, 2.79) | 0.412 ± 0.150 | Novel conductor with conductivity between 0.001 and 0.1 mS/cm | P is doped into S tetrahedron. 100-ps AIMD simulations at 8 temperatures were performed. |
| 10 | mp-1222486 | $Li_5Al(SiO_4)_2$ | Too low to be estimated | 1.062 ± 0.431 | High activation energy | Al is doped into Si tetrahedron. 35-ps AIMD simulations at 5 temperatures were performed. |
| 13 | mp-1222367 | $LiLa(WO_4)_2$ | - | - | High E above the hull | The pristine compound has high energy above the hull of 0.070 eV/atom. This is an ordered structure of a known compound (ICSD-184015) that has Li and La partial occupancies. |
| 14 | mp-540083 | $LiMo(PO_4)_2$ | 0.0389 (2.03E-4, 7.46) | 0.362 ± 0.131 | Novel conductor with conductivity between 0.001 and 0.1 mS/cm | Ta is doped into Mo octahedron. 100-ps AIMD simulations at 6 temperatures were performed. |
| 15 | mp-18147 | $LiGaSiO_4$ | 0.000982 (5.28E-9, 182) | 0.442 ± 0.302 | High activation energy | Al is doped into Si tetrahedron. 140-ps AIMD simulations at 5 temperatures were performed. |
| 17 | mp-6425 | $Li_3In_2(PO_4)_3$ | Too low to be estimated | 0.596 ± 0.199 | High activation energy | Pristine compound. 40-ps AIMD simulations at 5 temperatures were performed. |
| 21 | mp-13182 | $Li_2TiGeO_5$ | 0.00115 (2.12E-8, 62.0) | 0.467 ± 0.271 | High activation energy | Al is doped into Ge tetrahedron. 35-ps AIMD simulations at 5 temperatures were performed. |
| 22 | mp-565827 | $LiMoIO_6$ | 0.000183 (1.87E-9, 17.9) | 0.530 ± 0.287 | High activation energy | Ga is doped into Mo octahedron. 70-ps AIMD simulations at 5 temperatures were performed. |
| 23 | mp-557756 | $Li_4Zn(PO_4)_2$ | Too low to be estimated | 0.841 ± 0.331 | High activation energy | Li is doped into Zn tetrahedron. 50-ps AIMD simulations at 5 temperatures were performed. |
| 24 | mp-1222561 | $Li_5Ga(GeO_4)_2$ | Too low to be estimated | 0.556 ± 0.688 | High activation energy | Al is doped into Ge tetrahedron. 30-ps AIMD simulations at 5 temperatures were performed. |
| 26 | mp-557104 | $LiAlB_2O_5$ | 0.00494 (5.51E-6, 4.42) | 0.392 ± 0.169 | Novel conductor with conductivity between 0.001 and 0.1 mS/cm | Mg is doped into B tetrahedron. 500-ps AIMD simulations at 7 temperatures were performed. |
| 30 | mp-557177 | $Li_2Al(BO_2)_5$ | 0.0329 (7.88E-4, 1.37) | 0.340 ± 0.093 | Novel conductor with conductivity between 0.001 and 0.1 mS/cm | Zn is doped into B tetrahedron. 550-ps AIMD simulations at 7 temperatures were performed. |

**Supplemental Table 3.5 Comparison of quartile values of CSM between CS and non-CS frameworks.**
Q1, Q2 and Q3 values are provided for CSM values of CS and non-CS frameworks for both octahedral and tetrahedral environment. The row *Both occupied and unoccupied* corresponds to Figure 3.6. The rows *Only occupied* and *only unoccupied* correspond to Supplemental Figure 3.12-3.13.

| | Environment | Percentile | CSM of CS | CSM of non-CS |
|---|---|---|---|---|
| **Both Occupied and Unoccupied** | Octahedral | 25 (Q1) | 6.35 | 3.50 |
| | | 50 (Q2) | 11.06 | 8.83 |
| | | 75 (Q3) | 14.80 | 13.61 |
| | Tetrahedral | 25 (Q1) | 5.43 | 2.20 |
| | | 50 (Q2) | 7.09 | 5.13 |
| | | 75 (Q3) | 9.47 | 7.62 |
| **Only Occupied** | Octahedral | 25 (Q1) | 3.21 | 0.72 |
| | | 50 (Q2) | 7.37 | 3.43 |
| | | 75 (Q3) | 14.39 | 10.91 |
| | Tetrahedral | 25 (Q1) | 1.52 | 1.46 |
| | | 50 (Q2) | 4.61 | 4.62 |
| | | 75 (Q3) | 8.82 | 9.69 |
| **Only Unoccupied** | Octahedral | 25 (Q1) | 6.58 | 6.04 |
| | | 50 (Q2) | 11.21 | 10.31 |
| | | 75 (Q3) | 15.06 | 14.82 |
| | Tetrahedral | 25 (Q1) | 5.73 | 2.00 |
| | | 50 (Q2) | 7.19 | 5.28 |
| | | 75 (Q3) | 9.56 | 7.76 |

## Supplemental Note 3.1.
### Details on the high-throughput screening

Here, we provide additional notes regarding the high-throughput screening that is summarized as Step1-6 in Figure 3.2. In Step 1, we start with quaternary lithium oxides that do not contain anions other than $O^{2-}$ (e.g. $F^{-}$, $Cl^{-}$, $Br^{-}$, $S^{2-}$, or $N^{3-}$). We focus on quaternary systems that include two non-Li cation elements as it typically takes two or more distinct polyhedrons to generate diverse CS frameworks. In Step 2, we group entries based on the framework. Previous studies which tried various chemistries on LGPS, LLZO, and LATP frameworks indicate that the tendency to show superionic conductivity does not drastically change as long as the framework is maintained. In Step 4, we exclude compounds with redox-active elements (V, Cr, Mn, Fe, Co, Ni, Cu), hydrogen, or other hazardous, radioactive, or rare elements. In Step 5, we selectively study the frameworks which have been experimentally reported. In this step, there may exist multiple hypothetical materials which can activate fast lithium diffusion as well.

## Supplemental Note 3.2.
### Continuous symmetry measure of tetrahedrons and octahedrons

Continuous symmetry measure (CSM) is a metric to measure on a continuous scale from 0 to 100 the deviation from a perfect polyhedron geometry.[174] This quantity is defined through the following equation (3.4):

$$\mathrm{CSM} = \min \frac{\sum_{k=1}^{N} |Q_k - P_k|^2}{\sum_{k=1}^{N} |Q_k - Q_0|^2} \tag{3.4}$$

Where given a structure composed of N vertexes, their coordinates given by the vectors $\{Q_k, k = 1, 2,\ldots,N\}$ and $Q_0$ being the average coordination vector:

$$Q_0 = \frac{1}{N} \sum_{k=1}^{N} Q_k \tag{3.5}$$

We search for the vertex coordinates $\{P_k, k = 1, 2,\ldots,N\}$ of the nearest perfectly symmetric object. The CSM can be understood as the minimal cumulative distance that the vertexes of the given structure must undergo to attain the perfect geometry. CSM is independent of the position, orientation, and size of the given structure and therefore provides a general metric to evaluate the symmetry of any shape with respect to any perfectly symmetric geometry. A polyhedron with a perfect symmetry has a CSM value of 0. The CSM value increases as the distortion becomes larger.

The maximum value of CSM is 100. However, depending on the symmetry of the target polyhedron, there is a geometry-specific maximum value below 100. For an octahedron, the maximum value of CSM is 66.7 which occurs with infinite elongation of a perfect octahedron along the z-axis, as suggested by Pinsky and Avnir1 . Similarly, for a tetrahedron, the maximum value of CSM is 66.7 when a regular tetrahedron is elongated infinitely along the z-axis.

## Supplemental Note 3.3.
### Assignment of coordination environment

As described in the Methodology section, the coordination environment analysis measures the deviation of a lithium environment from a perfect tetrahedral and octahedral environment similar to a previous study.[173] Therefore, a high CSM value of a certain environment can indicate that the tetrahedral or octahedral site is extremely distorted or that the environment can be better matched to other coordination environments. We set our target environment as tetrahedral and octahedral sites first because as higher degree of distortion appears, the assignment of the coordination environment becomes ambiguous. In addition, a previous study[195] on the Li environment of oxides in the Materials Project database[168] showed that approximately 70% of Li sites are tetrahedral or octahedral sites and the remaining sites are classified as seesaw, trigonal bipyramid, square pyramid, or other sites. These statistics indicate that the lithium atom most prefers to occupy tetrahedral or octahedral sites in oxides, and therefore, the deviation of a given environment from a perfect tetrahedron, or octahedron was computed in this study. The analysis indicates that regular tetrahedral and octahedral sites are much less frequently provided in CS frameworks.

## Supplemental Note 3.4.

### Comparing the diffusional data of CS and non-CS polymorphs of the same composition

To compare the actual Li-ion diffusion in CS frameworks with non-CS frameworks, we investigated two set of representative polymorphs in the Materials Project database. These two compositions all have polymorphs with CS and non-CS frameworks, allowing us to compare the effect of framework connectivity on Li-ion diffusion while excluding the effect of chemistries and Li-ion concentrations. We have performed fully converged AIMD simulations to compare the difference of diffusional properties in these materials. By following the same method of finding novel conductors in this work, in each structure, we have investigated both Pristine and Stuffed composition, and chose the more conducting composition to represent that specific structure.

Supplemental Table 3.6 tabulates the results from AIMD simulations, and Supplemental Figure 3.19-3.20 show the Arrhenius plot and Li-ion probability density. We find that in all of the cases, Li-ion diffusion is significantly faster in the polymorph with CS frameworks compared to non-CS frameworks. For example, in non-CS $LiSbP_2O_7$ (mp-684090), lithium ions cannot percolate through the structure and are blocked by the framework cation polyhedrons as can be seen from the Li-ion probability density analysis (Supplemental Figure 3.20a) and the mean-squared displacement during 250 ps (Figure 3.19a). On the other hand, CS $LiSbP_2O_7$ (mp-26341), which has the same framework as $LiScP_2O_7$ reported by He et. al[161], is again found to be a fast ionic conductor.

Similarly, CS $LiNbWO_6$ shows two orders of magnitude higher Li-ion conductivity at RT compared to non-CS $LiNbWO_6$ even if we attempt Li-stuffing on the more sluggish non-CS $LiNbWO_6$. Supplemental Figure 20b shows that while the CS $LiNbWO_6$ shows favorable 3-dimensional diffusion, the non-CS is a 2-dimensional conductor due to the edge-sharing Nb- and W-polyhedrons blocking the third dimension.

**Supplemental Table 3.6 Summary of the comparison of diffusional data between CS and non-CS polymorphs**

| Composition | CS MPID | Pristine or Stuffed | $\sigma_{300\,K}$ (mS/cm) | $E_a$ (eV) | non-CS MPID | Pristine or Stuffed | $\sigma_{300\,K}$ (mS/cm) | $E_a$ (eV) |
|---|---|---|---|---|---|---|---|---|
| $LiSbP_2O_7$ | mp-26341 | Stuffed | 0.201 (0.0097, 4.18) | 0.278 (0.203, 0.353) | mp-684090 | Stuffed | Non-diffusive | Non-diffusive |
| $LiNbWO_6$ | mp-1222548 | Pristine | 16.5 (2.34, 115) | 0.188 (0.139, 0.236) | mp-619802 | Stuffed | 0.170 (0.00440, 6.56) | 0.311 (0.220, 0.401) |

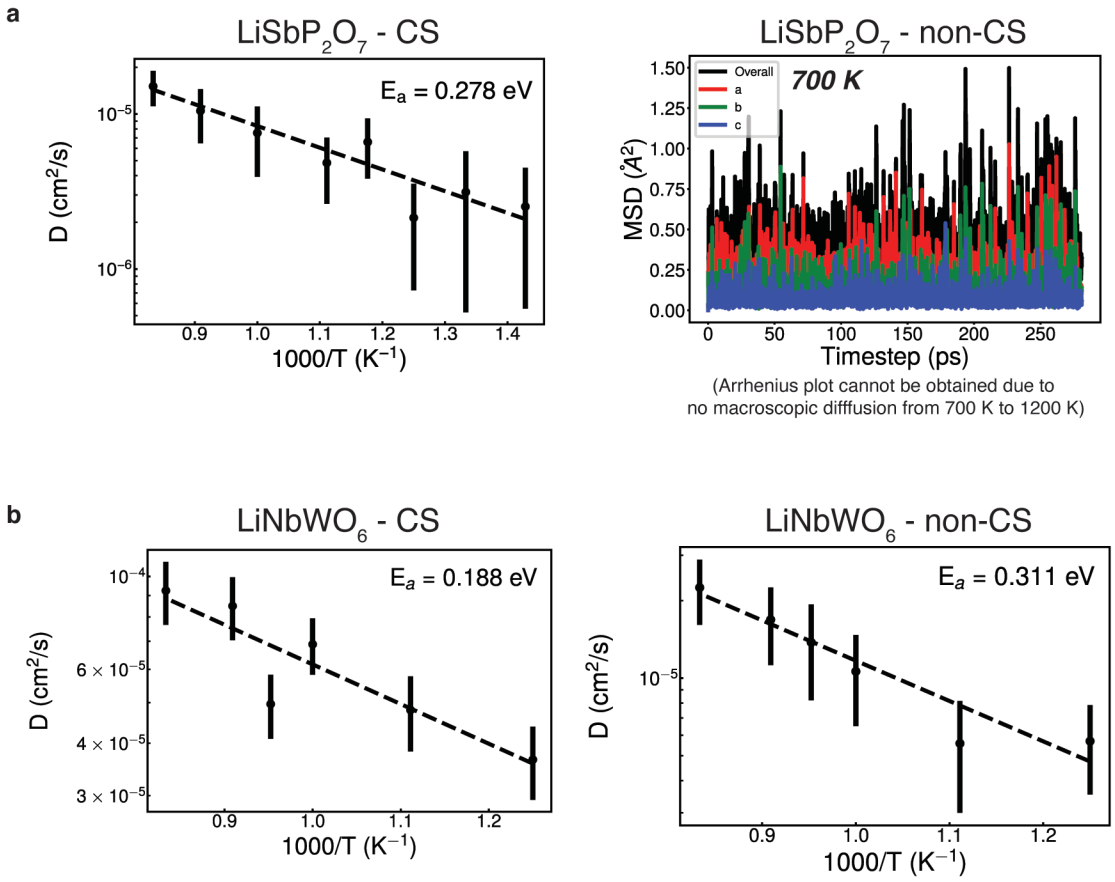


**Supplemental Figure 3.19 Comparing the Arrhenius plot of CS and non-CS polymorphs for $LiSbP_2O_7$ (a) and $LiNbWO_6$.**

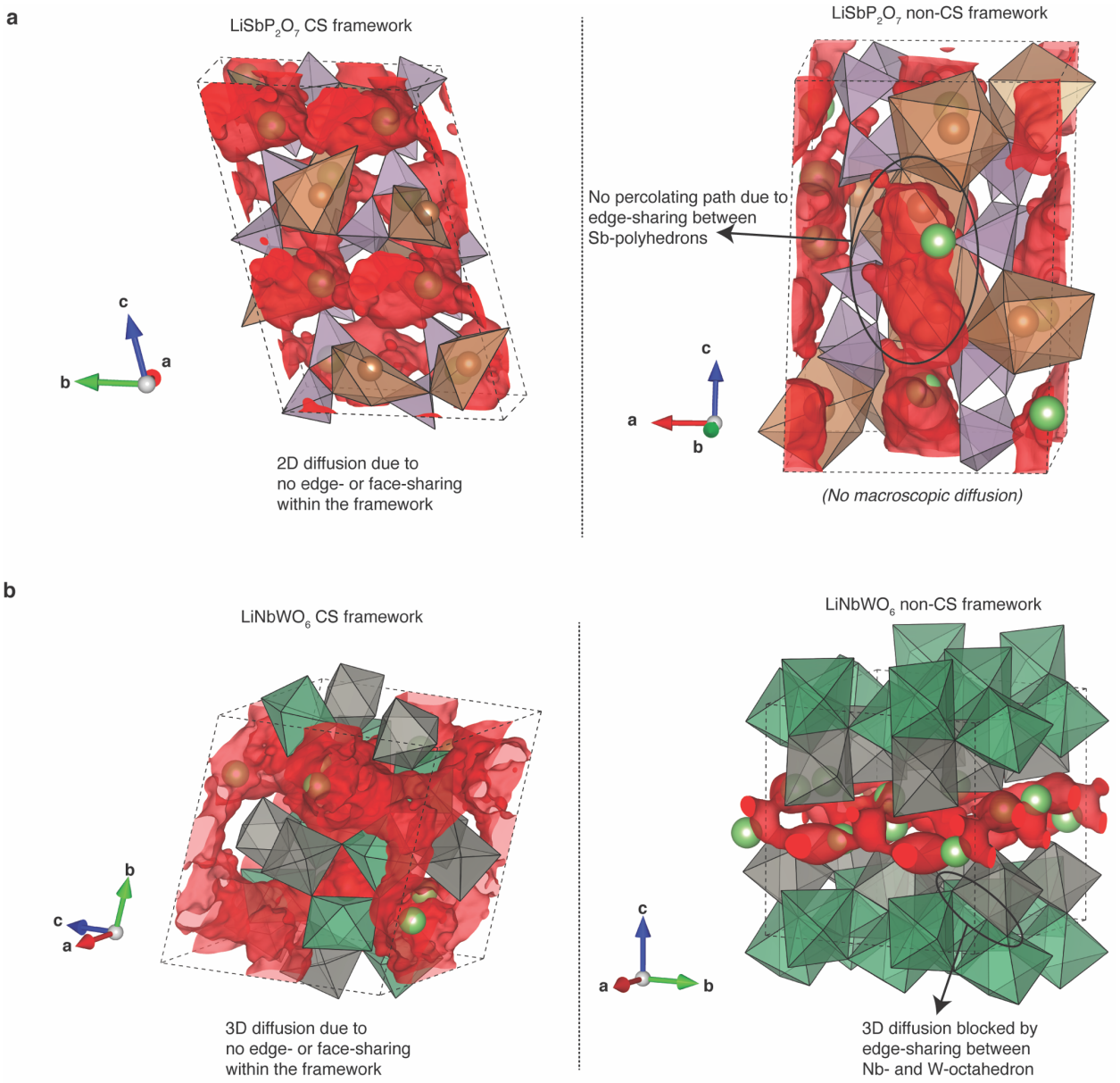


**Supplemental Figure 3.20 Comparing lithium probability density of CS and non-CS polymorphs.**

Li-ion probability density is shown for $LiSbP_2O_7$ (a) and $LiNbWO_6$ (b). The isosurface is drawn at $P = P_{max} / 100$ for $LiSbP_2O_7$ and $P = P_{max} / 1000$ for $LiNbWO_6$. The location of edge-sharing in non-CS frameworks are noted. Violet, orange, green and grey polyhedrons represent P, Sb, N and W coordination environments.

## Supplemental Note 3.5.
### Structural features of garnet Li-ion conductor

The garnet Li-ion conductor ($Li_7La_3Zr_2O_{12}$) shares similarities with CS frameworks, as shown in Supplemental Figure 3.21. Garnet framework has a well-defined *tet–oct–tet* migration channel with a tetrahedral site at 24d and an octahedral site at 96h. In terms of the Li environment, although the tetrahedral site is highly symmetric with a CSM value of 0.59, the octahedral site is quite distorted with a CSM value of 3.22. Second, the *tet–oct–tet* migration pathway in garnet is a RR (reduced-repulsion) channel. The distance from the tetrahedral Li to the edge-sharing La and the corner-sharing Zr is 3.30 and 3.69 Å, respectively. Although the octahedral Li face-share with the La polyhedron, the distance to the La atom is 3.07 Å because of the large size of the La cation. The distance from the octahedral Li to the edge-sharing Zr octahedron is 2.95 Å. Therefore, although face-sharing with the La cation occurs in the Li pathway, the large size of the La polyhedron makes the face-sharing distance larger than 3 Å, thereby making it a RR-channel. In addition, the octahedral site in garnet framework is distorted with a CSM value of 3.22. Therefore, the garnet structure has the most important features of the CS conductors.

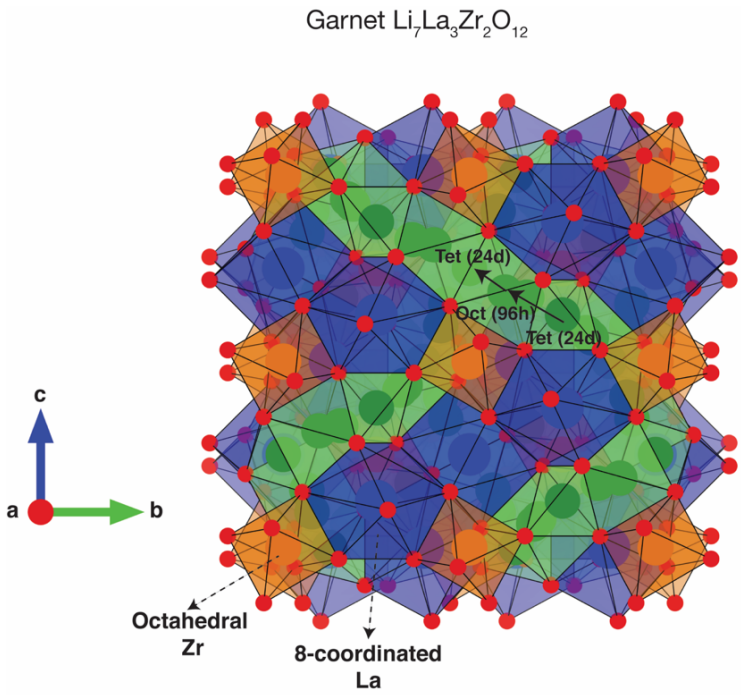


**Supplemental Figure 3.21 RR-channel in garnet structure.**
Green, Blue and orange polyhedrons represent Li, La and Zr coordination environment respectively. Red spheres represent oxygen anions. The tet-oct-tet pathway connecting 24d and 96h sites are shown.

## Supplemental Note 3.6.
### Structural features of perovskite Li-ion conductor

The perovskite Li-ion conductor shares two major similarities with CS frameworks, as shown in Supplemental Figure 3.22. First, the Li site is occupying a 12-coordinated cuboctahedral site positioned slightly off-center. This site is recognized as a highly distorted octahedral site with a CSM value of 16.5–17.4 and does not correspond to a typical tetrahedral or octahedral site. Second, the lithium conduction pathway from the A site passing through a square-planar bottleneck site to an adjacent vacant A site is a RR-channel. The distance from the Li atom in the A site to La in the nearest A site and Ti in the nearest B site is 3.07 and 2.62 Å, respectively. At the bottleneck as well, the distance from Li in the bottleneck site to La in the nearest A site other than the A site initially occupied by Li and the nearest B site is 4.34 and 2.70 Å, respectively. Therefore, the perovskite structures have the most important features of the CS conductors.

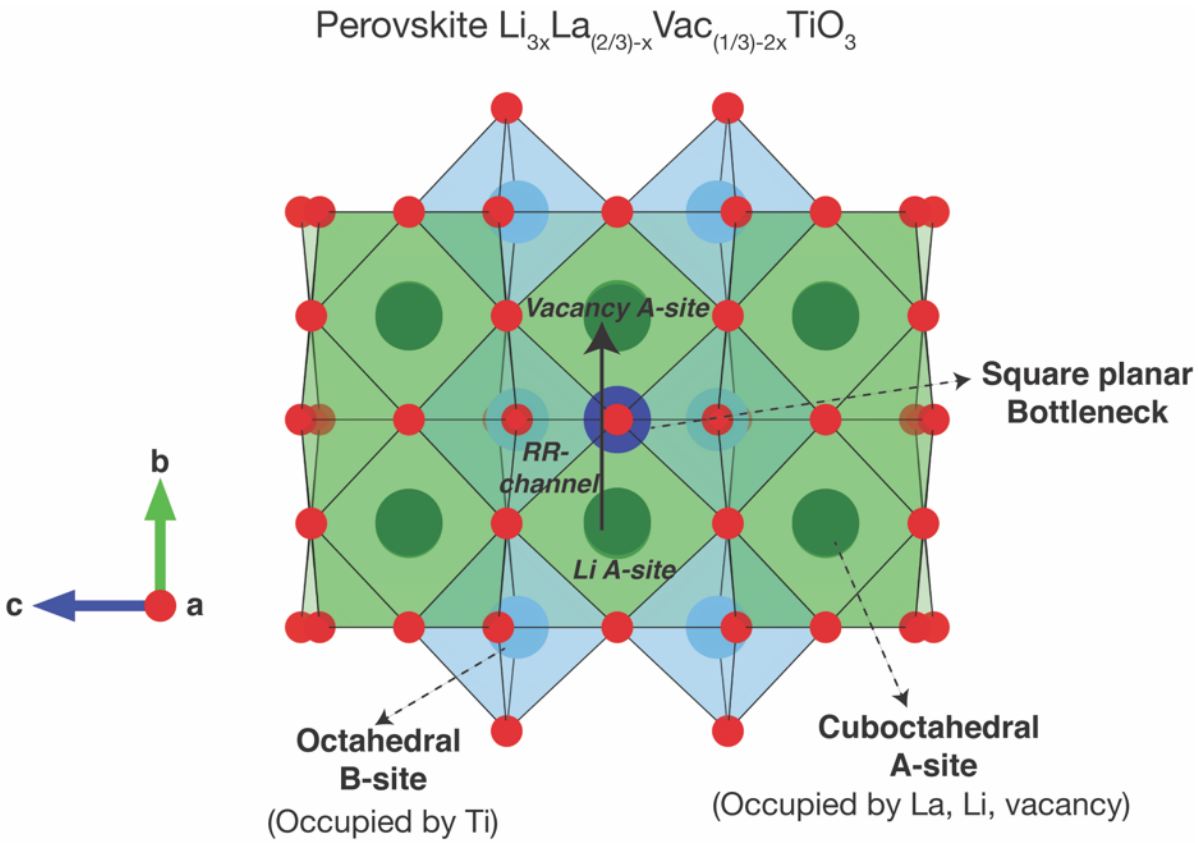


**Supplemental Figure 3.22 RR-channel in perovskite structure.**
Green polyhedrons represent A-site occupied by Li, La or vacancy. Light blue polyhedrons represent Ti octahedrons. Red spheres represent oxygen anions. The lithium migration pathway passing through a square planar bottleneck site is shown.

# Chapter 4 Conclusions and outlook

In summary, this dissertation focuses on designing superionic conductors which meet the requirement of all-solid-state batteries. We have explored new superionic conductors based on two different strategies: modifying composition to further enhance the property of known conductors, and searching new conductors based on structural features which benefit the migration of $Li^+$.

In Chapter 2, we presented a strategy to increase the ionic conductivity of sulfide Li-ion conductors through composition modification. Considering the wide usage of halogen in superionic conductors, we proposed to substitute halogen with pseudo-halogen to further improve the ionic conductivity. Li argyrodite system was used to demonstrate the feasibility of this strategy. $BH_4$-substituted Li argyrodite was successfully synthesized and displayed an enhanced ionic conductivity compared with halogen-substituted Li argyrodites. We further discussed the reason for the enhanced ionic conductivity and found that the enhanced conductivity mainly originates from the weak interaction between Li and the $BH_4$ polyanion instead of the typically expected paddle-wheel effect arising from cluster-ion rotation. The results provide a mechanistic understanding of how cluster ions can help increase Li-ion conductivity and shed light on design strategies for pseudohalogen-substituted superionic conductors.

In Chapter 3, we revealed a structural feature which could promote superionic conductivity in oxide Li-ion conductors. The crystal structures of known oxide Li-ion conductors are very limited. Most of representative oxide Li-ion conductors are NASICON-type or garnet-type materials. Based on these two structures, people have spent tons of effort on modifying the composition to get better ionic conductivities. In this context, it seems to be a better choice to search for oxide Li-conductors with new crystal structures. In this work, we find that corner-sharing connectivity of the oxide crystal structure framework is more likely to have distorted lithium environment and reduced interaction between lithium and non-lithium cations, which benefits the fast Li-ion migration. A high-throughput search was performed based on this structural feature and 10 new oxide Li-ion conductors were predicted. One of them, $LiGa(SeO_3)_2$, has been successfully synthesized and owns a bulk conductivity of 0.11 mS/cm which is in agreement with our prediction.

In this thesis, several design principles of superionic conductors were developed. To discover more superionic conductors based on these principles, a fast and efficient

syntheses-processing-testing workflow is required. To match with high-throughput computational screening, automated[196] and high-throughput[197] syntheses with short reaction period should be developed. Pelletization and high-temperature sintering are usually required before testing the ionic conductivity. To accelerate the processing and testing procedure, local ionic conductivity measurements[198] and low temperature processing technique[199,200] will be needed. In the meantime, to meet the requirement of solid-state batteries, we should not only consider the ionic conductivity while designing superionic conductors. Design principles should also be developed to improve the chemical and electrochemical stabilities of superionic conductors so that they could have better compatibility with high-voltage cathode active materials and Li metal anode.

# Bibliography


1. bp Statistical Review of World Energy 2022. https://www.bp.com/content/dam/bp/business-sites/en/global/corporate/pdfs/energy-economics/statistical-review/bp-stats-review-2022-full-report.pdf
2. Yang, Y., Okonkwo, E.G., Huang, G., Xu, S., Sun, W., and He, Y. (2021). On the sustainability of lithium ion battery industry – A review and perspective. Energy Storage Mater. *36*, 186–212. DOI:10.1016/J.ENSM.2020.12.019.
3. Faegh, E., Omasta, T., Hull, M., Ferrin, S., Shrestha, S., Lechman, J., Bolintineanu, D., Zuraw, M., and Mustain, W.E. (2018). Understanding the Dynamics of Primary Zn-MnO 2 Alkaline Battery Gassing with Operando Visualization and Pressure Cells . J. Electrochem. Soc. *165*, A2528–A2535. DOI:10.1149/2.0321811JES/XML.
4. Yu, X., Fu, Y., Cai, X., Kafafy, H., Wu, H., Peng, M., Hou, S., Lv, Z., Ye, S., and Zou, D. (2013). Flexible fiber-type zinc–carbon battery based on carbon fiber electrodes. Nano Energy *2*, 1242–1248. DOI:10.1016/J.NANOEN.2013.06.002.
5. Ruetschi, P. (1977). Review on the lead—acid battery science and technology. J. Power Sources *2*, 3–120. DOI:10.1016/0378-7753(77)85003-9.
6. Lun, Z., Ouyang, B., Kwon, D.H., Ha, Y., Foley, E.E., Huang, T.Y., Cai, Z., Kim, H., Balasubramanian, M., Sun, Y., et al. (2021). Cation-disordered rocksalt-type high-entropy cathodes for Li-ion batteries. Nat. Mater. *20*, 214–221. DOI:10.1038/s41563-020-00816-0.
7. Blomgren, G.E. (2017). The Development and Future of Lithium Ion Batteries. J. Electrochem. Soc. *164*, A5019–A5025. DOI:10.1149/2.0251701JES/XML.
8. Bibra, E.M., Connelly, E., Gorner, M., Lowans, C., Paoli, L., Tattini, J., and Teter, J. (2021). Global EV Outlook 2021: Accelerating Ambitions Despite the Pandemic.
9. Crabtree, G. (2019). The coming electric vehicle transformation: A future electric transportation market will depend on battery innovation. Science (80-. ). *366*, 422–424. DOI:10.1126/SCIENCE.AAX0704/ASSET/BCFFCBE0-73B9-4DCA-B07B-DFE0DEA2C0A9/ASSETS/GRAPHIC/366_422_F1.JPEG.
10. Sun, L., Liu, Y., Shao, R., Wu, J., Jiang, R., and Jin, Z. (2022). Recent progress and future perspective on practical silicon anode-based lithium ion batteries. Energy Storage Mater. *46*, 482–502. DOI:10.1016/J.ENSM.2022.01.042.

11. Hobold, G.M., Lopez, J., Guo, R., Minafra, N., Banerjee, A., Shirley Meng, Y., Shao-Horn, Y., and Gallant, B.M. (2021). Moving beyond 99.9% Coulombic efficiency for lithium anodes in liquid electrolytes. Nat. Energy 2021 610 *6*, 951–960. DOI:10.1038/s41560-021-00910-w.
12. Tian, Y., Zeng, G., Rutt, A., Shi, T., Kim, H., Wang, J., Koettgen, J., Sun, Y., Ouyang, B., Chen, T., et al. (2020). Promises and Challenges of Next-Generation "Beyond Li-ion" Batteries for Electric Vehicles and Grid Decarbonization. Chem. Rev. *121*, 1623–1669. DOI:10.1021/ACS.CHEMREV.0C00767.
13. BatPaC Model Software | Argonne National Laboratory https://www.anl.gov/cse/batpac-model-software.
14. Fan, L., Wei, S., Li, S., Li, Q., and Lu, Y. (2018). Recent Progress of the Solid-State Electrolytes for High-Energy Metal-Based Batteries. Adv. Energy Mater. *8*, 1702657. DOI:10.1002/AENM.201702657.
15. Gao, Z., Sun, H., Fu, L., Ye, F., Zhang, Y., Luo, W., and Huang, Y. (2018). Promises, Challenges, and Recent Progress of Inorganic Solid-State Electrolytes for All-Solid-State Lithium Batteries. Adv. Mater. *30*, 1705702. DOI:10.1002/adma.201705702.
16. Toyota set to sell long-range, fast-charging electric cars in 2022: paper | Reuters https://www.reuters.com/article/us-toyota-electric-cars-idUSKBN1AA035.
17. [Exclusive] Hyundai Motor solely developing EV batteries http://www.koreaherald.com/view.php?ud=20170405000762.
18. Solid Power, BMW partner to develop next-generation EV batteries | Reuters https://www.reuters.com/article/us-bmw-solid-power/solid-power-bmw-partner-to-develop-next-generation-ev-batteries-idUSKBN1EC16V.
19. Xi, G., Xiao, M., Wang, S., Han, D., Li, Y., Meng, Y., Xi, G., Xiao, M., Wang, S., Han, D., et al. (2021). Polymer-Based Solid Electrolytes: Material Selection, Design, and Application. Adv. Funct. Mater. *31*, 2007598. DOI:10.1002/ADFM.202007598.
20. Janek, J., and Zeier, W.G. (2016). A solid future for battery development. Nat. Energy 2016 19 *1*, 1–4. DOI:10.1038/nenergy.2016.141.
21. Tesla Says Car Fire Started in Battery - The New York Times https://archive.nytimes.com/wheels.blogs.nytimes.com/2013/10/02/highway-fire-of-tesla-model-s-included-its-lithium-battery/.
22. Samsung must act fast to keep an exploding phone from blowing up its brand | Samsung | The Guardian https://www.theguardian.com/technology/2016/oct/10/samsung-galaxy-note-7-exploding-phone-brand.
23. Wang, H., Yu, Z., Kong, X., Kim, S.C., Boyle, D.T., Qin, J., Bao, Z., and Cui,

Y. (2022). Liquid electrolyte: The nexus of practical lithium metal batteries. Joule *0*. DOI:10.1016/J.JOULE.2021.12.018.
24. Moshkovich, M., Gofer, Y., and Aurbach, D. (2001). Investigation of the Electrochemical Windows of Aprotic Alkali Metal (Li, Na, K) Salt Solutions. J. Electrochem. Soc. *148*, E155. DOI:10.1149/1.1357316/XML.
25. Zhou, L., Zuo, T.T., Kwok, C.Y., Kim, S.Y., Assoud, A., Zhang, Q., Janek, J., and Nazar, L.F. (2022). High areal capacity, long cycle life 4 V ceramic all-solid-state Li-ion batteries enabled by chloride solid electrolytes. Nat. Energy 2022 71 *7*, 83–93. DOI:10.1038/s41560-021-00952-0.
26. Gambe, Y., Sun, Y., and Honma, I. (2015). Development of Bipolar All-solid-state Lithium Battery Based on Quasi-solid-state Electrolyte Containing Tetraglyme-LiTFSA Equimolar Complex. Sci. Reports 2015 51 *5*, 1–4. DOI:10.1038/srep08869.
27. Kamaya, N., Homma, K., Yamakawa, Y., Hirayama, M., Kanno, R., Yonemura, M., Kamiyama, T., Kato, Y., Hama, S., Kawamoto, K., et al. (2011). A lithium superionic conductor. Nat. Mater. 2011 109 *10*, 682–686. DOI:10.1038/nmat3066.
28. Kato, Y., Hori, S., Saito, T., Suzuki, K., Hirayama, M., Mitsui, A., Yonemura, M., Iba, H., and Kanno, R. (2016). High-power all-solid-state batteries using sulfide superionic conductors. Nat. Energy *1*, 16030. DOI:10.1038/nenergy.2016.30.
29. Zhou, L., Assoud, A., Zhang, Q., Wu, X., and Nazar, L.F. (2019). New Family of Argyrodite Thioantimonate Lithium Superionic Conductors. J. Am. Chem. Soc. *141*, 19002–19013. DOI:10.1021/JACS.9B08357.
30. Tian, Y., Shi, T., Richards, W.D., Li, J., Kim, J.C., Bo, S.H., and Ceder, G. (2017). Compatibility issues between electrodes and electrolytes in solid-state batteries. Energy Environ. Sci. *10*, 1150–1166. DOI:10.1039/C7EE00534B.
31. Stability of Li, E., Han, F., Zhu, Y., He, X., Mo, Y., Wang, C., Han, F., Wang, C., Zhu, Y., He, X., et al. (2016). Electrochemical Stability of Li10GeP2S12 and Li7La3Zr2O12 Solid Electrolytes. Adv. Energy Mater. *6*, 1501590. DOI:10.1002/AENM.201501590.
32. Koerver, R., Aygün, I., Leichtweiß, T., Dietrich, C., Zhang, W., Binder, J.O., Hartmann, P., Zeier, W.G., and Janek, J. (2017). Capacity Fade in Solid-State Batteries: Interphase Formation and Chemomechanical Processes in Nickel-Rich Layered Oxide Cathodes and Lithium Thiophosphate Solid Electrolytes. Chem. Mater. *29*, 5574–5582. DOI:10.1021/ACS.CHEMMATER.7B00931/ASSET/IMAGES/LARGE/CM-2017-00931P_0006.JPEG.
33. Koerver, R., Zhang, W., De Biasi, L., Schweidler, S., Kondrakov, A.O., Kolling, S., Brezesinski, T., Hartmann, P., Zeier, W.G., and Janek, J. (2018).

Chemo-mechanical expansion of lithium electrode materials – on the route to mechanically optimized all-solid-state batteries. Energy Environ. Sci. *11*, 2142–2158. DOI:10.1039/C8EE00907D.

34. Lobe, S., Dellen, C., Finsterbusch, M., Gehrke, H.G., Sebold, D., Tsai, C.L., Uhlenbruck, S., and Guillon, O. (2016). Radio frequency magnetron sputtering of Li7La3Zr2O12 thin films for solid-state batteries. J. Power Sources *307*, 684–689. DOI:10.1016/J.JPOWSOUR.2015.12.054.
35. Saccoccio, M., Yu, J., Lu, Z., Kwok, S.C.T., Wang, J., Yeung, K.K., Yuen, M.M.F., and Ciucci, F. (2017). Low temperature pulsed laser deposition of garnet Li6.4La3Zr1.4Ta0.6O12 films as all solid-state lithium battery electrolytes. J. Power Sources *365*, 43–52. DOI:10.1016/J.JPOWSOUR.2017.08.020.
36. Nisula, M., Shindo, Y., Koga, H., and Karppinen, M. (2015). Atomic Layer Deposition of Lithium Phosphorus Oxynitride. Chem. Mater. *27*, 6987–6993. DOI:10.1021/ACS.CHEMMATER.5B02199/ASSET/IMAGES/LARGE/CM-2015-02199V_0011.JPEG.
37. Nam, Y.J., Cho, S.J., Oh, D.Y., Lim, J.M., Kim, S.Y., Song, J.H., Lee, Y.G., Lee, S.Y., and Jung, Y.S. (2015). Bendable and thin sulfide solid electrolyte film: A new electrolyte opportunity for free-standing and stackable high-energy all-solid-state lithium-ion batteries. Nano Lett. *15*, 3317–3323. DOI:10.1021/ACS.NANOLETT.5B00538/SUPPL_FILE/NL5B00538_SI_006.AVI.
38. Tian, Y., Sun, Y., Hannah, D.C., Xiao, Y., Liu, H., Chapman, K.W., Bo, S.H., and Ceder, G. (2019). Reactivity-Guided Interface Design in Na Metal Solid-State Batteries. Joule *3*, 1037–1050. DOI:10.1016/J.JOULE.2018.12.019.
39. Porz, L., Swamy, T., Sheldon, B.W., Rettenwander, D., Frömling, T., Thaman, H.L., Berendts, S., Uecker, R., Craig Carter, W., Chiang, Y.-M., et al. (2017). Mechanism of Lithium Metal Penetration through Inorganic Solid Electrolytes. Adv. Energy Mater. *7*, 1701003. DOI:10.1002/AENM.201701003.
40. Han, X., Gong, Y., Fu, K., He, X., Hitz, G.T., Dai, J., Pearse, A., Liu, B., Wang, H., Rubloff, G., et al. (2016). Negating interfacial impedance in garnet-based solid-state Li metal batteries. Nat. Mater. 2017 165 *16*, 572–579. DOI:10.1038/nmat4821.
41. Murayama, M., Sonoyama, N., Yamada, A., and Kanno, R. (2004). Material design of new lithium ionic conductor, thio-LISICON, in the Li2S–P2S5 system. Solid State Ionics *170*, 173–180. DOI:10.1016/J.SSI.2004.02.025.
42. Gao, Y.X., Wang, X.P., Wang, W.G., Zhuang, Z., Zhang, D.M., and Fang, Q.F. (2010). Synthesis, ionic conductivity, and chemical compatibility of garnet-like lithium ionic conductor Li5La3Bi2O12. Solid State Ionics *181*, 1415–1419. DOI:10.1016/J.SSI.2010.08.012.

43. Thangadurai, V., and Weppner, W. (2005). Li6ALa2Ta2O12 (A = Sr, Ba): Novel Garnet-Like Oxides for Fast Lithium Ion Conduction. Adv. Funct. Mater. *15*, 107–112. DOI:10.1002/ADFM.200400044.
44. Yamane, H., Shibata, M., Shimane, Y., Junke, T., Seino, Y., Adams, S., Minami, K., Hayashi, A., and Tatsumisago, M. (2007). Crystal structure of a superionic conductor, Li7P3S11. Solid State Ionics *178*, 1163–1167. DOI:10.1016/J.SSI.2007.05.020.
45. Murugan, R., Thangadurai, V., and Weppner, W. (2007). Fast Lithium Ion Conduction in Garnet-Type Li7La3Zr2O12. Angew. Chemie Int. Ed. *46*, 7778–7781. DOI:10.1002/ANIE.200701144.
46. Deiseroth, H.-J., Kong, S.-T., Eckert, H., Vannahme, J., Reiner, C., Zaiß, T., and Schlosser, M. (2008). Li6PS5X: A Class of Crystalline Li-Rich Solids With an Unusually High Li+ Mobility. Angew. Chemie *120*, 767–770. DOI:10.1002/ange.200703900.
47. Maekawa, H., Matsuo, M., Takamura, H., Ando, M., Noda, Y., Karahashi, T., and Orimo, S.I. (2009). Halide-stabilized LiBH4, a room-temperature lithium fast-ion conductor. J. Am. Chem. Soc. *131*, 894–895. DOI:10.1021/ja807392k.
48. Matsuo, M., Remhof, A., Martelli, P., Caputo, R., Ernst, M., Miura, Y., Sato, T., Oguchi, H., Maekawa, H., Takamura, H., et al. (2009). Complex Hydrides with $(BH_4)^-$ and $(NH_2)^-$ Anions as New Lithium Fast-Ion Conductors. J. Am. Chem. Soc. *131*, 16389–16391. DOI:10.1021/ja907249p.
49. Matsuo, M., Sato, T., Miura, Y., Oguchi, H., Zhou, Y., Maekawa, H., Takamura, H., and Orimo, S.I. (2010). Synthesis and lithium fast-ion conductivity of a new complex hydride Li3(NH2)2I with double-layered structure. Chem. Mater. *22*, 2702–2704. DOI:10.1021/cm1006857.
50. Ohta, S., Kobayashi, T., and Asaoka, T. (2011). High lithium ionic conductivity in the garnet-type oxide Li7−X La3(Zr2−X, NbX)O12 (X = 0–2). J. Power Sources *196*, 3342–3345. DOI:10.1016/J.JPOWSOUR.2010.11.089.
51. Li, Y., Han, J.T., Wang, C.A., Xie, H., and Goodenough, J.B. (2012). Optimizing Li + conductivity in a garnet framework. J. Mater. Chem. *22*, 15357–15361. DOI:10.1039/C2JM31413D.
52. Zhao, Y., and Daemen, L.L. (2012). Superionic Conductivity in Lithium-Rich Anti-Perovskites. J. Am. Chem. Soc. *134*, 15042–15047. DOI:10.1021/ja305709z.
53. Bron, P., Johansson, S., Zick, K., Der Günne, J.S.A., Dehnen, S., and Roling, B. (2013). Li10SnP2S12: An affordable lithium superionic conductor. J. Am. Chem. Soc. *135*, 15694–15697. DOI:10.1021/JA407393Y/SUPPL_FILE/JA407393Y_SI_002.CIF.
54. Wu, J.F., Chen, E.Y., Yu, Y., Liu, L., Wu, Y., Pang, W.K., Peterson, V.K., and Guo, X. (2017). Gallium-doped Li7La3Zr2O12 garnet-type electrolytes with

high lithium-ion conductivity. ACS Appl. Mater. Interfaces *9*, 1542–1552. DOI:10.1021/ACSAMI.6B13902/ASSET/IMAGES/LARGE/AM-2016-13902M_0009.JPEG.

55. Liu, Z., Fu, W., Payzant, E.A., Yu, X., Wu, Z., Dudney, N.J., Kiggans, J., Hong, K., Rondinone, A.J., and Liang, C. (2013). Anomalous High Ionic Conductivity of Nanoporous β-Li3PS4. J. Am. Chem. Soc. *135*, 975–978. DOI:10.1021/ja3110895.
56. Kuhn, A., Duppel, V., and Lotsch, B. V (2013). Tetragonal Li10GeP2S12 and Li 7GePS8-exploring the Li ion dynamics in LGPS Li electrolytes. Energy Environ. Sci. *6*, 3548–3552. DOI:10.1039/c3ee41728j.
57. Rangasamy, E., Liu, Z., Gobet, M., Pilar, K., Sahu, G., Zhou, W., Wu, H., Greenbaum, S., and Liang, C. (2015). An iodide-based Li 7 P 2 S 8 I superionic conductor. J. Am. Chem. Soc. *137*, 1384–1387. DOI:10.1021/ja508723m.
58. Tang, W.S., Unemoto, A., Zhou, W., Stavila, V., Matsuo, M., Wu, H., Orimo, S.I., and Udovic, T.J. (2015). Unparalleled lithium and sodium superionic conduction in solid electrolytes with large monovalent cage-like anions. Energy Environ. Sci. *8*, 3637–3645. DOI:10.1039/c5ee02941d.
59. Tang, W.S., Yoshida, K., Soloninin, A. V., Skoryunov, R. V., Babanova, O.A., Skripov, A. V., Dimitrievska, M., Stavila, V., Orimo, S.I., and Udovic, T.J. (2016). Stabilizing Superionic-Conducting Structures via Mixed-Anion Solid Solutions of Monocarba-closo-borate Salts. ACS Energy Lett. *1*, 659–664. DOI:10.1021/ACSENERGYLETT.6B00310/ASSET/IMAGES/LARGE/NZ-2016-00310Y_0004.JPEG.
60. D. Richards, W., Yan Wang, J. Miara, L., Chul Kim, J., and Gerbrand Ceder (2016). Design of Li 1+2x Zn 1−x PS 4 , a new lithium ion conductor. Energy Environ. Sci. *9*, 3272–3278. DOI:10.1039/C6EE02094A.
61. Yan, Y., Kühnel, R.S., Remhof, A., Duchêne, L., Reyes, E.C., Rentsch, D., Łodziana, Z., and Battaglia, C. (2017). A Lithium Amide-Borohydride Solid-State Electrolyte with Lithium-Ion Conductivities Comparable to Liquid Electrolytes. Adv. Energy Mater. *7*, 1–7. DOI:10.1002/aenm.201700294.
62. Xu, X., Wen, Z., Gu, Z., Xu, X., and Lin, Z. (2004). Lithium ion conductive glass ceramics in the system Li1.4Al0.4(Ge1−xTix)1.6(PO4)3 (x=0–1.0). Solid State Ionics *171*, 207–213. DOI:10.1016/J.SSI.2004.05.009.
63. Sedlmaier, S.J., Indris, S., Dietrich, C., Yavuz, M., Dräger, C., Von Seggern, F., Sommer, H., and Janek, J. (2017). Li4PS4I: A Li+ Superionic Conductor Synthesized by a Solvent-Based Soft Chemistry Approach. Chem. Mater. *29*, 1830–1835. DOI:10.1021/acs.chemmater.7b00013.
64. Asano, T., Sakai, A., Ouchi, S., Sakaida, M., Miyazaki, A., and Hasegawa, S. (2018). Solid Halide Electrolytes with High Lithium-Ion Conductivity for Application in 4 V Class Bulk-Type All-Solid-State Batteries. Adv. Mater. *30*,

1803075. DOI:10.1002/adma.201803075.
65. Aono, H., Sugimoto, E., Sadaoka, Y., Imanaka, N., and Adachi, G. (1990). Ionic Conductivity of Solid Electrolytes Based on Lithium Titanium Phosphate. J. Electrochem. Soc. *137*, 1023–1027. DOI:10.1149/1.2086597/XML.
66. Alpen, U. V., Rabenau, A., and Talat, G.H. (2008). Ionic conductivity in Li3N single crystals. Appl. Phys. Lett. *30*, 621. DOI:10.1063/1.89283.
67. Itoh, M., Inaguma, Y., Jung, W.H., Chen, L., and Nakamura, T. (1994). High lithium ion conductivity in the perovskite-type compounds Ln12Li12TiO3(Ln=La,Pr,Nd,Sm). Solid State Ionics *70–71*, 203–207. DOI:10.1016/0167-2738(94)90310-7.
68. Kanno, R., and Murayama, M. (2001). Lithium Ionic Conductor Thio-LISICON: The Li2 S - GeS2 - P 2 S 5 System. J. Electrochem. Soc. *148*, A742. DOI:10.1149/1.1379028.
69. Hayashi, A., Hama, S., Morimoto, H., Tatsumisago, M., and Minami, T. (2001). Preparation of Li2S–P2S5 Amorphous Solid Electrolytes by Mechanical Milling. J. Am. Ceram. Soc. *84*, 477–79. DOI:10.1111/J.1151-2916.2001.TB00685.X.
70. Thangadurai, V., Kaack, H., and Weppner, W.J.F. (2003). Novel Fast Lithium Ion Conduction in Garnet-Type Li5La3M2O12 (M = Nb, Ta). J. Am. Ceram. Soc. *86*, 437–440. DOI:10.1111/J.1151-2916.2003.TB03318.X.
71. Murayama, M., Kanno, R., Irie, M., Ito, S., Hata, T., Sonoyama, N., and Kawamoto, Y. (2002). Synthesis of New Lithium Ionic Conductor Thio-LISICON—Lithium Silicon Sulfides System. J. Solid State Chem. *168*, 140–148. DOI:10.1006/JSSC.2002.9701.
72. Famprikis, T., Canepa, P., Dawson, J.A., Islam, M.S., and Masquelier, C. (2019). Fundamentals of inorganic solid-state electrolytes for batteries. Nat. Mater. 2019 1812 *18*, 1278–1291. DOI:10.1038/s41563-019-0431-3.
73. Wang, Y., Richards, W.D., Ong, S.P., Miara, L.J., Kim, J.C., Mo, Y., and Ceder, G. (2015). Design principles for solid-state lithium superionic conductors. Nat. Mater. *14*, 1026–1031. DOI:10.1038/nmat4369.
74. Sun, Y., Wang, Y., Liang, X., Xia, Y., Peng, L., Jia, H., Li, H., Bai, L., Feng, J., Jiang, H., et al. (2019). Rotational Cluster Anion Enabling Superionic Conductivity in Sodium-Rich Antiperovskite $Na_3OBH_4$. J. Am. Chem. Soc., jacs.9b01746. DOI:10.1021/jacs.9b01746.
75. Moon, C.K., Lee, H.-J., Park, K.H., Kwak, H., Heo, J.W., Choi, K., Yang, H., Kim, M.-S., Hong, S.-T., Lee, J.H., et al. (2018). Vacancy-Driven Na+ Superionic Conduction in New Ca-doped Na3PS4 for All-Solid-State Na-ion Batteries. ACS Energy Lett., acsenergylett.8b01479. DOI:10.1021/acsenergylett.8b01479.
76. Nolan, A.M., Zhu, Y., He, X., Bai, Q., and Mo, Y. (2018). Computation-

Accelerated Design of Materials and Interfaces for All-Solid-State Lithium-Ion Batteries. Joule *2*, 2016–2046. DOI:10.1016/J.JOULE.2018.08.017.

77. Xu, M., Park, M.S., Lee, J.M., Kim, T.Y., Park, Y.S., and Ma, E. (2012). Mechanisms of Li + transport in garnet-type cubic Li 3+xLa 3M 2O 12 (M = Te, Nb, Zr). Phys. Rev. B - Condens. Matter Mater. Phys. *85*. DOI:10.1103/PhysRevB.85.052301.
78. Pradel, A., and Ribes, M. (1986). Electrical properties of lithium conductive silicon sulfide glasses prepared by twin roller quenching. Solid State Ionics *18–19*, 351–355. DOI:10.1016/0167-2738(86)90139-6.
79. Souquet, J.L., Robinel, E., Barrau, B., and Ribes, M. (1981). Glass formation and ionic conduction in the M2S□GeS2 (M = Li, Na, Ag) systems. Solid State Ionics *3–4*, 317–321. DOI:10.1016/0167-2738(81)90105-3.
80. Sakuda, A., Hayashi, A., and Tatsumisago, M. (2013). Sulfide Solid Electrolyte with Favorable Mechanical Property for All-Solid-State Lithium Battery. Sci. Reports 2013 31 *3*, 1–5. DOI:10.1038/srep02261.
81. Minami, T., Hayashi, A., and Tatsumisago, M. (2006). Recent progress of glass and glass-ceramics as solid electrolytes for lithium secondary batteries. Solid State Ionics *177*, 2715–2720. DOI:10.1016/J.SSI.2006.07.017.
82. Adeli, P., Bazak, J.D., Park, K.H., Kochetkov, I., Huq, A., Goward, G.R., and Nazar, L.F. (2019). Boosting Solid-State Diffusivity and Conductivity in Lithium Superionic Argyrodites by Halide Substitution. Angew. Chemie *131*, 8773–8778. DOI:10.1002/ANGE.201814222.
83. Ouyang, B., Wang, Y., Sun, Y., and Ceder, G. (2020). Computational Investigation of Halogen-Substituted Na Argyrodites as Solid-State Superionic Conductors. Chem. Mater. *32*, 1896–1903. DOI:10.1021/ACS.CHEMMATER.9B04541.
84. Kraft, M.A., Culver, S.P., Calderon, M., Böcher, F., Krauskopf, T., Senyshyn, A., Dietrich, C., Zevalkink, A., Janek, J., and Zeier, W.G. (2017). Influence of Lattice Polarizability on the Ionic Conductivity in the Lithium Superionic Argyrodites Li6PS5X (X = Cl, Br, I). J. Am. Chem. Soc. *139*, 10909–10918. DOI:10.1021/jacs.7b06327.
85. Zhou, L., Park, K.H., Sun, X., Lalère, F., Adermann, T., Hartmann, P., and Nazar, L.F. (2019). Solvent-Engineered Design of Argyrodite Li 6 PS 5 X (X = Cl, Br, I) Solid Electrolytes with High Ionic Conductivity. ACS Energy Lett. *4*, 265–270. DOI:10.1021/ACSENERGYLETT.8B01997/SUPPL_FILE/NZ8B01997_SI_001.PDF.
86. Xiao, Y., Wang, Y., Bo, S.H., Kim, J.C., Miara, L.J., and Ceder, G. (2019). Understanding interface stability in solid-state batteries. Nat. Rev. Mater. 2019 52 *5*, 105–126. DOI:10.1038/s41578-019-0157-5.

87. Zhu, Y., He, X., and Mo, Y. (2015). Origin of Outstanding Stability in the Lithium Solid Electrolyte Materials: Insights from Thermodynamic Analyses Based on First-Principles Calculations. ACS Appl. Mater. Interfaces *7*, 23685–23693. DOI:10.1021/ACSAMI.5B07517/ASSET/IMAGES/LARGE/AM-2015-07517G_0004.JPEG.
88. Richards, W.D., Miara, L.J., Wang, Y., Kim, J.C., and Ceder, G. (2016). Interface Stability in Solid-State Batteries. Chem. Mater. *28*, 266–273. DOI:10.1021/ACS.CHEMMATER.5B04082/ASSET/IMAGES/LARGE/CM-2015-04082X_0005.JPEG.
89. Awaka, J., Kijima, N., Hayakawa, H., and Akimoto, J. (2009). Synthesis and structure analysis of tetragonal Li7La3Zr2O12 with the garnet-related type structure. J. Solid State Chem. *182*, 2046–2052. DOI:10.1016/J.JSSC.2009.05.020.
90. Rangasamy, E., Wolfenstine, J., and Sakamoto, J. (2012). The role of Al and Li concentration on the formation of cubic garnet solid electrolyte of nominal composition Li7La3Zr2O12. Solid State Ionics *206*, 28–32. DOI:10.1016/J.SSI.2011.10.022.
91. Arbi, K., Rojo, J.M., and Sanz, J. (2007). Lithium mobility in titanium based Nasicon Li1+xTi2−xAlx(PO4)3 and LiTi2−x Zrx(PO4)3 materials followed by NMR and impedance spectroscopy. J. Eur. Ceram. Soc. *27*, 4215–4218. DOI:10.1016/J.JEURCERAMSOC.2007.02.118.
92. Ibarra, J., Várez, A., León, C., Santamaría, J., Torres-Martínez, L.M., and Sanz, J. (2000). Influence of composition on the structure and conductivity of the fast ionic conductors La2/3−xLi3xTiO3 (0.03≤x≤0.167). Solid State Ionics *134*, 219–228. DOI:10.1016/S0167-2738(00)00761-X.
93. Inaguma, Y., Liquan, C., Itoh, M., Nakamura, T., Uchida, T., Ikuta, H., and Wakihara, M. (1993). High ionic conductivity in lithium lanthanum titanate. Solid State Commun. *86*, 689–693. DOI:10.1016/0038-1098(93)90841-A.
94. Motavalli, J. (2015). Technology: A solid future. Nature *526*, S96–S97. DOI:10.1038/526S96a.
95. Ceder, G., Ong, S.P., and Wang, Y. (2018). Predictive modeling and design rules for solid electrolytes. MRS Bull. *43*, 782–788. DOI:10.1557/mrs.2018.210.
96. Deiseroth, H.J., Kong, S.T., Eckert, H., Vannahme, J., Reiner, C., Zaiß, T., and Schlosser, M. (2008). Li6PS5X: A class of crystalline Li-rich solids with an unusually high Li+ mobility. Angew. Chemie - Int. Ed. *47*, 755–758. DOI:10.1002/anie.200703900.
97. Adeli, P., Bazak, J.D., Park, K.H., Kochetkov, I., Huq, A., Goward, G.R., and Nazar, L.F. (2019). Boosting Solid-State Diffusivity and Conductivity in Lithium Superionic Argyrodites by Halide Substitution. Angew. Chemie *131*,

8773–8778. DOI:10.1002/ANGE.201814222.
98. Murugan, R., Thangadurai, V., and Weppner, W. (2007). Fast lithium ion conduction in garnet-type Li7La 3Zr2O12. Angew. Chemie - Int. Ed. *46*, 7778–7781. DOI:10.1002/anie.200701144.
99. Shou-Hang Bo, Yan Wang, and Gerbrand Ceder (2016). Structural and Na-ion conduction characteristics of Na 3 PS x Se 4−x. J. Mater. Chem. A *4*, 9044–9053. DOI:10.1039/C6TA03027K.
100. Wang, Y., Richards, W.D., Ong, S.P., Miara, L.J., Kim, J.C., Mo, Y., and Ceder, G. (2015). Design principles for solid-state lithium superionic conductors. Nat. Mater. 2015 1410 *14*, 1026–1031. DOI:10.1038/nmat4369.
101. Xiao, Y., Jun, K., Wang, Y., Miara, L.J., Tu, Q., and Ceder, G. (2021). Lithium Oxide Superionic Conductors Inspired by Garnet and NASICON Structures. Adv. Energy Mater. *11*, 2101437. DOI:10.1002/AENM.202101437.
102. Richards, W.D., Wang, Y., Miara, L.J., Kim, J.C., and Ceder, G. (2016). Design of Li 1+2x Zn 1−x PS 4 , a new lithium ion conductor. Energy Environ. Sci. *9*, 3272–3278. DOI:10.1039/C6EE02094A.
103. Liu, Y., Wang, S., Nolan, A.M., Ling, C., Mo, Y., Li, garnet, Li, N., Liu, Y., Wang, S., Nolan, A.M., et al. (2020). Tailoring the Cation Lattice for Chloride Lithium-Ion Conductors. Adv. Energy Mater. *10*, 2002356. DOI:10.1002/AENM.202002356.
104. Wang, R., Ping, W., Wang, C., Liu, Y., Gao, J., Dong, Q., Wang, X., Mo, Y., Hu, L., Wang, R., et al. (2020). Computation-Guided Synthesis of New Garnet-Type Solid-State Electrolytes via an Ultrafast Sintering Technique. Adv. Mater. *32*, 2005059. DOI:10.1002/ADMA.202005059.
105. Canepa, P., Bo, S.H., Sai Gautam, G., Key, B., Richards, W.D., Shi, T., Tian, Y., Wang, Y., Li, J., and Ceder, G. (2017). High magnesium mobility in ternary spinel chalcogenides. Nat. Commun. 2017 81 *8*, 1–8. DOI:10.1038/s41467-017-01772-1.
106. Matsuo, M., and Orimo, S.I. (2011). Lithium Fast-Ionic Conduction in Complex Hydrides: Review and Prospects. Adv. Energy Mater. *1*, 161–172. DOI:10.1002/AENM.201000012.
107. Unemoto, A., Wu, H., Udovic, T.J., Matsuo, M., Ikeshoji, T., and Orimo, S.I. (2016). Fast lithium-ionic conduction in a new complex hydride-sulphide crystalline phase. Chem. Commun. *52*, 564–566. DOI:10.1039/c5cc07793a.
108. Wang, F., Evans, H.A., Kim, K., Yin, L., Li, Y., Tsai, P.-C., Liu, J., Lapidus, S.H., Brown, C.M., Siegel, D.J., et al. (2020). Dynamics of Hydroxyl Anions Promotes Lithium Ion Conduction in Antiperovskite Li2OHCl. Chem. Mater. *32*, 8481–8491. DOI:10.1021/ACS.CHEMMATER.0C02602.
109. Fang, H., and Jena, P. (2017). Li-rich antiperovskite superionic conductors based on cluster ions. Proc. Natl. Acad. Sci. *114*, 11046–11051.

DOI:10.1073/PNAS.1704086114.
110. Fang, H., and Jena, P. (2018). Sodium Superionic Conductors Based on Clusters. ACS Appl. Mater. Interfaces *11*, 963–972. DOI:10.1021/ACSAMI.8B19003.
111. Sun, Y., Wang, Y., Liang, X., Xia, Y., Peng, L., Jia, H., Li, H., Bai, L., Feng, J., Jiang, H., et al. (2019). Rotational Cluster Anion Enabling Superionic Conductivity in Sodium-Rich Antiperovskite Na3OBH4. J. Am. Chem. Soc. *141*, 5640–5644. DOI:10.1021/JACS.9B01746.
112. Zhou, L., Assoud, A., Zhang, Q., Wu, X., and Nazar, L.F. (2019). New Family of Argyrodite Thioantimonate Lithium Superionic Conductors. J. Am. Chem. Soc. *141*, 19002–19013. DOI:10.1021/JACS.9B08357.
113. Zhou, L., Minafra, N., Zeier, W.G., and Nazar, L.F. (2021). Innovative Approaches to Li-Argyrodite Solid Electrolytes for All-Solid-State Lithium Batteries. Acc. Chem. Res. *54*, 2717–2728. DOI:10.1021/ACS.ACCOUNTS.0C00874.
114. Zhou, L., Park, K.H., Sun, X., Lalère, F., Adermann, T., Hartmann, P., and Nazar, L.F. (2019). Solvent-Engineered Design of Argyrodite Li6PS5X (X = Cl, Br, I) Solid Electrolytes with High Ionic Conductivity. ACS Energy Lett. *4*, 265–270. DOI:10.1021/acsenergylett.8b01997.
115. Kaup, K., Bishop, K., Assoud, A., Liu, J., and Nazar, L.F. (2021). Fast Ion-Conducting Thioboracite with a Perovskite Topology and Argyrodite-like Lithium Substructure. J. Am. Chem. Soc. *143*, 6952–6961. DOI:10.1021/JACS.1C00941/SUPPL_FILE/JA1C00941_SI_001.PDF.
116. De Klerk, N.J.J., Rosłoń, I., and Wagemaker, M. (2016). Diffusion Mechanism of Li Argyrodite Solid Electrolytes for Li-Ion Batteries and Prediction of Optimized Halogen Doping: The Effect of Li Vacancies, Halogens, and Halogen Disorder. Chem. Mater. *28*, 7955–7963. DOI:10.1021/acs.chemmater.6b03630.
117. Patel, S. V., Banerjee, S., Liu, H., Wang, P., Chien, P.H., Feng, X., Liu, J., Ong, S.P., and Hu, Y.Y. (2021). Tunable Lithium-Ion Transport in Mixed-Halide Argyrodites Li6- xPS5- xClBrx: An Unusual Compositional Space. Chem. Mater. *33*, 1435–1443. DOI:10.1021/ACS.CHEMMATER.0C04650/SUPPL_FILE/CM0C04650_SI_001.PDF.
118. Feng, X., Chien, P.H., Wang, Y., Patel, S., Wang, P., Liu, H., Immediato-Scuotto, M., and Hu, Y.Y. (2020). Enhanced ion conduction by enforcing structural disorder in Li-deficient argyrodites Li6−xPS5−xCl1+x. Energy Storage Mater. *30*, 67–73. DOI:10.1016/J.ENSM.2020.04.042.
119. Wang, P., Liu, H., Patel, S., Feng, X., Chien, P.H., Wang, Y., and Hu, Y.Y. (2020). Fast Ion Conduction and Its Origin in Li6- xPS5- xBr1+ x. Chem.

Mater. *32*, 3833–3840. DOI:10.1021/ACS.CHEMMATER.9B05331/SUPPL_FILE/CM9B05331_SI_001.PDF.
120. Smith, J.G., and Siegel, D.J. (2020). Low-temperature paddlewheel effect in glassy solid electrolytes. Nat. Commun. 2020 111 *11*, 1–11. DOI:10.1038/s41467-020-15245-5.
121. Song, A.-Y., Turcheniuk, K., Leisen, J., Xiao, Y., Meda, L., Borodin, O., and Yushin, G. (2020). Understanding Li-Ion Dynamics in Lithium Hydroxychloride (Li2OHCl) Solid State Electrolyte via Addressing the Role of Protons. Adv. Energy Mater. *10*, 1903480. DOI:10.1002/AENM.201903480.
122. Zhang, Z., Roy, P.-N., Li, H., Avdeev, M., and Nazar, L.F. (2019). Coupled Cation–Anion Dynamics Enhances Cation Mobility in Room-Temperature Superionic Solid-State Electrolytes. J. Am. Chem. Soc. *141*, 19360–19372. DOI:10.1021/JACS.9B09343.
123. Ong, S.P., Wang, L., Kang, B., and Ceder, G. (2008). Li−Fe−P−O2 Phase Diagram from First Principles Calculations. Chem. Mater. *20*, 1798–1807. DOI:10.1021/CM702327G.
124. Ong, S.P., Mo, Y., Richards, W.D., Miara, L., Lee, H.S., and Ceder, G. (2012). Phase stability, electrochemical stability and ionic conductivity of the Li 10±1 MP 2 X 12 (M = Ge, Si, Sn, Al or P, and X = O, S or Se) family of superionic conductors. Energy Environ. Sci. *6*, 148–156. DOI:10.1039/C2EE23355J.
125. Mo, Y., Ong, S.P., and Ceder, G. (2012). First principles study of the Li 10GeP 2S 12 lithium super ionic conductor material. Chem. Mater. *24*, 15–17. DOI:10.1021/CM203303Y/SUPPL_FILE/CM203303Y_SI_001.PDF.
126. Sun, W., Dacek, S.T., Ong, S.P., Hautier, G., Jain, A., Richards, W.D., Gamst, A.C., Persson, K.A., and Ceder, G. (2016). The thermodynamic scale of inorganic crystalline metastability. Sci. Adv. *2*, e1600225. DOI:10.1126/sciadv.1600225.
127. Sakuda, A., Yamauchi, A., Yubuchi, S., Kitamura, N., Idemoto, Y., Hayashi, A., and Tatsumisago, M. (2018). Mechanochemically Prepared Li2S–P2S5–LiBH4 Solid Electrolytes with an Argyrodite Structure. ACS Omega *3*, 5453–5458. DOI:10.1021/ACSOMEGA.8B00377.
128. Züttel, A., Wenger, P., Rentsch, S., Sudan, P., Mauron, P., and Emmenegger, C. (2003). LiBH4 a new hydrogen storage material. J. Power Sources *118*, 1–7. DOI:10.1016/S0378-7753(03)00054-5.
129. Wu, L., Zhang, Z., Liu, G., Weng, W., Zhang, Z., and Yao, X. (2021). Wet-Milling Synthesis of Superionic Lithium Argyrodite Electrolytes with Different Concentrations of Lithium Vacancy. ACS Appl. Mater. Interfaces *13*, 46644–46649.

DOI:10.1021/ACSAMI.1C13031/ASSET/IMAGES/LARGE/AM1C13031_0006.JPEG.
130. Zhang, Y.-Q., Tian, Y., Xiao, Y., Miara, L.J., Aihara, Y., Tsujimura, T., Shi, T., Scott, M.C., and Ceder, G. (1903). Direct Visualization of the Interfacial Degradation of Cathode Coatings in Solid State Batteries: A Combined Experimental and Computational Study. DOI:10.1002/aenm.201903778.
131. Tian, Y., Shi, T., Richards, W.D., Li, J., Kim, J.C., Bo, S.-H., and Ceder, G. (2017). Compatibility issues between electrodes and electrolytes in solid-state batteries. Energy Environ. Sci. *10*, 1150–1166. DOI:10.1039/C7EE00534B.
132. Soper, H.E., Young, A.W., Cave, B.M., Lee, A., and Pearson, K. (1917). On the Distribution of the Correlation Coefficient in Small Samples. Appendix II to the Papers of "Student" and R. A. Fisher. Biometrika *11*, 328. DOI:10.2307/2331830.
133. Rodgers, J.L., and Nicewander, ; W Alan (1988). Thirteen Ways to Look at the Correlation Coefficient. Am. Stat. *42*, 59–66.
134. Buda, A., and Jarynowski, A. (2010). Life time of correlations and its applications (Andrzej Buda Wydawnictwo NiezaleĹĽne).
135. George, L., Drozd, V., Saxena, S.K., Bardaji, E.G., and Fichtner, M. (2009). Structural Phase Transitions of Mg(BH4)2 under Pressure. J. Phys. Chem. C *113*, 486–492. DOI:10.1021/JP807842T/ASSET/IMAGES/LARGE/JP-2008-07842T_0006.JPEG.
136. Dronskowski, R., and Blochl, P.E. (1993). Crystal Orbital Hamilton Populations (COHP). Energy-Resolved Visualization of Chemical Bonding in Solids Based on Density-Functional Calculations. J. Phys. Chem *97*, 8617–8624.
137. Deringer, V.L., Tchougréeff, A.L., and Dronskowski, R. (2011). Crystal Orbital Hamilton Population (COHP) Analysis As Projected from Plane-Wave Basis Sets. J. Phys. Chem. A *115*, 5461–5466. DOI:10.1021/JP202489S.
138. Culver, S.P., Squires, A.G., Minafra, N., Armstrong, C.W.F., Krauskopf, T., Böcher, F., Li, C., Morgan, B.J., and Zeier, W.G. (2020). Evidence for a Solid-Electrolyte Inductive Effect in the Superionic Conductor Li10Ge1-xSnxP2S12. J. Am. Chem. Soc. *142*, 21210–21219. DOI:10.1021/JACS.0C10735/SUPPL_FILE/JA0C10735_SI_002.ZIP.
139. Hautier, G., Fischer, C., Ehrlacher, V., Jain, A., and Ceder, G. (2010). Data Mined Ionic Substitutions for the Discovery of New Compounds. Inorg. Chem. *50*, 656–663. DOI:10.1021/IC102031H.
140. Wang, L., Maxisch, T., and Ceder, G. (2006). Oxidation energies of transition metal oxides within the GGA+U framework. Phys. Rev. B - Condens. Matter Mater. Phys. *73*, 195107. DOI:10.1103/PhysRevB.73.195107.
141. Wang, Y., Richards, W.D., Bo, S.-H., Miara, L.J., and Ceder, G. (2017).

Computational Prediction and Evaluation of Solid-State Sodium Superionic Conductors Na7P3X11 (X = O, S, Se). Chem. Mater. *29*, 7475–7482. DOI:10.1021/ACS.CHEMMATER.7B02476.

142. Nosé, S. (1984). A unified formulation of the constant temperature molecular dynamics methods. J. Chem. Phys. *81*, 511–519. DOI:10.1063/1.447334.
143. Schmuch, R., Wagner, R., Hörpel, G., Placke, T., and Winter, M. (2018). Performance and cost of materials for lithium-based rechargeable automotive batteries. Nat. Energy 2018 34 *3*, 267–278. DOI:10.1038/s41560-018-0107-2.
144. Randau, S., Weber, D.A., Kötz, O., Koerver, R., Braun, P., Weber, A., Ivers-Tiffée, E., Adermann, T., Kulisch, J., Zeier, W.G., et al. (2020). Benchmarking the performance of all-solid-state lithium batteries. Nat. Energy 2020 53 *5*, 259–270. DOI:10.1038/s41560-020-0565-1.
145. Nam, Y.J., Oh, D.Y., Jung, S.H., and Jung, Y.S. (2018). Toward practical all-solid-state lithium-ion batteries with high energy density and safety: Comparative study for electrodes fabricated by dry- and slurry-mixing processes. J. Power Sources *375*, 93–101. DOI:10.1016/J.JPOWSOUR.2017.11.031.
146. Barroso-Luque, L., Tu, Q., and Ceder, G. (2020). An Analysis of Solid-State Electrodeposition-Induced Metal Plastic Flow and Predictions of Stress States in Solid Ionic Conductor Defects. J. Electrochem. Soc. *167*, 020534. DOI:10.1149/1945-7111/AB6C5B.
147. Seino, Y., Ota, T., Takada, K., Hayashi, A., and Tatsumisago, M. (2014). A sulphide lithium super ion conductor is superior to liquid ion conductors for use in rechargeable batteries. Energy Environ. Sci. *7*, 627–631. DOI:10.1039/c3ee41655k.
148. Wood, K.N., Steirer, K.X., Hafner, S.E., Ban, C., Santhanagopalan, S., Lee, S.H., and Teeter, G. (2018). Operando X-ray photoelectron spectroscopy of solid electrolyte interphase formation and evolution in Li2S-P2S5 solid-state electrolytes. Nat. Commun. *9*, 2490. DOI:10.1038/s41467-018-04762-z.
149. Wenzel, S., Randau, S., Leichtweiß, T., Weber, D.A., Sann, J., Zeier, W.G., and Janek, J. (2016). Direct Observation of the Interfacial Instability of the Fast Ionic Conductor Li10GeP2S12 at the Lithium Metal Anode. Chem. Mater. *28*, 2400–2407. DOI:10.1021/ACS.CHEMMATER.6B00610/ASSET/IMAGES/LARGE/CM-2016-00610Y_0005.JPEG.
150. Lian, P.J., Zhao, B.S., Zhang, L.Q., Xu, N., Wu, M.T., and Gao, X.P. (2019). Inorganic sulfide solid electrolytes for all-solid-state lithium secondary batteries. J. Mater. Chem. A *7*, 20540–20557. DOI:10.1039/C9TA04555D.
151. Xu, X., Ai, Q., Pan, L., Ma, X., Zhai, W., An, Y., Hou, G., Chen, J., Zhang, L., Si, P., et al. (2018). Li 7 P 3 S 11 solid electrolyte coating silicon for high-

performance lithium-ion batteries. Electrochim. Acta *276*, 325–332. DOI:10.1016/j.electacta.2018.04.208.
152. Zhang, Z., Shao, Y., Lotsch, B., Hu, Y.S., Li, H., Janek, J., Nazar, L.F., Nan, C.W., Maier, J., Armand, M., et al. (2018). New horizons for inorganic solid state ion conductors. Energy Environ. Sci. *11*, 1945–1976. DOI:10.1039/c8ee01053f.
153. Stramare, S., Thangadurai, V., and Weppner, W. (2003). Lithium Lanthanum Titanates: A Review. Chem. Mater. *15*, 3974–3990. DOI:10.1021/CM0300516/ASSET/IMAGES/LARGE/CM0300516F00016.JPEG.
154. Suzuki, N., Richards, W.D., Wang, Y., Miara, L.J., Kim, J.C., Jung, I.S., Tsujimura, T., and Ceder, G. (2018). Synthesis and Electrochemical Properties of i 4-Type Li1+2xZn1-xPS4 Solid Electrolyte. Chem. Mater. *30*, 2236–2244. DOI:10.1021/ACS.CHEMMATER.7B03833/ASSET/IMAGES/LARGE/CM-2017-03833W_0010.JPEG.
155. Knauth, P. (2009). Inorganic solid Li ion conductors: An overview. Solid State Ionics *180*, 911–916. DOI:10.1016/J.SSI.2009.03.022.
156. Sendek, A.D., Yang, Q., Cubuk, E.D., Duerloo, K.A.N., Cui, Y., and Reed, E.J. (2017). Holistic computational structure screening of more than 12000 candidates for solid lithium-ion conductor materials. Energy Environ. Sci. *10*, 306–320. DOI:10.1039/C6EE02697D.
157. Sendek, A.D., Cubuk, E.D., Antoniuk, E.R., Cheon, G., Cui, Y., and Reed, E.J. (2019). Machine Learning-Assisted Discovery of Solid Li-Ion Conducting Materials. Chem. Mater. *31*, 342–352. DOI:10.1021/ACS.CHEMMATER.8B03272/ASSET/IMAGES/LARGE/CM-2018-03272M_0004.JPEG.
158. Muy, S., Voss, J., Schlem, R., Koerver, R., Sedlmaier, S.J., Maglia, F., Lamp, P., Zeier, W.G., and Shao-Horn, Y. (2019). High-Throughput Screening of Solid-State Li-Ion Conductors Using Lattice-Dynamics Descriptors. iScience *16*, 270–282. DOI:10.1016/J.ISCI.2019.05.036.
159. Zhang, Y., He, X., Chen, Z., Bai, Q., Nolan, A.M., Roberts, C.A., Banerjee, D., Matsunaga, T., Mo, Y., and Ling, C. (2019). Unsupervised discovery of solid-state lithium ion conductors. Nat. Commun. 2019 101 *10*, 1–7. DOI:10.1038/s41467-019-13214-1.
160. Kahle, L., Marcolongo, A., and Marzari, N. (2020). High-throughput computational screening for solid-state Li-ion conductors. Energy Environ. Sci. *13*, 928–948. DOI:10.1039/C9EE02457C.
161. He, X., Bai, Q., Liu, Y., Nolan, A.M., Ling, C., Mo, Y., He, X., Bai, Q., Liu, Y., Nolan, A.M., et al. (2019). Crystal Structural Framework of Lithium Super-Ionic Conductors. Adv. Energy Mater. *9*, 1902078.

DOI:10.1002/AENM.201902078.
162. Arbi, K., Mandal, S., Rojo, J.M., and Sanz, J. (2002). Dependence of ionic conductivity on composition of fast ionic conductors Li1+xTi2-xAlx(PO4)3, $0 \leq x \leq 0.7$. A parallel NMR and electric impedance study. Chem. Mater. *14*, 1091–1097. DOI:10.1021/CM010528I/ASSET/IMAGES/LARGE/CM010528IF00008.JPEG.
163. Kim, J., Kim, J., Avdeev, M., Yun, H., and Kim, S.J. (2018). LiTa 2 PO 8 : a fast lithium-ion conductor with new framework structure. J. Mater. Chem. A *6*, 22478–22482. DOI:10.1039/C8TA09170F.
164. Wang, Q., Wu, J.F., Lu, Z., Ciucci, F., Pang, W.K., and Guo, X. (2019). A New Lithium-Ion Conductor LiTaSiO5: Theoretical Prediction, Materials Synthesis, and Ionic Conductivity. Adv. Funct. Mater. *29*, 1904232. DOI:10.1002/ADFM.201904232.
165. Xiong, S., He, X., Han, A., Liu, Z., Ren, Z., McElhenny, B., Nolan, A.M., Chen, S., Mo, Y., and Chen, H. (2019). Computation-Guided Design of LiTaSiO5, a New Lithium Ionic Conductor with Sphene Structure. Adv. Energy Mater. *9*, 1803821. DOI:10.1002/AENM.201803821.
166. Hong, H.Y.P. (1978). Crystal structure and ionic conductivity of Li14Zn(GeO4)4 and other new Li+ superionic conductors. Mater. Res. Bull. *13*, 117–124. DOI:10.1016/0025-5408(78)90075-2.
167. Bruce, P.G., and West, A.R. (1980). Phase diagram of the LISICON, solid electrolyte system, Li4GeO4-Zn2GeO4. Mater. Res. Bull. *15*, 379–385. DOI:10.1016/0025-5408(80)90182-8.
168. Jain, A., Ong, S.P., Hautier, G., Chen, W., Richards, W.D., Dacek, S., Cholia, S., Gunter, D., Skinner, D., Ceder, G., et al. (2013). Commentary: The Materials Project: A materials genome approach to accelerating materials innovation. APL Mater. *1*, 011002. DOI:10.1063/1.4812323.
169. Ong, S.P., Richards, W.D., Jain, A., Hautier, G., Kocher, M., Cholia, S., Gunter, D., Chevrier, V.L., Persson, K.A., and Ceder, G. (2013). Python Materials Genomics (pymatgen): A robust, open-source python library for materials analysis. Comput. Mater. Sci. *68*, 314–319. DOI:10.1016/J.COMMATSCI.2012.10.028.
170. Belkly, A., Helderman, M., Karen, V.L., and Ulkch, P. (2002). New developments in the Inorganic Crystal Structure Database (ICSD): accessibility in support of materials research and design. urn:issn:0108-7681 *58*, 364–369. DOI:10.1107/S0108768102006948.
171. Malik, R., Burch, D., Bazant, M., and Ceder, G. (2010). Particle size dependence of the ionic diffusivity. Nano Lett. *10*, 4123–4127. DOI:10.1021/NL1023595/SUPPL_FILE/NL1023595_SI_001.PDF.

172. Lee, D.W., and Ok, K.M. (2013). New alkali-metal gallium selenites, AGa(SeO3)2 (A = Li, Na, K, and Cs): Effect of cation size on the framework structures and macroscopic centricities. Inorg. Chem. *52*, 5176–5184. DOI:10.1021/IC400458A/SUPPL_FILE/IC400458A_SI_002.CIF.
173. Di Stefano, D., Miglio, A., Robeyns, K., Filinchuk, Y., Lechartier, M., Senyshyn, A., Ishida, H., Spannenberger, S., Prutsch, D., Lunghammer, S., et al. (2019). Superionic Diffusion through Frustrated Energy Landscape. Chem *5*, 2450–2460. DOI:10.1016/J.CHEMPR.2019.07.001.
174. Pinsky, M., and Avnir, D. (1998). Continuous Symmetry Measures. 5. The Classical Polyhedra. Inorg. Chem. *37*, 5575–5582. DOI:10.1021/IC9804925/ASSET/IMAGES/MEDIUM/IC9804925E00016.GIF.
175. Van der Ven, A., Ceder, G., Asta, M., and Tepesch, P.D. (2001). First-principles theory of ionic diffusion with nondilute carriers. Phys. Rev. B *64*, 184307. DOI:10.1103/PhysRevB.64.184307.
176. Lee, J., Urban, A., Li, X., Su, D., Hautier, G., and Ceder, G. (2014). Unlocking the potential of cation-disordered oxides for rechargeable lithium batteries. Science (80-. ). *343*, 519–522. DOI:10.1126/science.1246432.
177. Zhang, Z., Li, H., Kaup, K., Zhou, L., Roy, P.N., and Nazar, L.F. (2020). Targeting Superionic Conductivity by Turning on Anion Rotation at Room Temperature in Fast Ion Conductors. Matter *2*, 1667–1684. DOI:10.1016/J.MATT.2020.04.027.
178. Hanghofer, I., Gadermaier, B., and Wilkening, H.M.R. (2019). Fast Rotational Dynamics in Argyrodite-Type Li6PS5X (X: Cl, Br, I) as Seen by 31P Nuclear Magnetic Relaxation - On Cation-Anion Coupled Transport in Thiophosphates. Chem. Mater. *31*, 4591–4597. DOI:10.1021/ACS.CHEMMATER.9B01435/ASSET/IMAGES/LARGE/CM-2019-01435E_0003.JPEG.
179. Rong, Z., Xiao, P., Liu, M., Huang, W., Hannah, D.C., Scullin, W., Persson, K.A., and Ceder, G. (2017). Fast Mg 2+ diffusion in Mo 3 (PO 4 ) 3 O for Mg batteries. Chem. Commun. *53*, 7998–8001. DOI:10.1039/C7CC02903A.
180. Delaunay, B. Sur la sphère vide (1934) Bul Acad Sci URSS. Cl. Sci Nat, 793–800.
181. Daly, P.W. (1994). The Tetrahedron Quality Factors of CSDS.
182. Perdew, J.P., Burke, K., and Ernzerhof, M. (1996). Generalized Gradient Approximation Made Simple. Phys. Rev. Lett. *77*, 3865. DOI:10.1103/PhysRevLett.77.3865.
183. Blöchl, P.E. (1994). Projector augmented-wave method. Phys. Rev. B *50*, 17953. DOI:10.1103/PhysRevB.50.17953.
184. Kresse, G., and Furthmüller, J. (1996). Efficient iterative schemes for *ab initio*

total-energy calculations using a plane-wave basis set. Phys. Rev. B *54*, 11169. DOI:10.1103/PhysRevB.54.11169.
185. Jain, A., Hautier, G., Ong, S.P., Moore, C.J., Fischer, C.C., Persson, K.A., and Ceder, G. (2011). Formation enthalpies by mixing GGA and GGA + U calculations. Phys. Rev. B - Condens. Matter Mater. Phys. *84*, 045115. DOI:10.1103/PHYSREVB.84.045115/FIGURES/5/MEDIUM.
186. Miara, L.J., Richards, W.D., Wang, Y.E., and Ceder, G. (2015). First-Principles Studies on Cation Dopants and Electrolyte|Cathode Interphases for Lithium Garnets. Chem. Mater. *27*, 4040–4047. DOI:10.1021/ACS.CHEMMATER.5B01023/SUPPL_FILE/CM5B01023_SI_001.PDF.
187. He, X., Zhu, Y., Epstein, A., and Mo, Y. (2018). Statistical variances of diffusional properties from ab initio molecular dynamics simulations. npj Comput. Mater. 2018 41 *4*, 1–9. DOI:10.1038/s41524-018-0074-y.
188. Cussen, E.J., O'Callaghan, M.P., Powell, A.S., Titman, J.J., and Chen, G.Z. (2008). Switching on fast lithium ion conductivity in garnets: The structure and transport properties of Li3+xNd3Te2-xSb xO12. Chem. Mater. *20*, 2360–2369. DOI:10.1021/CM703677Q/SUPPL_FILE/CM703677Q-FILE002.PDF.
189. O'Callaghan, M.P., Lynham, D.R., Cussen, E.J., and Chen, G.Z. (2006). Structure and ionic-transport properties of lithium-containing garnets Li3Ln3Te2O12 (Ln = Y, Pr, Nd, Sm-Lu). Chem. Mater. *18*, 4681–4689. DOI:10.1021/CM060992T/ASSET/IMAGES/LARGE/CM060992TF00009.JPEG.
190. Bruce, P.G., and West, A.R. (1982). Ionic conductivity of LISICON solid solutions, Li2+2xZn1−xGeO4. J. Solid State Chem. *44*, 354–365. DOI:10.1016/0022-4596(82)90383-8.
191. Zhao, G., Suzuki, K., Seki, T., Sun, X., Hirayama, M., and Kanno, R. (2020). High lithium ionic conductivity of γ-Li3PO4-type solid electrolytes in Li4GeO4−Li4SiO4–Li3VO4 quasi-ternary system. J. Solid State Chem. *292*, 121651. DOI:10.1016/J.JSSC.2020.121651.
192. He, X., Zhu, Y., and Mo, Y. (2017). Origin of fast ion diffusion in super-ionic conductors. Nat. Commun. 2017 81 *8*, 1–7. DOI:10.1038/ncomms15893.
193. Deng, Y., Eames, C., Chotard, J.N., Laleìre, F., Seznec, V., Emge, S., Pecher, O., Grey, C.P., Masquelier, C., and Islam, M.S. (2015). Structural and Mechanistic Insights into Fast Lithium-Ion Conduction in Li4SiO4-Li3PO4 Solid Electrolytes. J. Am. Chem. Soc. *137*, 9136–9145. DOI:10.1021/JACS.5B04444/SUPPL_FILE/JA5B04444_SI_002.CIF.
194. Aono, H., Sugimoto, E., Sadaoka, Y., Imanaka, N., and Adachi, G. ya (1990). Ionic conductivity and sinterability of lithium titanium phosphate system. Solid State Ionics *40–41*, 38–42. DOI:10.1016/0167-2738(90)90282-V.

195. Waroquiers, D., Gonze, X., Rignanese, G.M., Welker-Nieuwoudt, C., Rosowski, F., Göbel, M., Schenk, S., Degelmann, P., André, R., Glaum, R., et al. (2017). Statistical analysis of coordination environments in Oxides. Chem. Mater. *29*, 8346–8360. DOI:10.1021/ACS.CHEMMATER.7B02766/SUPPL_FILE/CM7B02766_SI_001.XLS.
196. Szymanski, N.J., Zeng, Y., Huo, H., Bartel, C.J., Kim, H., and Ceder, G. (2021). Toward autonomous design and synthesis of novel inorganic materials. Mater. Horizons *8*, 2169–2198. DOI:10.1039/D1MH00495F.
197. Wang, C., Ping, W., Bai, Q., Cui, H., Hensleigh, R., Wang, R., Brozena, A.H., Xu, Z., Dai, J., Pei, Y., et al. (2020). A general method to synthesize and sinter bulk ceramics in seconds. Science (80-. ). *368*, 521–526. DOI:10.1126/SCIENCE.AAZ7681/SUPPL_FILE/AAZ7681S2.MP4.
198. Smetaczek, S., Wachter-Welzl, A., Wagner, R., Rettenwander, D., Amthauer, G., Andrejs, L., Taibl, S., Limbeck, A., and Fleig, J. (2019). Local Li-ion conductivity changes within Al stabilized Li 7 La 3 Zr 2 O 12 and their relationship to three-dimensional variations of the bulk composition. J. Mater. Chem. A *7*, 6818–6831. DOI:10.1039/C9TA00356H.
199. Grady, Z.M., Tsuji, K., Ndayishimiye, A., Hwan-Seo, J., and Randall, C.A. (2020). Densification of a Solid-State NASICON Sodium-Ion Electrolyte below 400 °c by Cold Sintering with a Fused Hydroxide Solvent. ACS Appl. Energy Mater. *3*, 4356–4366. DOI:10.1021/acsaem.0c00047.
200. Guo, J., Guo, H., Baker, A.L., Lanagan, M.T., Kupp, E.R., Messing, G.L., and Randall, C.A. (2016). Cold Sintering: A Paradigm Shift for Processing and Integration of Ceramics. Angew. Chemie - Int. Ed. *55*, 11457–11461. DOI:10.1002/anie.201605443.